Microswimming in Complex Fluids

Thomas R. Ives

Doctor of Philosophy
The University of Edinburgh
Janurary 2018

Lay Summary

There is a enormous variety of microorganisms found in nature, ranging from tiny bacteria which live in your gut to algae photosynthesising in ponds. Many of these tiny organisms have the ability to swim, and each uses its own strategy. An interesting question is: how do these strategies lead to the organism swimming? For example, we want to know how quickly it swims and how much energy it uses as it does so.

To answer these questions, we need to understand how swimming microorganisms, or microswimmers, interact with their fluid environments. These fluid environments are also enormously varied. For example, some microorganisms swim in water, which is a simple fluid that exhibits what is known as Newtonian behaviour. In contrast, other fluid environments, like mucus or blood, contain large protein molecules consisting of thousands of atoms. Often these proteins are a similar size to the microorganisms themselves. This changes how the microswimmer interacts with its fluid environment.

These fluids are known as complex fluids. They are often gooey, or what we call viscoelastic. We have investigate how this viscoelasticity can effect microswimmers. In order to do this, we have used a model swimmer, called Taylor's waving sheet, which is inspired by sperm. We have developed intuitive pictures of what is happening when swimming in the middle of such a fluid or close to a wall. We have also investigated how the similar sizes of the microswimmers and the protein molecules in the fluid can drastically change how the viscoelasticity interacts with the swimmer. Finally, we have tried to understand how evolution has chosen a swimmers strategy using mathematical optimisations.

Abstract

Many microorganisms have the ability to propel themselves through their fluid environments by periodically actuating their body. The biological fluid environments surrounding these microswimmers are typically complex fluids containing many high-molecular weight protein molecules, which give the fluid non-Newtonian rheological properties. In this thesis, we investigate the effect that one such rheological property, viscoelasticity, has on microswimming. We consider a classical model of a microswimmer, the so-called Taylor's waving sheet and generalise it to arbitrary shapes. We employ the Oldroyd-B model to study its swimming analytically and numerically. We attempt to develop a mechanistic understanding of the swimmer's behaviour in viscoelastic fluids.

It has recently been suggested that continuum models of complex biological fluids might not be appropriate for studying the swimming of flagellated microorganisms as the size of biological macromolecules is comparable to the typical width of a microorganism's flagellum. A part of this thesis is devoted to exploring this scenario. We propose an alternative method for modelling complex fluids using a two-fluid depletion region model and we have developed a numerical solver to find the swimming speed and rate of work for the generalised Taylor's waving sheet model swimmer using this alternate depletion region model.

This thesis is organised as follows. In the first chapter, we outline a physical mechanism for the slowing down of Taylor's sheet in an Oldroyd-B fluid as the Deborah number increases. We demonstrate how a microswimmer can be designed to avoid this. In the second chapter, we investigate swimming in an Oldroyd-B fluid near a solid boundary and show that, at large amplitudes and low polymer concentrations, the swimming speed of Taylor's sheet increases with De. In the third chapter, we show how the Oldroyd-B model can be adapted using depletion regions. In the final chapter, we investigate optimal swimming in a Newtonian fluid. We show that while the organism's energetics are important, the kinematics of planar-wave microswimmers do not optimise the hydrodynamic 'efficiency' typically used for mathematical optimisation in the literature.

Declaration

I declare that this thesis was composed by myself, that the work contained herein is my own except where explicitly stated otherwise in the text, and that this work has not been submitted for any other degree or professional qualification except as specified.

Parts of this work have been published in [1].

(*Thomas R. Ives, Janurary 2018*)

Acknowledgements

First, I would like to thank my supervisor Alexander Morozov for his guidance and encouragement.

Thank you also to my parents Michael and Julie for supporting me throughout this process.

Thank you to Gabrielle for putting up with me, and Ada for helping her do so.

This work was supported by SUPA[1] and EPSRC[2].

---

[1] Scottish Universities Physics Alliance

[2] The Engineering and Physical Sciences Research Council

Contents

List of Figures

List of Tables

Chapter 1

Introduction

Microswimmers are microorganisms that propel themselves through a fluid environment by actuating their bodies, or in some cases specialised organelles, in a cyclical fashion. Due to their small size, the mechanism of propulsion of microswimmers is fundamentally different to that of macroscopic fish. It is for this reason that physicists first became interested in microswimming in the 1950s. The swimming of fish or other macroscopic swimmers can be understood using conservation of momentum arguments (see [2] for an example of such arguments). In contrast, these conservation arguments cannot be applied to microswimmers because there is an absence of inertia for microscopic objects in viscous fluids. In fact, the absense of intertia has much more profound effects than the breakdown of these arguments. In 1976, some 25 years after the inital investigations into microswimming, Edward Purcell [3] noted that the absence of inertia on the microscopic scale also meant that any microswimmer with a time-reversible gait cannot swim, in contrast to macroscopic organisms where no such restriction exists.

Early studies of microswimmers by physicists were focussed on understanding how these organisms can propel themselves in the absence of inertia. Observations by the biologist James Gray [4] showed that to avoid Purcell's prohibition of time-reversible gaits, sea-urchin spermatozoa swim by propagating planar waves along a tail-like organelle, known as a flagellum. As a result of this, the sea-urchin spermatozoa swim in the opposite direction to the wave. This might look similar to the swimming method used by some macroswimmers, such as eels, which swim in the opposite direction to waves they propagate along their body. However, the absence of inertia in the microscopic case means that this can only be a superficial similarity. Geoffrey I. Taylor [5] was quick to show that microscopic planar-wave swimmers, such as spermatozoa, can propel themselves in the absence of inertia. In addition, G. J. Hancock [6] demonstrated that this propulsion could be understood as the spermatozoa exploiting what later became known as drag anisotropy. Later, Allen Chwang and Theodore Wu [7] used this drag anisotropy idea to show that microorganisms can swim by propagating helical rather than planar waves. Shortly after Chwang and Wu's calculation on helical swimming, observations by Howard Berg [8] of *Escherichia coli* showed that such bacteria do in fact swim by rotating helical flagella. Purcell [9] demonstrated that this swimming strategy is similar to that of spermatozoa in that it exploits the drag anisotropy of the flagella.

With such an understanding of how microswimmers propel themselves in Newtonian fluids, more recent studies have focussed on the collective behaviour of microswimmers. Typically, microswimmers interact with each other via long-range hydrodynamic interactions. Microswimmer suspensions exhibit various interesting phenomena as a result of these interactions. For example, the emergence of large-scale coherent structures have been observed in suspensions of microswimmers [10, 11]. Other studies highlight the phenomena of 'bacterial turbulence' [12], which is reminiscent of the hydrodynamic turbulence of large-Reynolds number Newtonian flows.

These studies often only consider microswimmers swimming in water, a simple Newtonian fluid. However, some microorganisms in their natural environments swim through complex fluids, which exhibit various types of non-Newtonian behaviour, such as viscoelasticity and shear thinning. The study of and the collection of these non-Newtonian behaviours are both known as rheology. For example, nematodes are tiny worms that propel themselves through soil by undulating their body [13]. Mammalian spermatozoa must swim through cervical mucus to reach the egg for fertilisation [14]. Many pathogens must swim through mucus to infect their host [15, 16]. And finally, bacterial motility in complex fluids plays an important role in biofilm stability [17].

There have been many recent studies into the behaviour of microswimmers in complex fluids. Although real microorganisms typically have different swimming gaits and beat frequencies in different fluids, one of the most common questions asked in such studies is whether a microswimmer with fixed kinematics swims faster or slower in a complex fluid than it would in a Newtonian one. This is a mathematically well defined problem, which does not require a detailed knowlegde of the organisms biology. It has been found both experimentally [18–21] and theoretically [22–33] that there is no universal answer to this question. Some microswimmers in some fluids swim faster than they would in a Newtonian fluid; whereas, other microswimmers in other fluids swim slower. Given the wide variety of microorganisms and complex fluids considered in these studies, this suggests that the behaviour of microswimmers in complex fluids depends on the geometry of the swimmer, its gait and the rheology of the fluid. These measurements and predictions are just observations and there have been few attempts to pair these with a mechanistic understanding of this behaviour. This thesis aspires to begin bridging this gap by developing such a mechanistic understanding of microswimmers in complex fluids.

This introduction contains four sections. Section 1.1 provides an introduction to biological microswimmers and microswimming in Newtonian fluids. Section 1.2 provides a short introduction to the rheology of complex fluids. Section 1.3 provides an overview of some experiments on microswimmers in complex fluids. And finally Section 1.4 outlines the research programme for this thesis.

1.1 Low Reynolds number swimming

In this section, we give a brief overview of swimming in low Reynolds number environments, highlighting a key result for the Newtonian case: Purcell's scallop theorem. Then, we familiarise the reader with some biological microswimmers and how they behave. Finally, we introduce the mathematical microswimmer we use throughout this thesis: Taylor's waving sheet. For more detailed reviews of low Reynolds number swimming in Newtonian fluids see [34–36].

1.1.1 Life at low Reynolds number

Microswimmers are united as a topic of study by their size relative to the properties of the fluid they are swimming in. That is, they are small enough and move slowly enough that the effects of inertia in the fluid are negligible. This can be characterised by the Reynolds number of the situation Re, which is a dimensionless quantity that estimates the ratio of the effects of inertia to the viscous forces in the fluid. Suppose the microswimmer has a characteristic length scale L and characteristic speed U then the inertial effects felt by the microswimmer will be of the order $\rho U^2/L$, where ρ is the density of the fluid. The viscous force densities will be of the order $\eta U/L^2$ where η is the viscosity of the fluid. Thus, the Reynolds number is ratio of these two quantities and is given by

$$\mathrm{Re} = \frac{\rho L U}{\eta}. \tag{1.1}$$

When the Reynolds number is small, that is $\mathrm{Re} \ll 1$, inertia can be neglected and we say the problem is in the low Reynolds-number regime. The Reynolds number for a bacterium in water is typically $\mathrm{Re} \approx 10^{-5}$ [37] and even relatively large organisms, such as nematodes ($L \approx 1\,\mathrm{mm}$), can have $\mathrm{Re} < 10^{-3}$ in high viscosity fluids [20].

In the low Reynolds-number regime, Newtonian fluids surrounding a microswimmer are governed by the Stokes flow equations, which are given by

$$-\nabla p + \eta \nabla^2 \boldsymbol{u} = \boldsymbol{0}, \tag{1.2}$$

$$\nabla \cdot \boldsymbol{u} = 0. \tag{1.3}$$

where p and $\boldsymbol{u}$ are the pressure and velocity fields in the fluid, respectively. The Stokes' equations are linear and have no explicit time dependence. For microswimmers, this leads to what is known as Purcell's scallop theorem [3]. Purcell showed that, as a consequence of the linearity of the Stokes' equations, any microorganism with time-reversible kinematics cannot swim. For example, a scallop is a high Reynolds-number swimmer that propels itself by opening and closing its shell. This is a time reversible process. If we were to shrink the scallop, or alternatively place it in a very viscous fluid, such that it was in the low Reynolds-number regime, it would not longer swim. All progress made when closing the shell is undone when the shell is opened again and the 'microscallop' cannot make any progress. Importantly, because the Stokes' equations are independent of time, this time-reversibility constraint is unaffected by how quickly the organism performs the forward and backward strokes. The microscallop can open its shell slowly and close it quickly, it still will not make any progress.

To familiarise the reader with biological microswimmers and the strategies they use to overcome the challenges posed by the scallop theorem, we now give a brief overview of various swimming microorganisms found in nature.

Figure 1.1 A collage of microorganisms with flagella and related organisms. Drawn by Sir James Lighthill [2] and adopted from [35].

1.1.2 Biological microswimmers

As shown in Fig. 1.1, which was drawn by James Lighthill [2], many microorganisms have evolved to use an organelle known as a flagellum to swim. Flagella are evolutionarily conserved organelles. That is, there is very little variation in the structure of flagella motors inside a domain of life. All organisms can be split into three domains: archaea, bacteria and eukaryotes. In each of these domains, flagella have (probably) evolved independently. Although the chemical structure of archaic and bacterial flagella are very different, for our purposes, the physical structure is similar enough that we only need consider one to gain an understanding of the strategies microorganisms have evolved for swimming. Archaic flagella are less well understood than their bacterial counterparts, so we chose bacterial flagella to discuss here.

A bacterial flagellum is a relatively rigid filament attached by a hook to a motor at the body of the bacterium. The following properties of bacterial flagella have been observed [38]. The filament has a constant diameter of ≈5 nm and a length of ≈5–10 μm. The filament forms a left-handed helix with a diameter of ≈200 nm and a pitch of $\approx$2–2.5 μm. Depending on the species, a bacterium can have anywhere from one to 100 flagella, which can be either clustered at some location on the bacterium or they can be arranged randomly all over the surface of the cell.

E. coli is a very commonly studied bacterial species. Wild-type *E. coli* has a rod-shaped body, with a length of $\approx$2 μm and diameter of $\approx$1 μm. An *E. coli* cell typically has around 10 flagella all over its body [38]. The motors of the flagella have two modes, where they rotate either clockwise or anticlockwise at a frequency of $\approx$100 Hz [39]. When the motor rotates anticlockwise, as seen by an external observer, the flagella form a single helical bundle, often at the pole of the cell. The flagella bundle and the cell body rotate in opposite directions and the bacterium swims in a straight line. In the bulk of an aqueous solution the swimming speed of *E. coli* is $\approx$20 $\mu\mathrm{m\,s}^{-1}$ [37]. Thus, a typical *E. coli* bactrium travels $\approx$ 200 nm per rotation of its flagella bundle. With clockwise rotation, the bundle pulls apart and the cell ‘tumbles’, reorienting itself.

Unlike bacterial flagella, which are driven by a rotatory motor at the cell body, the motor of a eukaryotic flagellum is located along its length. The internal structure of a eukaryotic flagellum is called an axoneme. For most organisms, the axoneme consists of nine outer microtubule doublets surrounding a central pair of microtubules (the so-called 9+2 structure) [40]. The motor of the flagellum is a molecule called dynein, which is located between adjacent outer doublets. The motor produces a sliding motion between the adjacent doublets that causes the flagellum as a whole to bend. In order to accommodate this more complicated internal structure, eukaryotic flagella are thicker than bacterial flagella at $\approx$200 nm [14]. The more sophisticated structure of eukaryotic flagella allows for actuation via the bending of the flagella, as opposed to the simple rigid body rotation of their bacterial counterparts.

Spermatozoa are eukaryotes with a single polar flagellum. The length of a spermatozoon’s flagellum is species dependent and ranges from $\approx$50–250 μm. The head of a spermatazoon has a diameter that also varies according to the species between $\approx$5–10 μm [40]. The spermatozoa of sea urchins, such as *Lytechinus pictus* are often studied. The flagellum of an *L. pictus* spermatozoon propagates a planar wave along its length, causing the organism to swim at speeds of $\approx$160 $\mu\mathrm{m\,s}^{-1}$ against the direction of the wave. The wave has a wavelength of $\approx$20 μm, a wave amplitude of $\approx$5 μm and a frequency of $\approx$30 Hz [41]. The cell travels $\approx$ 530 nm per beat of its flagellum.

Not all eukaryotic flagellates propagate waves along their flagella to swim. For example, the spherical algae *Chlamydomonas reinhardtii* have a diameter of $\approx$10 μm [42] and two flagella located at the front of the cell bodies. When they swim forward, the flagella do not propagate planar waves along their length. Instead, the flagella perform three-dimensional, non-time-reversible beats, which pull the organism forward [43]. Using this 'breaststroke' motion, the cell swims at a speed of $\approx$60 $\mu\mathrm{m\,s^{-1}}$ in water [44]. When swimming backwards, *C. reinhardtii* propagates planar waves along its flagella in a similar manner to spermatozoa.

Cilia are structurally similar to eukaryotic flagella [40], but they are typically more numerous on the cell. Cilliates of the genus *Paramecium* are unicellular eukaryotes with a length of $\approx$100–300 μm, covered in $\approx$5000–6000 cilia [45]. Each of the cilia performs a non-time-reversible three-dimensional stroke, similar to the flagella of *C. reinhardtii.* The cilia are synchronised with a small phase difference between neighbouring cilia, such that a so-called metachronal wave of beating propagates along the length of the cell. By this mechanism, the cell swims. The species *Paramecium tetraurelia* have swimming speeds in the range of $\approx$140–470 $\mu\mathrm{m\,s^{-1}}$ [46].

Not all microorganisms use flagella or cilia to swim. For example, nematodes are small multicellular worms that swim by propagating planar waves along their bodies. *Caenorhabditis elegans* is a commonly studied species of nematode consisting of $\approx$2000–3000 eukaryotic cells [47]. *C. elegans* have a length of $\approx$1 mm and a diameter of $\approx$70 μm. *C. elegans* propagate waves with an amplitude $\approx$0.25 mm, wavelength $\approx$2.5 mm and frequency $\approx$2 Hz [20]. With such kinematics, they swim at a speed of $\approx$0.35 $\mathrm{mm\,s^{-1}}$ in Newtonian fluids [48], propelling itself $\approx$ 175 μm per beat.

For a bacterial example of swimming without a flagella, consider the genus *Spiroplasma.* Unlike most bacteria, *Spiroplasma* lack cell walls and their bodies form long, thin helices. These helices have a diameter of $\approx$150 nm, a length of $\approx$20 μm and a pitch of $\approx$600 nm. The cell body itself has a diameter of $\approx$200 nm. The organism swims by propagating kinks along its length where the chirality of the helix changes. These kinks travel at a speed of $\approx$10 $\mu\mathrm{m\,s^{-1}}$, which results in swimming speeds of $\approx$3 $\mu\mathrm{m\,s^{-1}}$ in water [49].

The final microorganisms we will discuss are spirochetes, which are bacteria that use internal flagella in order to swim. These internal flagella resemble the external flagella of other bacteria, such as *E. coli*, and reside in between the cell membrane

Figure 1.2 A schematic of Taylor's swimming sheet. The sheet propagates a wave along the x-axis with wave speed c and waveform f. It swims in the opposite direction to the wave at a speed U.

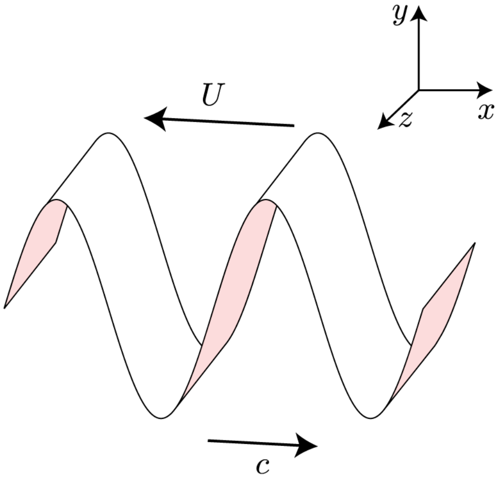

and wall. Spirochetes form long, thin helices with a length of $\approx 100\,\mu$m and a diameter of $\approx$0.4–3.0 μm [50]. Most spirochetes swim by rotating their entire body and propagating helical waves along their lengths. The cell rotation is believed to be driven by the rotation of the internal flagella. In order to compensate for the torque generated by the rotation of the internal flagella, the cell body rotates in the opposite direction [51]. Not all spirochetes are helical. For example, *Borrelia burgdorferi* have planar forms and swim by propagating planar waves along their lengths, reminiscent of eukaryotic flagella [52].

As we have shown, there are a large number of strategies employed by biological microswimmers in order to propel themselves. To study these biological microswimmers, we will use a simple mathematical model of a microswimmer: Taylor's waving sheet [5]. This model swimmer is inspired by planar-wave swimmers such as nematodes and spermatozoa. The following subsection introduces the model and some results for the swimmer in Newtonian fluids.

1.1.3 A mathematical microswimmer: Taylor's waving sheet

In 1951 Taylor [5] first proposed his sheet as a model microorganism to investigate low Reynolds swimming in a Newtonian fluid. The sheet is infinite in both its dimensions and propagates a transverse wave in the positive x-direction. Due to the motion of the wave, at a time t, the sheet makes the shape, $y_s = y_s(x,t)$, in the xy-plane, given by

$$y_s(x,t) = f(k(x-(c-U)t)), \tag{1.4}$$

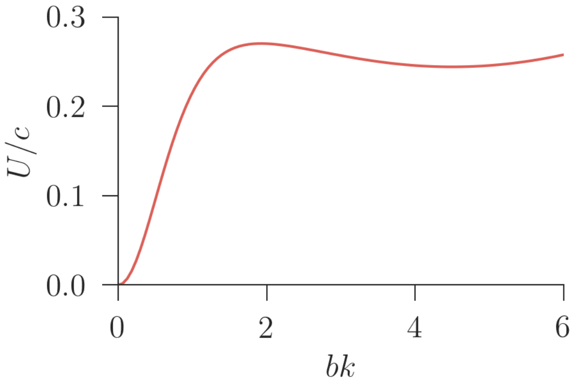

Figure 1.3 The swimming speed U of Taylor's sheet against wave amplitude b for the waveform $f(\zeta) = b\sin(\zeta)$ as found by Sauzade et al. [53]. The swimming speed is scaled by the wave speed c and the amplitude is scaled by the wavenumber k.

where U is the swimming speed of the sheet in the negative x-direction, f is the sheet's waveform, c is the speed of the wave and k is the associate wavenumber.

This model swimmer is afforded plenty of symmetries to simplify the problem. Firstly, there is translational symmetry in the z-direction, so we only have to consider a single xy-plane. Secondly, the sheet is periodic in the x-direction so we only have to consider a single period of the wave. Thirdly, as we will be considering low Reynolds-number flows, the time dependence of the problem only occurs via the travelling wave in Eq. (1.4). Thus, we can easily remove any explicit time dependence from the problem by moving to an appropriate frame of reference. Also, if the fluid is incompressible (which is the case we will be exclusively considering), then the sheet can only swim along the x-axis because the fluid above and below the sheet are disconnected.

When Taylor first proposed the swimmer he only considered the waveform $f(\zeta) = b\sin(\zeta)$ in the small-amplitude limit, that is $\epsilon = bk \ll 1$. In this limit, the sheet swims through a Newtonian fluid in the negative x-direction with a speed of

$$U = c\left(\frac{1}{2}\epsilon^2 - \frac{19}{32}\epsilon^4 + \mathcal{O}(\epsilon^6)\right). \tag{1.5}$$

More recently Sauzade et al. [53] have found the first 500 non-zero terms of the small-amplitude expansion of the swimming speed, the results of which are shown in Fig. 1.3. Sauzade et al. were able to remove the poles from their Taylor expansion, and find a series that converges to $bk \approx 15$.

One of the great strengths of Taylor's sheet is the ease with which we can find analytic expressions for the swimming in this small-amplitude limit. Moreover, en route to finding these swimming speeds, we also find analytic expressions for the small-amplitude flow fields around the sheet. This is useful because it allows us to understand the physical mechanisms at play.

Figure 1.4 shows a schematic of the mechanism responsible for the propulsion of the sheet with a sine waveform in a Newtonian fluid, as has been described by Lauga and Powers [36]. Taylor showed that, for a small-amplitude wave, as the wave passes along the sheet, the material points of the sheet move approximately vertically [5]. Due to the periodicity of the wave, for every material point moving upwards there is a corresponding material point moving downwards with the same speed. These material points push on the fluid and, in order to satisfy the incompressibility of the fluid and have the velocity field vanish far from the sheet, create an array of counter-rotating vortices. There is one clockwise-rotating vortex and one anticlockwise-rotating vortex per wavelength of the sheet. There is a net push on the sheet by the periodic array of vortices. This is due to the relationship between the direction of rotation of the vortices and the shape of the sheet. As shown in Fig. 1.4, peaks in the sheet's waveform find themselves above the centre of anticlockwise-rotating vortices; while troughs find themselves below the centre of clockwise-rotating vortices. Because of this arrangement, both peaks and troughs are pushed by the vortices in the opposite direction to the wave. This is the mechanism responsible for the sheet swimming.

It is important to realise that this mechanism is universal. Even though we only considered the small-amplitude solution, due to the geometric nature of the mechanistic argument above, it applies irrespective of the wave amplitude. Moreover, the argument is valid for any waveform. The arrangement of the vortices is determined by the gradient of the waveform and the direction of the wave. The location of the peaks and troughs of the waveform are also controlled by its gradient. As such, any peak of any waveform will find itself above the centre of an anticlockwise-rotating vortex. Similarly, any trough will find itself below the centre of a clockwise-rotating vortex. Thus, for *any* waveform of *any* amplitude, the sheet will swim in the opposite direction to the wave.

While Taylor only used the sheet to examine swimming in the bulk of a Newtonian fluid, others have used his model to find analytic expressions for the swimming speed of microswimmers in myriad other situations, such as: (i) swimming next to a boundary in a Newtonian fluid [44]; (ii) swimming in a small, but finite Reynolds-number fluid [54, 55]; (iii) starting to swim from rest [56]; (iv) swimming next to another swimmer [57, 58]; (v) swimming in a two-phase fluid [59]; (vi) swimming in a viscoelastic fluid [22, 60, 61] and (vii) swimming in a shear-thinning fluid [62].

As well as small-amplitude analytic calculations like those pioneered by Taylor,

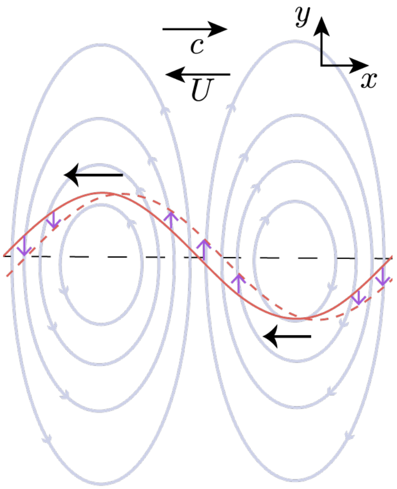

Figure 1.4 A schematic of the mechanism of propulsion of Taylor's waving sheet in a Newtonian fluid. The position of the sheet at a time t (solid red line) and $t + \delta t$ (dashed red line) are shown. The material points of the sheet are moving between these lines as indicated by the purple arrows. The material points push the surrounding fluid, generating an array counter-rotating vortices. These vortices line up with the shape of the sheet such that they push the sheet at a speed U in the opposite direction to the wave, which has a speed c.

we perform numerical calculations for the swimmer at finite wave amplitudes. We discuss these numerical calculations in the research chapters of this thesis.

Taylor's waving sheet is a simple model swimmer inspired by planar-wave swimmers such as spermatozoa. This simplicity is corroborated by the variety of situations that people have been able to find analytic expressions for the sheet's swimming speed. This makes the model an excellent choice for our purposes of investigating the mechanisms involved in swimming through complex fluids.

The objective of this thesis is to use this model swimmer to develop a mechanistic understanding in swimmers in complex fluids, which exhibit non-Newtonian behaviour. As seen above, there have been some studies using Taylor's sheet to examine swimming in shear-thinning and viscoelastic fluids. However, these studies have not provided mechanistic explanations such as those we seek to develop. In order to develop such mechanistic explanations, we must first understand the structure and behaviour of complex fluids. The next section will provide an overview of just that.

1.2 Complex fluids

Whilst in their natural habitat, many of the microorganisms we discussed in Section 1.1.2 swim in complex fluids. Some microorganisms, such as *C. elegans*, propel themselves through non-Newtonian environments, such as wet soils [13]; however, in this thesis we are concerned with swimming in biological fluids containing high molecular-weight biomacromolecules. For example, many microorganisms swim through mucuses found in metazoans [14–16]. Although the exact composition of mucus varies between species and location in the body, mucuses typically contain high molecular-weight, semiflexible mucin proteins [63] and exhibit non-Newtonian behaviours such as shear thinning, complex viscosities and first normal-stress differences [64, 65].

Biological complex fluids are not a good candidate for studying the physical effects that non-Newtonian rheology has on microswimming. In addition to the biomacromolecules in mucus, there are various proteins and salts that a biological microswimmer can often interact with via some biological process. For example, there may be something in the solution that the microswimmer can consume, which causes the microswimmer to swim more quickly than in a Newtonian 'no-growth' medium which lacks nutrients. Any measurement of the swimming speed of a microorganism in such a fluid is a measurement of biological, over physical, effects. Moreover, it is often difficult to control and indeed characterise the rheology of these biological complex fluids.

Thus, if we want to understand how the rheology of complex fluids affects microswimming, we should perform experiments on microswimmers in better understood fluids. Some of the most studied complex fluids are synthetic polymer solutions and they are often used when studying microswimmers. Polymers are macromolecules that are created by a process called polymerisation. They can either be created synthetically or by a biological polymerisation process.

Solutions containing these macromolecules exhibit non-Newtonian behaviour just like biological complex fluids. However, the rheological properties of synthetic-polymer solutions are much more easily controlled and characterised. Moreover, the use of synthetic-polymer solutions makes it easier to separate biological and physical effects. As such, this thesis focuses on understanding experiments of microswimmers in synthetic-polymer solutions; but we hope that the understanding developed can help to explain the behaviour of microswimmers in biological complex fluids.

In this section we will familiarise the reader with the structure and dynamics of polymers in solution and the rheology of polymer solutions. For more a more detailed discussion of the rheology and structure of polymer solutions see [66, 67].

1.2.1 The structure and dynamics of polymers

Complex fluids have internal degrees of freedom that interact with the flow of the fluid. It is these interactions that give rise to the observed non-Newtonian rheology of complex fluids. For polymer solutions, these internal degrees of freedom are the spatial conformations of the polymers. The polymer conformations couple to the fluid flow for the following reasons: (i) any velocity gradients in the fluid flow will stretch polymers, changing their spatial conformation; and (ii) any changes in spatial conformation of the polymers will drag nearby fluid, inducing a flow field.

The rheological behaviour of polymer solutions is thus governed by how the conformation of polymers in solution change. This is particularly important when studying microswimmers because, shown below, the size of polymers in solution can often be similar to the thickness of microorganisms' flagella. This calls into question the validity of coarse-grained continuum models when studying flagellated microswimmers in complex fluids. We will explore this methodological concern in Chapter 4. Furthermore, the size of these polymers in relation to the swimmer highlights the crucial importance of complementing any continuum model of the fluid with a robust understanding of the structures of polymer solutions, which we address in the following.

The structure of polymers

Polymers are large chain-like molecules created by a process called polymerisation. Many, often organic, molecules can form bonds with copies of themselves. Such molecules can undergo various polymerisation reactions resulting in large molecules comprised of many copies of the original molecule. These large molecules are known as polymers and the original molecules are known as monomers. For example, the monomer ethylene ($CH_2{=}CH_2$) can polymerise to form the polymer polyethylene ($-\!\!\left[CH_2-CH_2 \right]\!\!-_n$).

The degree of polymerisation of a given polymer chain is the number of monomer units which reacted together to make the chain. This number typically ranges from 20–10^{10}. Often, the molecular weight M_w of the polymer is used as a more experimentally accessible proxy for the degree of polymerisation. These weights typically range from 10^3–10^{12} Da. During a polymerisation reaction, the polymers created will not have the same degree of polymerisation, or equivalently the same molecular weight. In fact, there is a distribution of molecular weights in the sample, which depends on the specifics of the polymerisation process. The width of the molar mass distribution is estimated by the polydispersity index, p, which is defined as the ratio of the weight- and number-averaged molar masses of the polymers. For all samples of polymers, $p \geq 1$ with $p = 1$ corresponding to a monodisperse sample.

If each monomer can react with exactly two other monomers, then the resulting polymer either forms a linear chain or, in some cases, a ring. However, if a monomer can bond with more than two other monomers, then it is possible to create branching polymers. The branches can either be randomly placed along the length of the polymer chain, or there can be some pattern to their placement. The branch arrangements depend on the chemistry of the monomers and on the specifics of the polymerisation process. Also, cross-links can form between different polymer chains, joining them into a single molecule. If the degree of cross-linking is large enough, then all the polymer chains can be cross-linked into a single macroscopic molecule, known as a polymer network.

Monomers do not have to be identical to form polymers, some polymers are constructed from a few different monomers. Such polymers are known as heteropolymers. The different monomer types in a heteropolymer can be arranged randomly or following some pattern. For example, there are: (i) alternating heteropolymers; (ii) block heteropolymers, where two chains of each type of monomer are joined together; (iii) graft heteropolymers, where one monomer species forms branches on the backbone consisting of the other monomer species; and (iv) proteins are heteropolymers created from 20 different types of monomer known as amino acids. The amino acids of a protein are arranged to the specification provided by the organism's DNA.

Often, these polymers can be dissolved in some solvent. The resulting solution is a complex fluid with non-Newtonian rheological properties. The conformation and dynamics of the polymers in solution depends on many factors, including: the chemistry of the polymer, the degree of polymerisation, the degree of branching, the degree of cross-linking, the concentration of the solution, the polydispersity of the solution and the quality of the solvent. However, much of the non-Newtonian behaviour of polymers in solution can be understood without a detailed knowledge of the conformation of the polymers. Rather, all that is required is the knowledge that said conformations can change and that these changes take place over a characteristic timescale. This is known as the relaxation time of the fluid.

To make this more concrete, for the remainder of the subsection, we will discuss the dynamics of the simplest polymers in solution: monodisperse flexible linear polymers.

The dynamics of polymers in solution

Flexible linear polymers in a solution at rest undergo a random walk due to the thermal motions of the fluid. This leads to them forming coil-like conformations. In velocity gradients, the conformation of the polymer coils will change to minimise the free energy of the system. We can estimate the relaxation time λ taken by the polymers to change their conformation, using the polymers' self-diffusion time. The self-diffusion time of a polymer is the time it takes for the polymer to diffuse, due to thermal motions in the fluid, by a distance equal to its size. The size of the polymer coils is characterised by their radius of gyration, R_g. The radius of gyration depends on the molecular weight and chemistry of the polymer, the concentration of the solution and the quality of the solvent. R_g can vary from 10–1000 nm.

The change in conformation does not have to happen for the entire chain. In fact, any section of the chain can change conformation. The chain is self-similar such that the process for this shorter piece of the chain is the same as the process for the whole chain. Thus, we have a range of relaxation times, the longest corresponding to the entire chain relaxing and the shortest to a single repeat unit relaxing. Often, the rheological behaviour of a fluid is well characterised by solely considering the longest relaxation time. Thus, here, we only discuss these longest relaxation times.

Solutions of high molecular-weight polymers are often entangled. Entanglements are topological constraints on the motion of a polymer due to the other polymers in the solution. The exact nature of entanglements and the dynamics of entangled polymer solutions is poorly understood [66, 67]. However, the presence of entanglements does lead to different dynamics than those of unentangled polymer solutions. Here, we just discuss the better understood dynamics of unentangled polymer solutions.

Polymer solutions can be in one of three regimes, depending on their concentration: (i) dilute; (ii) semidilute; and (iii) concentrated. In each of these regimes, the dynamics of the polymers and their self-diffusion times vary. In dilute solutions, polymer coils are isolated from each other and strong hydrodynamic interactions dominate the dynamics. In concentrated solutions, the polymer coils are completely interpenetrating; and, as a result, screen each other from these hydrodynamic interactions. In the semidilute regime there is only partial interpenetration and thus, partial hydrodynamic screening. As such, semidilute solutions interpolate between these two extremes.

In dilute polymer solutions, polymers experience excluded-volume effects and undergo self-avoiding random walks to find their at-rest configurations. Thus, their radius of gyration scales as $R_g \sim M_w^\nu$, where ν is the swelling exponent and M_w is the molecular weight of the polymer. In a good solvent, where polymer-solvent interactions are preferable to polymer-polymer interactions, $\nu = 3/5$. The dynamics of polymers in these dilute solutions are described by the Zimm model [67]. Due to hydrodynamic interactions, as the polymer diffuses, it drags some of the solvent with it. Thus, we can approximate the self-diffusing polymer as a sphere of solvent, with a radius of R_g being dragged through the fluid. The drag coefficient, ζ, for such a sphere in a Stokes flow scales as $\zeta \sim R_g$; and the time, λ, it takes for the sphere to diffuse a distance R_g scales as

$$\lambda \sim R_g^2 \zeta \sim R_g^3 \sim M_w^{3\nu}. \tag{1.6}$$

In concentrated solutions, excluded-volume effects are screened and polymers undergo ideal random walks to find their at-rest configuration. Thus, their radius of gyration scales as $R_g \sim M_w^{1/2}$. The dynamics of polymers in concentrated solutions are governed by the Rouse model [67]. Hydrodynamic interactions are screened by the presence of other polymers. As a result, each monomer of the polymer can diffuse independently. The number of monomers in each polymer scales as the molecular weight of the polymer. And each monomer has to diffuse a distance R_g. Thus, the relaxation time scales as

$$\lambda \sim M_w R_g^2 \sim M_w^2. \tag{1.7}$$

In semidilute solutions, hydrodynamic interactions are partially screened. In this regime, each polymer can be thought of as a chain of "blobs", each blob containing many monomers. Inside the blob, there is no hydrodynamic screening; and monomers must drag the solvent with them. However, there are no hydrodynamic interactions between the blobs; and thus, the dynamics of the chain of blobs is described by the Rouse model. Scaling analysis [67] shows that in this scenario, the relaxation time behaves as

$$\lambda \sim M_w^2 c^\alpha \tag{1.8}$$

where c is the concentration of the polymers in solution and $\alpha = (2 - 3\nu)/(3\nu - 1) = 1/4$ for a good solvent.

The Zimm relaxation time of a polymer is shorter than its Rouse relaxation time. The longest relaxation time of an unentangled polymer solution increases slowly with increasing concentration, from the Zimm relaxation time of dilute polymer solutions to the Rouse relaxation time of concentrated solutions.

This have been a very brief glimpse at the large variety of chemical structures and dynamics of polymers in solution. Despite this complexity at the microscopic scale, the behaviour of polymer solutions at a macroscopic scale is surprisingly universal. As we have already stated, this universal behaviour is characterised by the relaxation times discussed above.

1.2.2 The rheology of polymer solutions

Polymer solutions are often viscoelastic, in that they share properties with viscous fluids and elastic solids. When a constant shear stress is applied to an elastic solid, the solid will respond with a constant shear strain. Whereas, when a constant shear stress is applied to a viscous fluid, the fluid will respond with a constant shear strain $r$ate. In situations such as that described above, viscoelastic substances behave like viscous fluids at long timescales and elastic solids at short timescales.

We can understand this behaviour in terms of the changing conformation of polymers in solution discussed in the previous section, as follows. Consider a polymer solution at rest. At some time $t = 0$, we begin to shear the solution at a constant rate. At short timescales, the polymers have yet to change conformation to match their new flow environment. As the polymers resist the change, the fluid as a whole behaves elastically. At longer timescales, the polymers have reached their new conformation and are simply advected by the flow. As such, the fluid as whole responds viscously.

This simple picture of polymer solutions suggests that the boundary between short and long timescales is defined by the longest relaxation time λ from Section 1.2.1, which governs the time it takes of the polymers to change conformations. Experiments have shown that this is indeed the case [66]. For the remainder of this subsection, we describe various phenomena that viscoelastic fluids exhibit and how they relate to the relaxation time. For a more detailed discussion of the viscoelasticity of polymer solutions see [66].

Many rheological experiments consist of inducing simple flows in a fluid and measuring the fluid's stress response. In what follows, we discuss: (i) The complex viscosity of a viscoelastic fluid in small-amplitude oscillatory shear. Understanding this will help us understand Taylor's sheet, which at small-amplitudes can be interpreted as a complicated oscillatory shear probe. (ii) The normal stress differences of viscoelastic fluids in constant shear, which is a marker of elasticity in the fluid. This is the main focus of this thesis. And (iii) shear-thinning phenomena of viscoelastic fluids at high shear-rates. We will exclude these effects from our analysis of microswimming in complex fluids. However, an understanding of shear thinning is required in order to interpret experiments.

Oscillatory shear strain

One of the clearest demonstrations of the combined viscous and elastic behaviours of polymeric solutions is the response of such fluids to oscillatory shear strain. Consider a polymer solution between two plates. We oscillate the top plate backwards and forwards at a frequency ω such that, at a time t, the fluid experiences a shear strain rate $\dot{\gamma}$, given by

$$\dot{\gamma} = \dot{\gamma}_0 \sin(\omega t). \tag{1.9}$$

Here, the amplitude of the oscillation $\dot{\gamma}_0/\omega$ is taken to be small, such that the polymers in the fluid do not deviate much from their at-rest conformations. This is known as the linear viscoelastic regime. If the polymer solution is a viscous fluid, we would expect the shear stress σ, applied to the plates, to be proportional to this strain rate. Whereas, for an elastic solid, we expect the shear stress to be proportional to the strain $\gamma = -\dot{\gamma}_0 \cos(\omega t)/\omega$. For viscoelastic fluids in the linear regime, we find a superposition of these two behaviours with σ, given by

$$\sigma = \dot{\gamma}_0 \left(\eta' \sin(\omega t) + \eta'' \cos(\omega t) \right). \tag{1.10}$$

Here, $\eta^* = \eta' - i\eta''$ is the complex viscosity of the fluid. The viscous response of the fluid is characterised by η' and the elastic response is characterises by η''. This complex viscosity is a fluid-centric view of the viscoelastic behaviour. Alternatively, the complex modulus $G^* = i\omega\eta^* = G' + iG''$ is often used for making comparisons to solids. $G' = \eta''\omega$ is known as the storage modulus and $G'' = \eta'\omega$ is the loss modulus.

The complex viscosity depends on the frequency of the oscillation due to the dynamics of the polymers in solution. For example, Zimm theory, which accounts for all the relaxation modes of the polymers, predicts that for a dilute polymer solution, there are three different frequency regimes. At low frequencies (or long timescales), we find η' is constant and $\eta'' \sim \omega \ll \eta'$, which is viscous behaviour for the fluid. At moderate frequencies (or moderate timescales), we find $\eta' - \eta_s \sim \eta'' \sim \omega^{(1-3\nu)/(3\nu)}$, where η_s is the viscosity of the solvent and ν the swelling exponent [67]. At even higher frequencies (or short timescales), the polymers do not have time to react to the oscillatory shear. In this regime, the polymers do not contribute to the viscosity of the fluid, but instead resist the motion elastically. Thus, at high frequencies we have $\eta' - \eta_s = 0$ and $\eta'' \sim \omega^{-1}$ [66].

The boundary between these frequency regimes is determined by the relaxation times of the polymers, that is, the transition from the low to moderate frequency regimes occurs at $\omega = 1/\lambda$, where λ is the longest Zimm relaxation time in Eq. (1.6). Whereas, the transition from moderate to high occurs at $\omega = 1/\lambda_0$, where λ_0 is the shortest relaxation time in the fluid associated with a single repeat unit relaxing. Experimental evidence supports this frequency dependence of the complex viscosity of dilute polymer solutions [66].

Normal stress differences

Consider a fluid undergoing a simple shear in the xy-plane such that the velocity field in the fluid is given by $\boldsymbol{u} = \dot{\gamma} y \boldsymbol{e}_x$. If the fluid is Newtonian the total stress $\boldsymbol{\Sigma}$, is given by

$$\boldsymbol{\Sigma} = -p\mathbf{1} + 2\eta\mathbf{D} = \begin{pmatrix} -p & \eta\dot{\gamma} & 0 \\ \eta\dot{\gamma} & -p & 0 \\ 0 & 0 & -p \end{pmatrix}, \tag{1.11}$$

where $\mathbf{1}$ is the identity matrix and $\mathbf{D} = (\nabla\boldsymbol{u} + \nabla\boldsymbol{u}^T)/2$ is the rate of strain tensor. Here $(...)^T$ denotes a transpose. For this Newtonian fluid in shear flow, the only contribution to the normal components of the fluid stress are the isotropic contributions of the pressure. In contrast, a viscoelastic fluid in shear flow has additional non-isotropic contributions to the normal stresses.

The normal stress components (Σ_{xx}, Σ_{yy}, Σ_{zz}) cannot be measured directly, because the pressure field is only defined up to an additive constant. Instead, measurements are made of the normal stress differences $N_1 = \Sigma_{xx} - \Sigma_{yy}$ and $N_2 = \Sigma_{yy} - \Sigma_{zz}$. At low shear rates $\dot{\gamma}$, the polymers in the fluid are close to their at-rest configurations. In this regime, the first and second normal stress differences scale as $N_1, N_2 \sim \dot{\gamma}^2$. This leads to the definition of the normal stress coefficients, $\Psi_1 = N_1/\dot{\gamma}^2$ and $\Psi_2 = N_2/\dot{\gamma}^2$.

In addition to creating first normal stress differences, introducing polymers to a solution also increases the fluid viscosity. This viscosity is increased from the viscosity η_s of the pure solvent by some polymeric contribution $\eta_p = \eta - \eta_s$.

Simple kinetic theories predict that $\Psi_1 = 2\eta_p\lambda$ and $\Psi_2 = 0$ [68]. Experiments for dilute polymeric solutions find that Ψ_1 is a positive constant and that Ψ_2 is small and negative at low shear rates [66]. The relation $\lambda = \Psi_1/(2\eta_p)$ is often used to obtain the relaxation time of the fluid experimentally.

The presence of normal stress differences is an indication of the elastic behaviour of the fluid. To understand why they occur, consider the following. As a response to the velocity gradients in the shear flow, the conformation of polymers changes from a statistically isotropic coil to a new configuration aligned, on average, with the flow. This breaks the isotropy of the fluid and is responsible for the anisotropic normal stresses.

Shear thinning

In a low shear-rate shearing flow, the polymers in the fluid do not change substantially from their at-rest configurations. When shear-rate increases, the deformations in the fluid become large enough that the dynamics of the polymers change substantially. This leads to changes in the rheological behaviour of the fluid. In polymer solutions the most common type of changes are known as shear thinning.

Shear thinning occurs for both the shear viscosity of the fluid and the first normal stress coefficient. At low shear rates $\dot{\gamma}$, both the viscosity of the fluid η and the first normal coefficient Ψ_1 are constant. However, at shear rates $\dot{\gamma} > 1/\lambda$, both

η and Ψ_1 decrease with $\dot{\gamma}$, typically by a power law [66]. This is known as shear thinning. It is the polymeric contribution to the viscosity η_p that shear thins, thus $\eta \geq \eta_s$ at all shear rates. Due to the use of Ψ_1 in determining the relaxation time of the fluid, shear thinning of the first normal stress coefficient is often interpreted as shear thinning on the relaxation time of the fluid.

We have just outlined a small sample of the many types of rheological behaviour observed in polymer solutions. A real fluid exhibits all of these phenomena. However, in order to mechanistically explain the swimming of microorganisms in complex fluids we need to isolate those aspects of viscoelasticity which are most relevant to the problem. Here, we propose to do so by isolating a single aspect, namely, the presence of first normal stress differences in shear flow, which is an indication of the presence of elasticity in the fluid. We will consider fluid elasticity in the absence of shear thinning — as this is a separate viscoelastic effect.

1.2.3 A mathematical fluid: The Oldroyd-B model

The Oldroyd-B model [68] is the simplest model of a viscoelastic fluid that predicts first normal stress differences in shear flows. The model prescribes an alternative to the constitutive equation for the total stress in a Newtonian fluid. We introduce the polymeric stress tensor $\boldsymbol{\tau}$ to account for the contribution to the total stress $\boldsymbol{\Sigma}$, made by the polymers in solution. Thus, we have

$$\boldsymbol{\Sigma} = -p\mathbf{1} + 2\eta_s\mathbf{D} + \boldsymbol{\tau}, \tag{1.12}$$

where η_s is the viscosity of the solvent.

We are only concerned with low Reynolds-number fluids. Therefore, we can neglect inertial terms and our governing equations are the incompressibility of the fluid and local force balance. In addition to these equations, we need constitutive equations for the newly introduced $\boldsymbol{\tau}$. For an Oldroyd-B fluid, these constitutive equations are the upper-convected Maxwell equations of each of the components of the polymer stress. Thus, we have the Stokes-Oldroyd-B equations which are given by

$$\nabla \cdot \boldsymbol{\Sigma} = -\nabla p + \eta_s \nabla^2 \boldsymbol{u} + \nabla \cdot \boldsymbol{\tau} = \boldsymbol{0}, \tag{1.13a}$$

$$\nabla \cdot \boldsymbol{u} = 0, \tag{1.13b}$$

$$\boldsymbol{\tau} + \lambda \overset{\triangledown}{\boldsymbol{\tau}} = 2\eta_p \mathbf{D}. \tag{1.13c}$$

Here, λ is the longest relaxation time in the fluid, η_p is the polymeric contribution to the viscosity and

$$\overset{\triangledown}{\boldsymbol{\tau}} = \partial_t \boldsymbol{\tau} + \boldsymbol{u} \cdot \nabla \boldsymbol{\tau} - \nabla \boldsymbol{u}^T \cdot \boldsymbol{\tau} - \boldsymbol{\tau} \cdot \nabla \boldsymbol{u}$$

is the upper-convected derivative of $\boldsymbol{\tau}$. The upper-convected derivative is the Galilean-invariant time derivative of a second-rank tensor being moved by some velocity field $\boldsymbol{u}$.

In an analogy to the Reynolds number, another dimensionless number is used to characterised flows in Oldroyd-B fluids, the Deborah number. The Deborah number is defined as $\mathrm{De} = \lambda/T$ where T is the characteristic time of the fluid flow. Two situations with the same geometry and Deborah number result in the same fluid flow. Thus, to explore microswimmers in viscoelastic fluids we either vary the relaxation time λ of the fluid, or the kinematics of the swimmers, which are characterised by T.

There is a simple kinetic model, known as the elastic dumbbell model, which, when coarse grained, produces the Oldroyd-B equations, see Bird et al. [69] for details. In this model, pairs of beads joined by Hookean springs are suspended in the fluid. These “elastic dumbbells” interact with the fluid flow by stretching and relaxing. Other, more complicated, kinetic models of viscoelastic fluids produce the Oldroyd-B model with additional higher order terms when coarse grained. These higher order terms correspond to changes to the dynamics of the viscoelastic agents as they change conformation. The elastic dumbbell model and the Oldroyd-B model ignore such changes in dynamics. For example, if we think about the dumbbells, the force required to stretch the spring by some displacement $\Delta \boldsymbol{R}$ is independent of the initial length of the spring $\boldsymbol{R}$. Thus, this model neglects any changes to the dynamics of the viscoelastic agents as a result of changes to their conformation.

Although the dumbbell model is a pretty poor approximation of the structure of real polymer solutions, it does provide a useful visualisation tool for the polymeric stresses in the fluid. Throughout this thesis, we use dumbbells to represent components of the polymeric stress in schematics of what is happening in fluid around our microswimmer. It is important to remember that these dumbbells do not represent constituents of the fluid, but merely components of the polymeric stress tensor $\boldsymbol{\tau}$.

Due to the assumption of the viscoelastic agents in the fluid having conformation independent dynamics, the Oldroyd-B model fails to predict shear-thinning behaviours in the fluid. In shear flows, the viscosity is given by $\eta = \eta_s + \eta_p$ and the first normal stress coefficient is given by $\Psi_1 = 2\eta_p\lambda$ independent of the shear rate. Also, in extensional flows, the Oldroyd-B model predicts infinite extensional stresses for finite extensional strain rates, $\dot{\epsilon} > \dot{\epsilon}_c = 1/(2\lambda)$ [69]. In terms of the dumbbell model, the dumbbells become infinitely extended, which results in the infinite extensional stress in the fluid. As we will show in Chapter 2, there are stagnation points around the sheet where the flow is extensional. However, the extension stresses never diverge at such points. Thus, the solution to the Oldroyd-B equations are finite around Taylor's sheet and we can ignore this concern.

The Oldroyd-B model predicts [69] that the components of the complex viscosity in oscillator shear flow, which were defined in Eq. (1.10), are given by

$$\eta' = \eta_s + \frac{\eta_p}{1+\lambda^2\omega^2}, \tag{1.14a}$$

$$\eta'' = \frac{\eta_p\lambda\omega}{1+\lambda^2\omega^2}. \tag{1.14b}$$

For $\omega \ll 1/\lambda$, we have $\eta' \approx \eta_s + \eta_p$ and $\eta'' \sim \omega$ which is the expected viscous behaviour. Whereas, for $\omega \gg 1/\lambda$ we have $\eta' \approx \eta_s$ and $\eta'' \sim \omega^{-1}$. This is elastic behaviour where viscoelastic agents in the fluid do not have time to react to the oscillatory shear flow. As we will see in Chapter 2, at small wave amplitudes Taylor's sheet generates stresses in the fluid that are analogous to this oscillatory shear response.

Using the Oldroyd-B equation allows us to consider the effects of elasticity in the fluid, in the absence of any shear-dependent viscosity. This can also be done experimentally, using what are known as Boger fluids. Over an appropriate range of shear rates, Boger fluids have shear-independent viscosities. This allows them to be used experimentally to investigate the effects of elasticity in the absence of shear-thinning — just like the Oldroyd-B model. However, to truly be modelled by the Oldroyd-B equations, a Boger fluid must also have a shear-independent relaxation times. Typically, this is much harder to achieve than shear-independent viscosities, and as such, Boger fluids often have relaxation times that shear thin at shear rates characteristic of the experiment. However, we can still expect qualitative agreement on the effects of fluid elasticity in fluid on microswimming when comparing theoretical results from the Oldroyd-B equation and experimental results using Boger fluids. For more information about Boger fluids see [70].

Now we have developed an understanding of both microswimming and complex fluids, we discuss the various experiments on microswimmers in complex fluids before defining the research questions of this thesis.

1.3 Microswimming in complex fluids: experiments and observations

Often, experiments of microswimmers in complex fluids try to determine whether viscoelasticity helps or hinders the swimmer. As we have already stated, it is difficult to control the rheological behaviour of biological complex fluids; and so experiments are typically performed with synthetic polymer solutions. Some experiments use biological microswimmers, despite the fact it is impossible to directly control the kinematics of these biological microswimmers. It has been shown that *C. elegans* [48], spermatozoa [71] and *E. coli* [72] change the rate that they perform their swimming stroke when swimming through Newtonian fluids of different viscosities. Thus, care must be taken to ensure microswimmers have the same swimming kinematics when making comparisons of swimming in different fluids. To avoid this issue, others have used macroscopic model swimmers where they can control the swimming kinematics directly. These engineered swimmers must be force-free if they are to accurately model a microswimmer.

This section gives an overview of some of these experiments.

Liu et al. [18] have performed experiments using a macroscopic rigid helix as a model swimmer. They rotated the helix at a rate Ω in a bucket of high-viscosity fluid. To simulate force-free swimming, they moved the helix vertically through the fluid at a speed V, selected so that the helix experiences no net hydrodynamic force. Liu et al. performed this experiment in a high-viscosity Newtonian fluid and Boger fluids made with different concentrations of 420 kDa

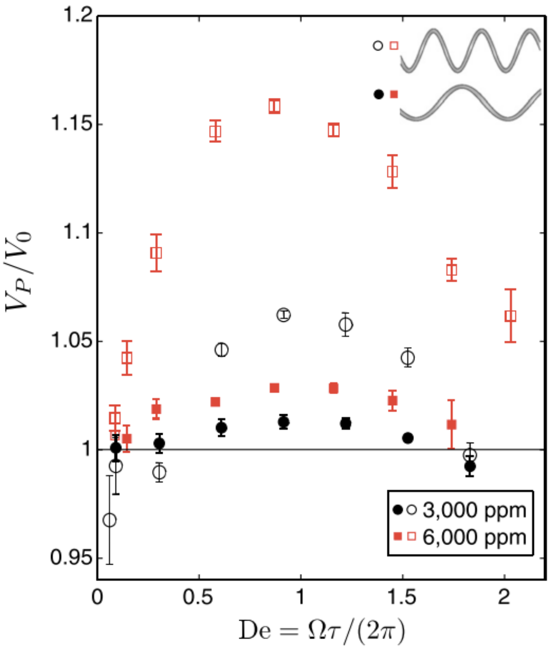

Figure 1.5 The swimming speed V_p against Deborah number De for helices in PIB-PB Boger fluids of different concentrations of PIB. The swimming speeds are scaled by the swimming speed V_0 of the same helix in a high-viscosity Newtonian fluid. The upper and lower helices have a pitch angle of 0.38π and 0.27π, respectively. See the text for more details. Adopted from [18].

polyisobutylene (PIB) in polybutene (PB). These Boger fluids have relaxation times of $\tau \approx 0.6\,\mathrm{s}$. For a given rotation rate they measured the speed V_0 required for force-free swimming in a Newtonian fluid and the speed V_p required in the Boger fluid. As shown in Fig. 1.5, they found that V_p/V_0 initially increases with Deborah number $\mathrm{De} = \tau\Omega/(2\pi)$, reaching a peak at $\mathrm{De} \approx 1$ before decreasing. In some cases, they found $V_p < V_0$. They also found that the peak in V_p/V_0 was enhanced for larger concentrations of PIB and larger pitch angles of the helix. This experiment suggests that helices can swim faster or slower in viscoelastic fluids depending on the geometry and rotation rate of the helix. This result is in agreement with the theoretical results of large amplitude helices in complex fluids found by Spagnolie et al. [27].

Martinez et al. [19] have investigated swimming based on rotating helices in viscoelastic fluids on a microscopic scale using the bacteria *E. coli*. As we have seen in Section 1.1.2, these bacteria swim by rotating helical flagella bundles at the pole of the cells. In order to be instantaneously torque-free, the cell body of a bacterium rotates in the opposite direction to the bundle. It is easier to measure the rotation rate of the cell body directly than that of the flagella bundle because the body is larger. Berg and Turner [72] showed that the body rotation rate decreases with the viscosity of the fluid the bacteria is swimming through. Purcell's [9] simple model for an *E. coli* bacterium consisting of an ellipsoidal cell-body with a single polar helical flagellum predicts that the swimming speed v of *E. coli* is proportional to the rotation rate of the cell

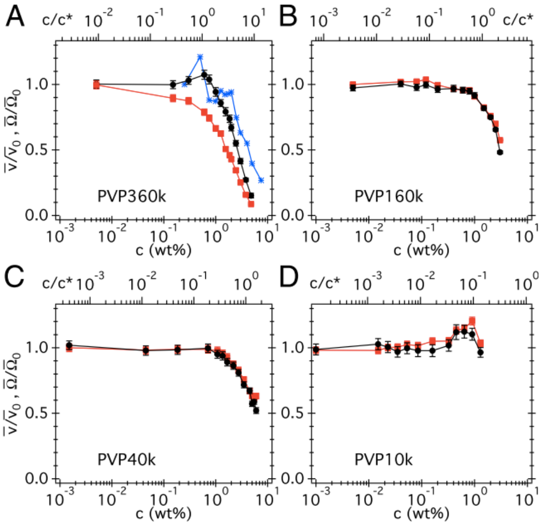

Figure 1.6 The average swimming speed $\bar{v}$ (black circles) and average body rotation rate $\bar{\Omega}$ (red squares) against concentration c for *E. coli* in solutions of different molecular-weight PVP. The swimming speeds and rotation rates are scaled by their values, $\bar{v}_0$ and $\bar{\Omega}_0$ respectively, at $c = 0$. In lower molecular-weight solutions the *E. coli* behaved as if they were swimming in a Newtonian fluid. For 360 kDa, there are non-Newtonian effects present and the *E. coli*, with fixed kinematics, swim faster than they would in a Newtonian fluid. See the text for more details. The blue stars are data from [73]. Adopted from [19].

body Ω in Newtonian media. Any deviation from this behaviour is evidence of non-Newtonian effects influencing the swimming of the bacteria. As shown in Fig. 1.6, Martinez et al. found that *E. coli* swimming in low molecular-weight dialysed polyvinylpyrrolidone (PVP) solutions behave as if swimming through a Newtonian fluid. That is $\bar{v}/\bar{v}_0 = \bar{\Omega}/\bar{\Omega}_0$ for all PVP concentrations c. Here, $\bar{v}_0$ and $\bar{\Omega}_0$ are the swimming speed and rotation rate in pure solvent ($c = 0$); while the bars represent averages over $\approx 10^4$ bacteria.

However, Martinez et al. also found that for 320 kDa PVP solutions $\bar{v}/\bar{v}_0 > \bar{\Omega}/\bar{\Omega}_0$ over a range of c. This suggests that, for a given rotation rate Ω, the non-Newtonian properties of the fluid enhance the propulsion of *E. coli* compared to swimming in a Newtonian fluid. Martinez et al. explained their data by considering the interaction of the polymers in solution with the flagella bundle of the bacteria, which are of similar size. This has inspired Chapter 4 of this thesis, where we will discuss their mechanism in more detail.

Shen and Arratia [20] have investigated the swimming of the nematode *C. elegans* in 700 kDa carboxymethyl cellulose (CMC) solutions of various concentrations c. Recall that nematodes are small worms that swim by propagating planar waves along their length, similar to the Taylor sheet model we described in Section 1.1.3. The CMC solutions considered are viscoelastic with shear-rate independent viscosities. By varying the concentration c, Shen and Arratia were

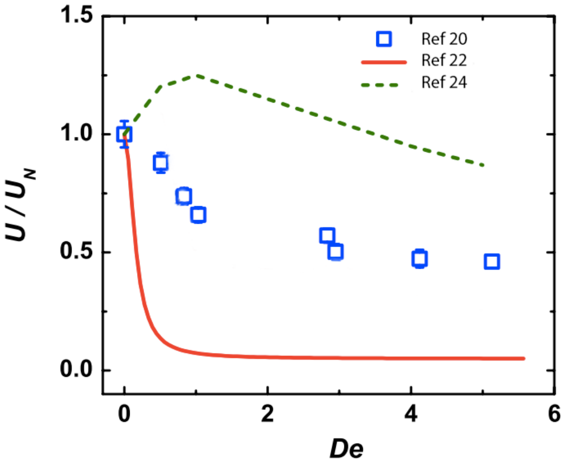

Figure 1.7 The average swimming speed U against Deborah number De for *C. elegans* (symbols) in CMC solutions. The swimming speeds are scaled by the swimming speed U_N of the nematode in a Newtonian fluid of the same viscosity. The solid line is the swimming speed predicted for Taylor's waving sheet in an Oldroyd-B fluid found by Lauga [22], with the same parameters as the CMC solution. The dashed line is the swimming speed found by Teran et al. [24] for a finite sheet. See the text for more details. Adopted from [20].

able to control the relaxation time λ (0.4–5.6 s) of the fluid. They found that the kinematics of the nematode were the same in the CMC solution as in a Newtonian fluid of the same viscosity. However, as shown in Fig. 1.7, the swimming speed U of the *C. elegans* in the CMC solution was less than the swimming speed U_N in a viscosity-matched Newtonian fluid. Furthermore, they found that U/U_N decreased with $\mathrm{De} = \lambda f$, where f is the frequency of the wave, reaching a plateau swimming speed at larger Deborah numbers.

Shen and Arratia's results are in qualitative agreement with small-amplitude analytical calculations by Lauga [22] and finite-amplitude numerical calculations by Li and Ardekani [23] of Taylor's infinite waving sheet in an Oldroyd-B fluid. However, numerical calculations of a finite waving sheet made by Teran et al. [24] find that the U/U_N initially increases with an increasing Deborah number, prior to decreasing to values below unity. We attempt to provide a mechanistic understanding of Shen and Arratia's results in Chapter 2.

Dasgupta et al. [21] have performed experiments with a macroscopic version of Taylor's waving sheet using an elastic sheet wrapped into a cylinder with a radius of ≈5.7 cm and suspended vertically in a cylindrical tank of fluid with a radius of ≈10.15 cm. Whereas the infinite periodic waving sheet swims laterally by propagating transverse waves along its length, the cylindrical sheet swims in a

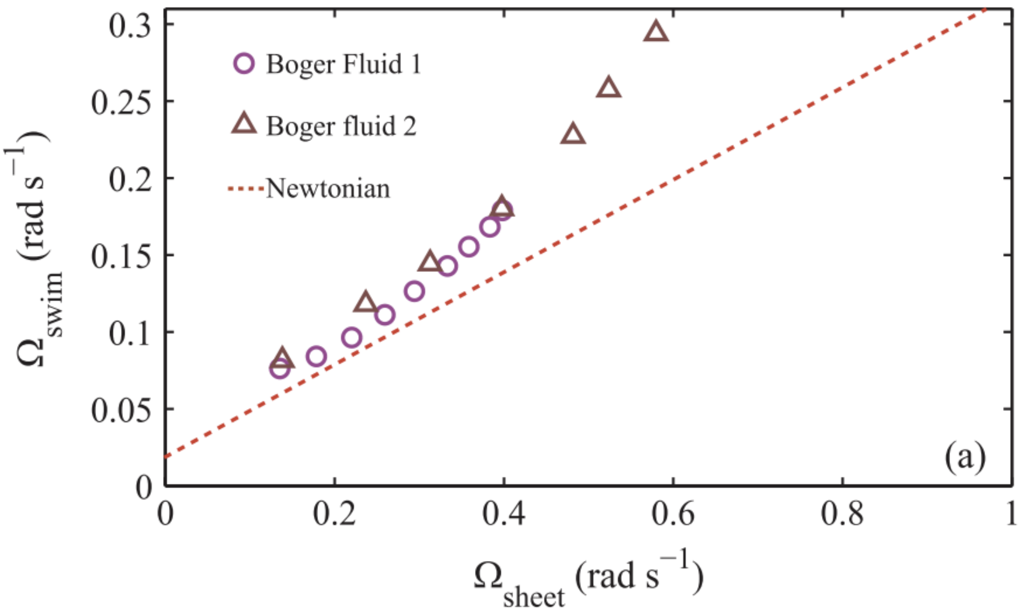

Figure 1.8 The angular swimming speed Ω_{swim} against rotation rate Ω_{sheet} for a cylindrical Taylor's sheet in Boger and Newtonian fluids. The swimming speeds of the sheet are faster in Boger fluids than Newtonian fluids. See the text for details. Adopted from [21].

circle as Dasgupta et al. propagate transverse waves around its circumference. To create the waves, Dasgupta et al. deform the sheet into an ellipse and rotate it with a motor at a speed Ω_{sheet}. Both the tank and the motor housing are on bearings so that the whole apparatus can rotate freely. When the motor is turned on, the tank rotates in the same direction as the sheet at a rate of Ω_{tank}, in order to minimise the torque acting on the tank. As the apparatus is isolated by the bearings, the cylindrical sheet is also torque-free, which is the angular analogue of the force-free condition we require for a true swimmer.

The angular swimming speed of the sheet is then $\Omega_{\text{swim}} = \Omega_{\text{sheet}} - \Omega_{\text{tank}}$. Dasgupta et al. measure the angular swimming speed of their cylinder swimmer in a high viscosity Newtonian fluid and a Boger fluid, polyacrylamide in corn syrup. As shown in Fig. 1.8, they find that the cylindrical sheet swims more quickly in the Boger fluid than the Newtonian fluid over a small range of Ω_{sheet} (0.1–0.6 rad s^{-1}). This is contrary to the theoretical behaviour of a planar-infinite waving sheet, which swims more slowly in an Oldroyd-B fluid [22]. Dasgupta et al. demonstrate that at the operating conditions of their apparatus, the first normal stress coefficient $\Psi_1 \sim \Omega_{\text{sheet}}^{-1}$, so their Boger fluids deviate from the Oldroyd-B model. However, this does not explain the qualitatively different behaviour from

Lauga's infinite sheet calculation found by Dasgupta et al. for the cylindrical sheet. In Chapter 3 we consider Taylor's waving sheet swimming in an Oldroyd-B fluid next to a wall and show that in some circumstances, elasticity can increase the sheet's swimming speed. Dasgupta et al.'s cylindrical sheet is somewhat confined and perhaps this is the origin of the qualitatively different behaviour.

1.4 Research Questions

As we have seen from the experimental and theoretical results discussed so far, there is a wide variety of behaviour observed and predicted for microswimmers in complex fluids. These behaviours seem to depend on the geometry of the swimmer, its gait and the rheology of the fluid. There has been little effort in trying to understand why these different behaviours are observed, in a mechanistic sense. In this thesis, we attempt to begin to do this by focussing on how the elasticity of the fluid affects planar-wave swimmers. This is arguably a investigation into the mechanism of propulsion of the simplest swimmer in the simplest viscoelastic fluid. We hope that in doing so, we have paved the way for our mechanistic understanding to be extended to more complicated swimmers and/or fluids.

This thesis is structured as follows.

In Chapter 2, we begin by investigating the simplest situation of microswimming in complex fluids. We consider Taylor's waving sheet swimming through the bulk of an Oldroyd-B fluid. Lauga [22] has previously shown that at small wave amplitudes, the swimming speed of the sheet decreases with increasing Deborah number reaching a plateau swimming speed at large Deborah numbers. Using the small-amplitude solution to the problem, we propose a physical mechanism responsible for the slowing down of the sheet. We also provide an explanation for the origin of the plateau found by Lauga. In addition, we develop a numerical solver in order to find solutions to the problem at finite amplitudes. We then suggest how our small-amplitude mechanism is altered in these finite amplitude situations and use that to design a swimmer that swims faster in Oldroyd-B fluids.

As well as swimming in complex fluids, many biological microorganisms also swim in confined space. In Chapter 3, we consider Taylor's waving sheet swimming in an Oldroyd-B fluid next to a wall. Katz [74] found that, at small wave amplitudes, Taylor's sheet swims more quickly next to solid boundaries in Newtonian fluids. Also, Elfring and Lauga [75] have shown that, at small wave amplitudes, swimming next to a wall does not change the behaviour of Taylor's waving sheet in viscoelastic fluids. The swimming speed still decreases with Deborah number, tends to a plateau value at large Deborah numbers. Using small-amplitude analysis, we provide a mechanistic explanation for the increased swimming speed when next to a wall. We also show that the mechanism discussed in Chapter 2 is still present when swimming next to a wall. Furthermore, this explains why we observe the same behaviour of the swimming speed with regards to the relaxation time. We also adapt our numerical solver for the new geometry in order to solve the problem at finite wave amplitudes. We show that at large wave amplitudes, Taylor's sheets in strong confinement can, in fact, have an increasing swimming speed as a function of relaxation time.

The experiments by Martinez et al. discussed in Section 1.3 suggest that continuum models are not appropriate for describing flagellated microswimmers in complex fluids. Martinez et al. explain their results using a 'semi-continuum' Newtonian depletion region model. Inspired by this, we consider the effects of elasticity on such a depletion region model for Taylor's waving sheet in Chapter 4. We solve the problem both analytically for small-amplitudes and numerically at finite amplitudes. We find that when swimming with a depletion region, Taylor's waving sheet is either helped or hindered by the elasticity in the fluid, depending on the amplitude of the wave. This highlights how the behaviour of microswimmers in complex fluids is sensitive to the kinematics of the microswimmer in question. We show that the resulting swimming behaviour can be understood in terms of the mechanisms described in Chapters 2 and 3.

This concludes our attempt to mechanistically explain the behaviour of microswimmers in complex fluids. Chapter 5 looks at a different question related to microswimming. Whereas in the previous chapters, we prescribed kinematics to Taylor's sheet and investigated the resulting swimming behaviour. In Chapter 5, we ask what it is that prescribes the kinematics. We perform mathematical optimisations of a general fitness function for two model swimmers: Taylor's sheet and an infinite flexible flagellum. We compare the results of these mathematical optimisations with the results of the optimisation processes carried out by evolution, in order words, real biological swimmers. We show that care must be taken when choosing the fitness function to optimise if one wants to use mathematical optimisation as a metaphor for evolutionary processes. We also show that, for our model microswimmers, the often used hydrodynamic efficiency is a poor choice of fitness function when making a comparison to evolutionary processes.

Notes on the numerical solver

This note serves as an apology to the reader for the way in which we present the numerical solver in the chapters that follow. In order to aid reproducibility, the numerical method is spelled out in full in each chapter. Unfortunately, the numerical solver is sufficiently similar in each chapter that this is somewhat tedious. However, the numerical methods are also sufficiently different that providing a single description of the solver for all chapters would be unwieldy and confusing. We hope that the reader will understand the rationale and forgive us for the tedium. On the bright side, this might enable the reader to easily adapt the numerical solver to Taylor's waving sheet in other situations.

Chapter 2

Swimming in the bulk of a viscoelastic fluid

2.1 Introduction

As we have seen in Chapter 1, complex fluid environments exhibit non-Newtonian behaviours; and studies into microswimming in complex fluids tend to focus on whether these behaviours help or hinder the swimming of microorganisms. Remember that various experimental [18–21] and theoretical [22–27, 29, 31–33] studies have collectively shown that there is no universal answer to this question. Some microswimmers swim faster in complex fluids than in Newtonian fluids; while others are slower in complex fluids. However, this statement is just an observation. As discussed in Chapter 1, only a mechanistic explanation of their behaviour will allow us to understand microswimmers in complex fluids.

As we have seen in Section 1.2, there are many different types of non-Newtonian behaviour exhibited by complex fluids. One such behaviour is the presence of first normal stress differences in shearing flows, and this is what we focus on in this thesis. As discussed in Section 1.2.3, we use the Oldroyd-B model for the fluid to isolate the presence of first normal stress differences from shear-thinning effects. Also, as discussed in Section 1.1.3, we will be using a simple model swimmer, Taylor's waving sheet, which can be solved analytically in the small-amplitude limit.

Recall that Lauga's [22] analytical, small-amplitude calculation of Taylor's sheet in an Oldroyd-B fluid shows that the swimming speed of a sine-waving sheet decreases monotonically with an increasing Deborah number, tending to a constant swimming speed at large Deborah numbers. We will refer to this large Deborah number swimming speed as the “plateau” swimming speed. Li and Ardekani [23] showed that this result also holds at finite amplitudes, using numerical calculations. Furthermore, Shen and Arratia [20] have observed qualitatively similar behaviour for the waving worm-like microswimmer *C. elegans*. The quantitative discrepancies between the behaviour of *C. elegans* and Taylor’s waving sheet can probably be attributed to the geometrical differences between a finite worm and an infinite sheet. However, the similarity in both (i) their observed behaviour in viscoelastic fluids with shear-independent viscosities and (ii) their swimming kinematics suggests that there may be a common viscoelastic mechanism at play.

Shen and Arratia explained the slowing down of *C. elegans* in their polymer solution, by suggesting that around ‘hyperbolic points’ in the fluid flow, the extensional viscosity is large and resists the motion of the microswimmer. This increased resistance slows the worm down. As a consequence of these large extensional viscosities, we would expect to see regions with large polymeric stresses in the fluid surrounding the microswimmer. However, Lauga’s small-amplitude solution to Taylor’s waving sheet in an Oldroyd-B fluid has no such regions of large polymeric stress and still predicts the qualitative behaviour of *C. elegans*. This suggests that, at least for a small-amplitude waving sheet, there is an alternative mechanism.

In this chapter, we use our numerical solver to show that the swimming of Taylor’s waving sheet in an Oldroyd-B fluid has three regimes, depending on the amplitude of the wave. We develop a mechanistic explanation of the behaviour in these regimes.

Firstly, there is the small amplitude regime, already found by Lauga’s small amplitude calculation. We use Lauga’s solution to the problem to show that constant swimming speeds at large Deborah numbers can be understood by considering Taylor’s waving sheet as a linear oscillatory shear probe. In addition, we demonstrate that the majority of the terms in the constitutive equation for an Oldroyd-B fluid, Eq. (1.13c), do not contribute to the swimming speed of the sheet. This leads to a simple geometric explanation as to why the sheet is slowed down by viscoelasticity.

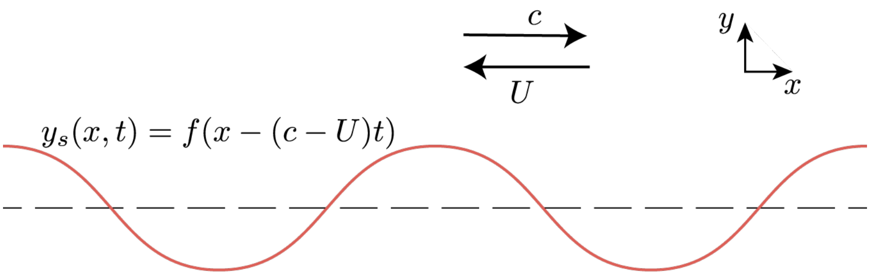

Figure 2.1 A schematic of Taylor's waving sheet in the bulk of a fluid. The sheet (red line) propagates a wave with waveform f in the positive x-direction at a speed c, which propels it in the negative x-direction at a speed U.

Secondly, there is a moderate amplitude regime with the same qualitative behaviour as the small amplitude case, but with faster relative swimming speeds. This was the behaviour found by Li and Ardekani's [23]. Using our solver, we also find the hydrodynamic field surrounding the sheet, which allows us to explain the behaviour at moderate amplitudes and small Deborah numbers in terms of the small-amplitude mechanism. We use this understanding of Taylor's sheet at moderate amplitudes to design a microswimmer that avoids, at small Deborah numbers, the slowing down caused by the viscoelasticity in the fluid at small Deborah number.

Thirdly, at large amplitudes, there is a departure from this qualitative behaviour and the swimming speed is a non-monotonic function of Deborah number. These large amplitudes are of little biological interest as the kinematics of planar wave microswimmers typically do not reach such amplitudes. While the introduction of viscoelasticity does not change the topology of the fluid flow at smaller amplitudes; at large amplitudes, the topology is different in viscoelastic fluids. We believe that this might lead to the observed non-monotonic behaviour.

We now mathematically define the problem at hand.

2.1.1 The model

In Section 1.1.3, we saw that Taylor's sheet is a model microswimmer that propagates a wave along itself in the positive x-direction such that the sheet traces out the shape y_s in the xy-plane. At a time t, this shape is given by

$$y_s(x,t) = f(k(x-(c-U)t)) \tag{2.1}$$

where U is the swimming speed of the sheet in the negative x-direction, f is the waveform, c the wave speed, and k the associated wavenumber. See Fig. 2.1.

Our goal is to find the swimming speed of the sheet in an Oldroyd-B fluid. As stated in Section 1.2.3, the hydrodynamic fields in the fluids surrounding the sheet are governed by the Stokes-Oldroyd-B equations, which are given by

$$-\nabla p + \eta_s \nabla^2 \boldsymbol{u} + \nabla \cdot \boldsymbol{\tau} = 0, \tag{2.2a}$$

$$\nabla \cdot \boldsymbol{u} = 0, \tag{2.2b}$$

$$\boldsymbol{\tau} + \lambda \overset{\triangledown}{\boldsymbol{\tau}} = 2\eta_p \mathbf{D}, \tag{2.2c}$$

where $\boldsymbol{u} = (u, v)^T$ is the velocity field, p is the pressure field, $\boldsymbol{\tau}$ is the polymeric contribution to the stress, η_s is the solvent viscosity, η_p is the polymeric viscosity and λ is the longest relaxation time in the fluid. Here

$$\overset{\triangledown}{\boldsymbol{\tau}} = \partial_t \boldsymbol{\tau} + \boldsymbol{u} \cdot \nabla \boldsymbol{\tau} - \nabla \boldsymbol{u}^T \cdot \boldsymbol{\tau} - \boldsymbol{\tau} \cdot \nabla \boldsymbol{u}$$

is the upper-convected derivative of $\boldsymbol{\tau}$. See Section 1.2.3 for more details.

In addition to these governing equations, we need boundary conditions. We use the usual no-slip boundary conditions at the sheet, which are given by

$$\boldsymbol{u}\big|_{y=y_s} = \boldsymbol{u}_s, \tag{2.3}$$

where $\boldsymbol{u}_s = (u_s, v_s)^T$ is the velocity of the material points of the sheet.

Previously, Lauga [22] has shown that, for a sine-waving sheet ($f(\zeta) = b\sin(\zeta)$), the swimming speed U is, to the lowest order in wave amplitude $\epsilon = bk$, given by

$$U = \frac{c\epsilon^2}{2}\left(\frac{1+\beta \mathrm{De}^2}{1+\mathrm{De}^2}\right), \tag{2.4}$$

where $\beta = \eta_s/(\eta_s + \eta_p)$ is the viscosity ratio and $\mathrm{De} = \lambda ck$ is the Deborah number of the problem. As the Deborah number increases, the swimming speed of the sheet decreases from the Newtonian swimming of $U_N = c\epsilon^2/2$ to a plateau value of $U_\infty = \beta U_N$ at very large Deborah number. Li and Ardekani [23] have shown that this trend continues for large amplitude sinusoidal swimmers, albeit with smaller relative decreases in swimming speed.

In Section 2.2, we begin by repeating Lauga's calculation and demonstrate that the majority of the terms in Eq. (2.2c) do not contribute to the swimming speed.

This is used in Section 2.4.1 when we discuss the small-amplitude mechanism. In Section 2.3, we outline how our numerical method can be used to solve this problem at finite amplitudes. In Section 2.4, we use the solutions found in Sections 2.2 and 2.3 to develop a mechanistic explanation for the behaviour of Taylor's sheet in an Oldroyd-B fluid. Finally in Section 2.5, we use the mechanistic understanding developed in Section 2.4 to guide us to a design of a microswimmer that avoids this mechanism at moderate amplitudes and small Deborah numbers.

2.2 Small-amplitude swimming: analytic solutions

In this section, we outline Lauga's calculation of the small-amplitude swimming speed, Eq. (2.4) for a sine-waving sheet ($f(\zeta) = b\sin(\zeta)$), and show which terms in the constitutive equation Eq. (2.2c) are responsible for the slowing down of the sheet in an Oldroyd-B fluid.

We begin by simultaneously introducing dimensionless variables and removing any explicit time dependence, by performing the following transformation to starred quantities

$$\begin{gathered} x^* = k(x-ct),\ y^* = ky,\ y_s^* = ky_s, \\ U^* = \frac{U}{c},\ u^* = 1 + \frac{u}{c},\ v^* = \frac{v}{c}, \\ p^* = \frac{p}{\eta ck},\ \boldsymbol{\tau}^* = \frac{\boldsymbol{\tau}}{\eta_p ck},\ \boldsymbol{\Sigma}^* = \frac{\boldsymbol{\Sigma}}{\eta ck}. \end{gathered}$$

In these coordinates, we are co-moving with the wave. The shape of the sheet is approximately fixed in time, such that $y_s^*(x^*) = \epsilon\sin(x^*) + \mathcal{O}(\epsilon^3)$, where $\epsilon = bk$ is the dimensionless wave amplitude. Our goal is to find the steady state velocity field surrounding the sheet and, from this, to calculate the sheet's swimming speed. From now on, we will drop the *s.

As we are only interested in the swimming speed for a small wave-amplitude sheet, we expand the fields p, $\boldsymbol{u}$ and $\boldsymbol{\tau}$ into Taylor series about $\epsilon = 0$. For example, the pressure field is given by

$$p = \sum_{n=0}^{\infty} p^{(n)} \epsilon^n. \tag{2.5}$$

where $p^{(n)}$ is the 'nth-order' contribution to the pressure field.

To find the lowest order solution to Eq. (2.2), subject to the no-slip boundary conditions of Eq. (2.3), we require the first-order velocity of the material points of the sheet. From Taylor's original paper [5], we can show that, in our frame of reference, this velocity $\boldsymbol{u}_s$ is given by

$$u_s = -1 + \mathcal{O}(\epsilon^2), \tag{2.6}$$

$$v_s = -\epsilon \cos(x) + \mathcal{O}(\epsilon^3). \tag{2.7}$$

In our coordinate system, the swimming speed of the sheet can be found by averaging the velocity field along the length of the sheet. Thus, up to the lowest (second) order in ϵ, the swimming speed of the sheet is given by

$$U = -\langle y_s \, \partial_y u^{(1)}\Big|_{y=0} \rangle \epsilon - \langle u^{(2)}\Big|_{y=0} \rangle \epsilon^2. \tag{2.8}$$

Here, the $\langle ... \rangle$ are x-averages.

We find the first and second order velocity fields by substituting the Taylor expansion of each of the fields into Eq. (2.2). We then consider each power of ϵ separately. To the zeroth order, this procedure yields the following set of equations

$$\begin{aligned} -\nabla p^{(0)} + \beta \nabla^2 \boldsymbol{u}^{(0)} + (1-\beta) \nabla \cdot \boldsymbol{\tau}^{(0)} &= \boldsymbol{0}, \\ \nabla \cdot \boldsymbol{u}^{(0)} &= 0, \\ \boldsymbol{\tau}^{(0)} &= \mathbf{D}^{(0)}, \\ \boldsymbol{u}^{(0)}\Big|_{y=0} &= -\boldsymbol{e}_x, \end{aligned}$$

which has the trivial solution $p^{(0)} = 0$, $\boldsymbol{\tau}^{(0)} = \boldsymbol{0}$, and $\boldsymbol{u}^{(0)} = -\boldsymbol{e}_x$. Note that the zeroth order velocity field does not contribute to the swimming speed of the sheet as the latter is given by the difference between the average velocities of the fluid at the sheet and at a distance far from the sheet. This difference vanishes at the zeroth order.

The first-order velocity field is the same for an Oldroyd-B fluid as for a Newtonian one [22]. To demonstrate this, consider the first order equations:

$$-\nabla p^{(1)} + \nabla \cdot (2\beta \mathbf{D}^{(1)} + (1-\beta)\boldsymbol{\tau}^{(1)}) = \mathbf{0}, \tag{2.9a}$$

$$\nabla \cdot \boldsymbol{u}^{(1)} = 0, \tag{2.9b}$$

$$(1 - \mathrm{De}\ \partial_x)\boldsymbol{\tau}^{(1)} = \mathbf{D}^{(1)}, \tag{2.9c}$$

$$\boldsymbol{u}^{(1)}\Big|_{y=0} = -\cos(x)\boldsymbol{e}_y, \tag{2.9d}$$

Here, we have used the previous solution, $u^{(0)} = -1$, in Eq. (2.9c), and we have re-arranged Eq. (2.9a) using $\nabla^2 \boldsymbol{u}^{(1)} = 2\nabla \cdot \mathbf{D}^{(1)}$.

Let $\mathcal{L}$ be the linear operator defined by

$$\mathcal{L}(\boldsymbol{a}) = (1 - \mathrm{De}\ \partial_x)\nabla \cdot \mathcal{E} \cdot \boldsymbol{a}, \tag{2.10}$$

where $\mathcal{E} = \boldsymbol{e}_x\boldsymbol{e}_y - \boldsymbol{e}_y\boldsymbol{e}_x$. Applying $\mathcal{L}$ to Eq. (2.9a), we obtain

$$\nabla \cdot \mathcal{E} \cdot \nabla \cdot \Big((1 - \mathrm{De}\ \partial_x)(2\beta \mathbf{D}^{(1)} + (1-\beta)\boldsymbol{\tau}^{(1)})\Big) = 2\nabla \cdot \mathcal{E} \cdot \nabla \cdot (1 - \beta \mathrm{De}\ \partial_x)\, \mathbf{D}^{(1)} = 0, \tag{2.11}$$

where we have used the commutativity of differential operators and Eq. (2.9c) to remove $\boldsymbol{\tau}^{(1)}$. This equation is satisfied either by a $\mathbf{D}^{(1)}$ for which $\nabla \cdot \mathcal{E} \cdot \nabla \cdot \mathbf{D}^{(1)} = 0$, or by a $\mathbf{D}^{(1)}$ for which $(1 - \beta \mathrm{De}\ \partial_x)\mathbf{D}^{(1)} = 0$. The first of these conditions is satisfied by the Newtonian solution, while the second has no non-trivial solutions that are periodic in x. Moreover, since the boundary conditions are the same as in the Newtonian case, we conclude that the first-order velocity field in an Oldroyd-B fluid is the same as its Newtonian counterpart.

From Taylor's analysis of the sheet in a Newtonian fluid [5], we know the first-order velocity field in the fluid above the sheet is given by

$$u^{(1)} = -y\sin(x)e^{-y}, \tag{2.12a}$$

$$v^{(1)} = -(1+y)\cos(x)e^{-y}. \tag{2.12b}$$

As the problem has an 'up-down' symmetry, the solution in the fluid below the sheet can be found via the transformation of $y \to -y$ and $x \to x + \pi$. The contribution of Eq. (2.12) to the swimming speed is given by the first term of Eq. (2.8), which we label U_s and reads

$$U_s = -\langle y_s\ \partial_y u^{(1)}\Big|_{y=0}\rangle \epsilon = \frac{\epsilon^2}{2}. \tag{2.13}$$

This contribution is the same as the Newtonian swimming speed. The second term in Eq. (2.8) does not contribute to the second-order swimming speed in the Newtonian case. U_s is the same regardless of whether we use the velocity field from the fluid above or below the sheet. Now we calculate the second term in Eq. (2.8) for the Oldroyd-B case.

The second-order set of governing equations is given by

$$-\nabla p^{(2)} + \beta\nabla^2\boldsymbol{u}^{(2)} + (1-\beta)\nabla\cdot\boldsymbol{\tau}^{(2)} = \boldsymbol{0}, \tag{2.14a}$$

$$\nabla\cdot\boldsymbol{u}^{(2)} = 0, \tag{2.14b}$$

$$\begin{aligned}(1-\mathrm{De}\,\partial_x)\boldsymbol{\tau}^{(2)} = \mathbf{D}^{(2)} - \mathrm{De}\Big[&\boldsymbol{u}^{(1)}\cdot\nabla\boldsymbol{\tau}^{(1)} - \\ &(\nabla\boldsymbol{u}^{(1)})^T\cdot\boldsymbol{\tau}^{(1)} - \boldsymbol{\tau}^{(1)}\cdot\nabla\boldsymbol{u}^{(1)}\Big].\end{aligned} \tag{2.14c}$$

Here, we have left out the boundary conditions, which we will consider later. As the average in the second term of Eq. (2.8) commutes with y-substitution, we only need to solve the x-average of Eq. (2.14). Specifically, we only need to find the x-average of $u^{(2)}$. Considering the x-averages of the x-component of Eq. (2.14a) and the xy-component of Eq. (2.14c), we have

$$\beta\partial_{yy}\langle u^{(2)}\rangle + (1-\beta)\partial_y\langle\tau_{xy}^{(2)}\rangle = 0, \tag{2.15a}$$

$$\begin{aligned}\langle\tau_{xy}^{(2)}\rangle = \partial_y\langle u^{(2)}\rangle - \mathrm{De}\Big[&\langle u^{(1)}\partial_x\tau_{xy}^{(1)}\rangle + \langle v^{(1)}\partial_y\tau_{xy}^{(1)}\rangle - \\ &\langle D_{xy}^{(1)}(\tau_{xx}^{(1)}+\tau_{yy}^{(1)})\rangle + \langle\Omega_{xy}^{(1)}(\tau_{xx}^{(1)}-\tau_{yy}^{(1)})\rangle\Big],\end{aligned} \tag{2.15b}$$

where $\boldsymbol{\Omega} = (\nabla\boldsymbol{u}^T - \nabla\boldsymbol{u})/2$ is the vorticity tensor, and we have ignored the x-averages of x-derivatives of x-periodic functions, which must vanish. Since the first order fields are known, Eq. (2.15) is simply an ordinary differential equation for $\langle u^{(2)}\rangle$, the solution to which is given by

$$\langle u^{(2)}\rangle = E + Fy + \frac{(1-\beta)\mathrm{De}^2}{2(1+\mathrm{De}^2)}(1-2y^2)e^{-2y}, \tag{2.16a}$$

$$\text{with } \langle\tau_{xy}^{(2)}\rangle = F - \frac{\mathrm{De}^2}{1+\mathrm{De}^2}(1+2y-2y^2)e^{-2y}. \tag{2.16b}$$

Here, E and F are arbitrary constants, which we find by applying the appropriate boundary conditions. Firstly, we require that the $\langle u^{(2)}\rangle$ does not contribute to the velocity field far from the sheet. Secondly, we require that the sheet is force-free in the x-direction. The first-order flow field, which is the same as the first-order Newtonian flow field, does not apply a net-force to the sheet [76]. The second order flow field contributes a force per unit area of $\boldsymbol{\Sigma}^{(2)} \cdot \boldsymbol{n}\Big|_{y=0}$ where $\boldsymbol{n}$ is the inward-normal of the sheet. To the second order, these boundary conditions are given by

$$\lim_{y\to\infty} \langle u^{(2)} \rangle = 0, \tag{2.17a}$$

$$-\beta \partial_y \langle u^{(2)} \rangle\Big|_{y=0} + (1-\beta)\langle \tau_{xy}^{(2)} \rangle\Big|_{y=0} = 0. \tag{2.17b}$$

which has the trivial solution of $E = F = 0$. Evaluating Eq. (2.16a) at $y = 0$ yields the second term of Eq. (2.8), which we label U_p and reads

$$U_p = -\left. \langle u^{(2)} \rangle \right|_{y=0} = \frac{(1-\beta)\mathrm{De}^2}{2(1+\mathrm{De}^2)}. \tag{2.18}$$

Combined with U_s in Eq. (2.13), this gives the second order swimming speed in Eq. (2.4).

Let us observe that the majority of the terms in Eq. (2.15b) do not contribute to the swimming speed of the sheet. Consider the following set of equations as a replacement for Eq. (2.15)

$$\beta \partial_{yy} \langle u^{(2)} \rangle + (1-\beta)\partial_y \langle \tau_{xy}^{(2)} \rangle = 0, \tag{2.19a}$$

$$\langle \tau_{xy}^{(2)} \rangle = \partial_y \langle u^{(2)} \rangle - \mathrm{De}\langle \Omega_{xy}^{(1)} (\tau_{xx}^{(1)} - \tau_{yy}^{(1)}) \rangle. \tag{2.19b}$$

As before, the first-order fields are known and Eq. (2.19) is again an ordinary differential equation of $\langle u^{(2)} \rangle$. Now, the solution is given by

$$\langle u^{(2)} \rangle = E + Fy + \frac{(1-\beta)\mathrm{De}^2}{2(1+\mathrm{De}^2)}(1+2y)e^{-2y}, \tag{2.20}$$

which is governed by the same boundary conditions as before, leading to $E = F = 0$. Evaluating $\langle u^{(2)} \rangle$ at $y = 0$ for the reduced set of second-order equation yields U_p, which is still given by Eq. (2.18). Thus, the set of equations in Eq. (2.19) is sufficient to predict the swimming speed of the sheet in Oldroyd-B fluids at small wave amplitudes. And, importantly, all the physics that is responsible for the slowing down compared to swimming in a Newtonian fluid is contained in Eq. (2.19).

In Section 2.4.1, we use Eq. (2.19) to guide a geometrical argument as to why the sheet is slowed down by viscoelasticity. However, before this, we describe how we solve the problem numerically for a finite-amplitude swimmer.

2.3 Finite-amplitude swimming: numerical solutions

In the previous section, our analysis is only valid for small wave amplitudes. In order to investigate the behaviour of the sheet at finite wave amplitudes, we use a numerical solver based on spectral methods. Similarly to the small-amplitude analysis, we find the velocity field surrounding the sheet; and from this calculate the swimming speed. To do so, we still solve Eq. (2.2), subject to the boundary conditions Eq. (2.3).

Rather than solving the problem in an unbounded domain, we solve the problem of a sheet surrounded by walls at a distance h_+ and h_- above and below the centreline of the sheet, respectively. This introduces a new set of boundary conditions: that there is no slip at the wall, which is given by

$$\boldsymbol{u}\big|_{y=\pm h_\pm} = \boldsymbol{u}_w \tag{2.21}$$

where $\boldsymbol{u}_w = (u_w, v_w)^T$ is the velocity of the material points of the wall. We are only interested in up-down-symmetric waveforms, so we set $h_+ = h_- = h$, resulting in the equivalence of the fluid domains above and below the sheet. From now on, we will only consider the fluid domain above the sheet. We select $hk = 13.0$ throughout this thesis, as we find this is sufficiently large that doubling hk does not change the converged swimming speed by more than 0.5%.

To begin, we perform a similar transformation to starred quantities to remove any explicit time dependence and render the variables dimensionless:

$$\begin{gathered} x^* = k(x-(c-U)t),\ y^* = ky,\ y_s^* = ky_s,\ f^* = kf,\ h^* = kh, \\ U^* = \frac{U}{c},\ u^* = 1 - \frac{U}{c} + \frac{u}{c},\ v^* = \frac{v}{c}, \\ p^* = \frac{p}{\eta ck},\ \boldsymbol{\Sigma}^* = \frac{\boldsymbol{\Sigma}}{\eta ck},\ \boldsymbol{\tau}^* = \frac{\boldsymbol{\tau}}{\eta_p ck}. \end{gathered}$$

This frame is exactly co-moving with the wave; whereas the small-amplitude frame was only co-moving with the wave to the lowest order in wave amplitude. In this frame, the velocity of the material points of the wall is given by $\boldsymbol{u}_w^* = -(1-U^*)\boldsymbol{e}_x$ and the shape of the sheet is fixed in time such that $y_s^*(x^*) = f^*(x^*)$. From now on, we will drop the *s for clarity.

As originally found by Taylor [5], the velocity of the material points of the sheet in this frame of reference is given by

$$u_s(x) = -\frac{Q}{\sqrt{1+f'(x)^2}}, \tag{2.22a}$$

$$v_s(x) = -\frac{Qf'(x)}{\sqrt{1+f'(x)^2}}, \tag{2.22b}$$

$$\tag{2.22c}$$

where

$$Q = \int_0^{2\pi} \sqrt{1+f'(x)^2}\mathrm{d}x.$$

We introduce a stream-function $\psi(x,y)$ to exploit the two-dimensional nature of the problem. The stream-function is defined such that it automatically solves Eq. (2.2b) for any choice of ψ. This is achieved by setting $u = \partial_y\psi$ and $v = -\partial_x\psi$. The remaining equations to solve are the curl and divergence of Eq. (2.2a), along with the constitutive Eq. (2.2c), resulting in the following

$$\beta\nabla^4\psi - (1-\beta)\Big[\Box^2\tau_{xy} - \partial_{xy}(\tau_{xx} - \tau_{yy})\Big] = 0, \tag{2.23a}$$

$$\nabla^2 p - (1-\beta)\Big[\partial_{xx}\tau_{xx} + 2\partial_{xy}\tau_{xy} + \partial_{yy}\tau_{yy}\Big] = 0, \tag{2.23b}$$

$$\tau_{xx} - 2\partial_{xy}\psi + \mathrm{De}\Big[(\partial_y\psi\partial_x - \partial_x\psi\partial_y)\tau_{xx} - 2\tau_{xx}\partial_{xy}\psi - 2\tau_{xy}\partial_{yy}\psi\Big] = 0, \tag{2.23c}$$

$$\tau_{xy} + \Box^2\psi + \mathrm{De}\Big[(\partial_y\psi\partial_x - \partial_x\psi\partial_y)\tau_{xy} + \tau_{xx}\partial_{xx}\psi - \tau_{yy}\partial_{yy}\psi\Big] = 0, \tag{2.23d}$$

$$\tau_{yy} + 2\partial_{xy}\psi + \mathrm{De}\Big[(\partial_y\psi\partial_x - \partial_x\psi\partial_y)\tau_{yy} + 2\tau_{xy}\partial_{xx}\psi + 2\tau_{yy}\partial_{xy}\psi\Big] = 0, \tag{2.23e}$$

where $\Box^2 = \partial_{xx} - \partial_{yy}$. There are five differential equations, three of which are non-linear, with five fields to solve for (ψ, p, τ_{xx}, τ_{xy}, τ_{yy}).

We solve Eq. (2.23) numerically, using a spectral method adapted for the geometry of our problem, where the hydrodynamic fields are represented by Fourier-Chebyshev series [77]. Since the convergence properties of the Fourier-Chebyshev basis are optimal in rectangular domains, we perform a coordinate transformation, which projects the domain onto a rectangular strip, which is periodic in one direction. This transformation from the (x,y)-coordinates into

(η, ξ)-coordinates is given by

$$\eta = x, \tag{2.24a}$$

$$\xi = 1 - 2\frac{h-y}{h-f(x)}. \tag{2.24b}$$

Here, $\xi = 1$ corresponds to the domain's wall; whereas $\xi = -1$ corresponds to the sheet.

In this deformed domain, we represent the hydrodynamic fields by truncated Fourier-Chebyshev series. For example, the pressure field, p, is given by

$$p(\eta, \xi) = \sum_{n=0}^{N-1} \sum_{m=0}^{M-1} p^{(nm)} F_n(\eta) T_m(\xi), \tag{2.25}$$

where $T_m(\xi) = \cos(m \arccos(\xi))$ is the mth Chebyshev polynomial, and

$$F_n(\eta) = \begin{cases} \sin(\frac{n+1}{2}\eta) & n \text{ odd} \\ \cos(\frac{n}{2}\eta) & n \text{ even}, \end{cases}$$

is the nth Fourier mode. We increase the resolution (N, M) until the error in the calculated swimming speed is no more than 0.5%. We find a resolution of $N = 25$ and $M = 60$ is typical for a sine-waving sheet with amplitude around $bk = 1.0$ in the bulk of an Oldroyd-B fluid.

The spatial derivatives ∂_η and ∂_ξ of the Fourier-Chebyshev representations are calculated by multiplying vectors containing the spectral coefficients with the $NM \times NM$ spectral derivative matrices [77–79]. The spatial derivatives in the original (x, y)-space are then trivially constructed with the help of Eq. (2.24), giving

$$\frac{\partial}{\partial x} = \frac{\partial}{\partial \eta} + (\xi - 1)\frac{f'(\eta)}{h - f(\eta)}\frac{\partial}{\partial \xi}, \tag{2.26a}$$

$$\frac{\partial}{\partial y} = \frac{2}{h - f(\eta)}\frac{\partial}{\partial \xi}. \tag{2.26b}$$

We use a Fast-Fourier transform technique to calculate products of fields, using the collocation points given by

$$\eta_{n_c} = \frac{2\pi n_c}{N_c}, \tag{2.27a}$$

$$\xi_{m_c} = \cos\left(\frac{\pi m_c}{M_c - 1}\right). \tag{2.27b}$$

Here, $n_c \in [0, N_c)$, $m_c \in [0, M_c)$, and the collocation resolution (N_c, M_c) is selected to satisfy $N_c > 1.5N$ and $M_c > 1.5M$ in order to avoid aliasing issues [77, 78].

Representing five governing equations in the truncated Fourier-Chebyshev basis yields a set of $5NM$ non-linear algebraic equations, which need to be complemented by the boundary conditions. By using Fourier modes, we have implicitly imposed periodic boundary conditions in the η-direction. This correctly reflects the symmetry of the underlying problem. In finding the steady state solution, we have also applied the only boundary condition required to determine $\boldsymbol{\tau}$. However, we still need six boundary conditions (four for ψ and two for p) along the lines $\xi = \pm 1$. These boundary conditions are expanded in the Fourier basis (as they are functions of η), generating $6N$ discretised boundary conditions to substitute into the original set of $5NM$ discretised governing equations.

The first boundary conditions to consider are the no-slip boundary conditions at both the sheet and the wall in Eqs. (2.3) and (2.21), where the velocities of the material points of the sheet are given by Eq. (2.22) and $\boldsymbol{u}_w = (U-1)\boldsymbol{e}_x$. The four boundary conditions are, therefore,

$$\partial_y \psi|_{\xi=-1} = u_s, \tag{2.28a}$$

$$-\partial_x \psi|_{\xi=-1} = v_s, \tag{2.28b}$$

$$\partial_y \psi|_{\xi=1} = u_w = U - 1, \tag{2.28c}$$

$$-\partial_x \psi|_{\xi=1} = v_w = 0. \tag{2.28d}$$

Note that the x-derivative of the $n = 0$ Fourier mode vanishes, and that the sheet's swimming speed U, which is unknown, appears in the $n = 0$ mode of Eq. (2.28), thus different sets of boundary conditions are required for the $n = 0$ and the $n \neq 0$ Fourier modes. We address this below. Before coming to this, we consider the other two boundary conditions required for the $n \neq 0$ case.

As already mentioned above, we do not directly solve the force balance equation, Eq. (2.2a), but instead solve its derivatives (specifically its curl and divergence, see Eq. (2.23)). The solutions to both problems may differ, at most, by curl-free and divergence-free terms. To fix those terms, we explicitly ensure that the force balance equation is satisfied at the boundaries. Specifically, at both the sheet and the wall, we require that the $\boldsymbol{n} \cdot \nabla \cdot \boldsymbol{\Sigma} = 0$, where $\boldsymbol{n}$ is the normal to the surface. This yields the final two boundary conditions for the $n \neq 0$ Fourier modes:

$$\begin{gathered}\Big[f'(\eta)\partial_x p - \partial_y p + \beta(f'(\eta)\partial_y - \partial_x)\nabla^2\psi + \\ f'(\eta)\partial_x\tau_{xx} + (f'(\eta)\partial_y + \partial_x)\tau_{xy} + \partial_y\tau_{yy}\Big]_{\xi=-1} = 0,\end{gathered} \tag{2.29a}$$

$$\Big[\partial_y p + \beta\partial_x\nabla^2\psi - \partial_x\tau_{xy} - \partial_y\tau_{yy}\Big]_{\xi=1} = 0, \tag{2.29b}$$

where we have used $(0,-1)^T$ as the normal to the wall, and $(-f'(\eta),1)^T$ as the normal to the surface of the sheet.

For the $n = 0$ mode, we replace Eqs. (2.28a), (2.28b), (2.28d) and (2.29b) with alternative boundary conditions. First of all, we note that ψ and p are defined up to a constant as only their derivatives are physical. We set those constants to some arbitrary value. The other two boundary conditions ensure that the average x-forces being applied to the wall and the sheet are both zero. Thus, we have

$$p|_{\xi=1} = 0, \tag{2.30a}$$

$$\psi|_{\xi=1} = 0, \tag{2.30b}$$

$$\Big[\beta\Box^2\psi - \tau_{xy}\Big]_{\xi=1} = 0, \tag{2.30c}$$

$$\Big[f'(\eta)p_+ - 2\beta f'(\eta)\partial_{xy}\psi - \beta\Box^2\psi - f'(\eta)\tau_{xx} + \tau_{xy}\Big]_{\xi=-1} = 0, \tag{2.30d}$$

In the spirit of the Chebyshev-tau method [78], for each Fourier mode we replace the four highest Chebyshev modes of the discretised Eq. (2.23a) and the two highest modes of Eq. (2.23b) with the boundary conditions. Combining everything together yields of a set of $5NM$ non-linear discretised equation. The structure of these equations is summarised in Table 2.1.

The set of equations is, in general, non-linear. To solve the equations, we use the Newton-Raphson method [78] with an analytically calculated Jacobian. In general, for De > 0, starting from an arbitrary initial guess does not lead to convergence of the Newton-Raphson algorithm, and therefore, we employ a simple continuation strategy. For each set of parameters, we start from the Newtonian case, De $= 0$, which is linear and can always be solved, and use its solution as the initial guess for a slightly higher De. This process is continued until we either reach the target value of De or the algorithm fails to converge, in which case a smaller step ΔDe is selected. In practice, the ΔDe required for continuation

	$n = 0$	$0 < n < N$
$0 \leq m < M - 4$	Equations (2.23a) to (2.23e)	Equations (2.23a) to (2.23e)
$m = M - 4$	Equation (2.30d) Equations (2.23b) to (2.23e)	Equation (2.28d) Equations (2.23b) to (2.23e)
$m = M - 3$	Equation (2.30c) Equations (2.23b) to (2.23e)	Equation (2.28c) Equations (2.23b) to (2.23e)
$m = M - 2$	Equation (2.30b) Equation (2.30a) Equations (2.23c) to (2.23e)	Equation (2.28b) Equation (2.29b) Equations (2.23c) to (2.23e)
$m = M - 1$	Equation (2.28a) Equation (2.29a) Equations (2.23c) to (2.23e)	Equation (2.28a) Equation (2.29a) Equations (2.23c) to (2.23e)

Table 2.1 An outline of how the $5NM$ discretised equations are constructed from the differential equations in Eq. (2.23) and the various boundary conditions Eqs. (2.28) to (2.30).

becomes very small at sufficiently large De, leading to unreasonable computation times. In this case, we only report the results up to that value of De.

2.3.1 Results

Figure 2.2 shows the swimming speed U, scaled by the Newtonian swimming speed U_N, of a sine-waving sheet ($f(\zeta) = b\sin(\zeta)$) against Deborah number De at different wave amplitudes b and viscosities ratios β. There are three regimes for the behaviour of the scaled swimming speed U/U_N as a function of Deborah number.

At small wave amplitudes ($bk = 0.1$), we find that the numerically calculated swimming speeds (symbols) agree with the small amplitude calculation (lines) originally found by Lauga [22].

At moderate wave amplitudes, we find the same behaviour as that observed by Li and Ardekani [23]. The scaled swimming speed has qualitatively similar behaviour to the small-amplitude regime. It decreases monotonically with increasing Deborah number, reaching a constant swimming speed at large Deborah numbers. However, at a given Deborah number, U/U_N is greater than that predicted by the small-amplitude calculation.

At large amplitudes ($bk = 2.0$ and $bk = 2.5$), we find that the swimming speed is no longer a monotonically decreasing function of Deborah number and that,

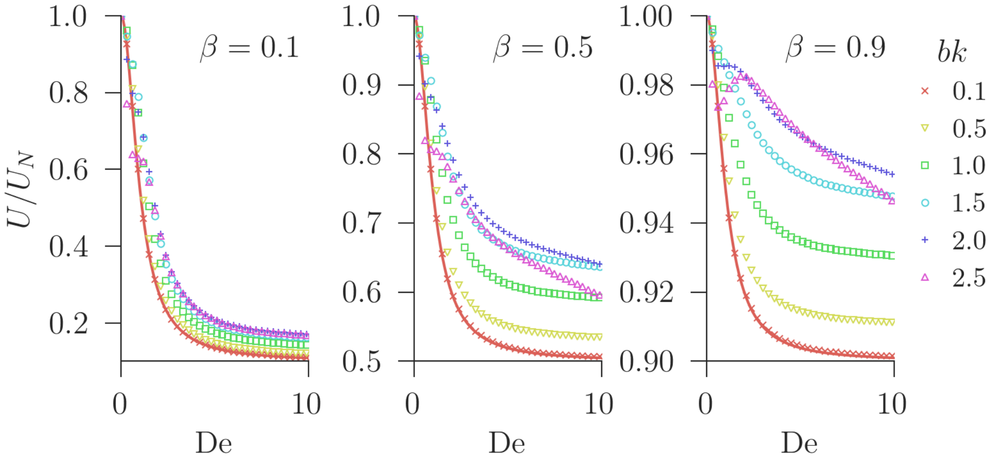

Figure 2.2 Swimming speed U, scaled by the Newtonain swimming speed U_N, against Deborah number De for a sine-waving sheet ($f(\zeta) = b\sin(\zeta)$) in Oldroyd-B fluids for different viscosity ratios β and wave amplitudes b. The numerical results (symbols) are obtained by solving the equations in Table 2.1, using the method described in the text. The small-amplitude swimming speeds (lines) show good agreement with the $bk = 0.1$ numerical results. The Newtonian swimming speeds are $U_N/c = 4.941 \times 10^{-3}$, 9.578×10^{-2}, 0.2159, 0.2632, 0.2703 and 0.2649 for $bk = 0.1$, 0.5, 1.0, 1.5, 2.0 and 2.5, respectively.

at least by De $=$ 10, plateau values are not reached. Interestingly, the non-monotonicity seems to be strongest for dilute (large β) solutions. As previously mentioned, large amplitude behaviour is not of much biological interest. Real microswimmers rarely reach such large amplitudes. For example, some of the largest amplitude swimmers, sea-urchin spermatozoa, have a wave amplitude of $bk \approx 1.5$ [41], which is in the moderate-amplitude regime.

We will now seek to explain these results mechanistically.

2.4 Discussion

In Sections 2.2 and 2.3, we found the swimming speed of and the hydrodynamic fields surrounding Taylor's sheet in an Oldroyd-B fluid. Here, we will use this to discuss the mechanism responsible for the behaviour observed, excluding the large-amplitude regime due to its lesser relevance.

In Section 2.4.1, we discuss the mechanism at small amplitudes, followed by a discussion of the mechanism at moderate amplitudes in Section 2.4.2. Finally, we compare our solution of Taylor's sheet in an Oldroyd-B fluid to the flow field around *C. elegans*, observed by Shen and Arratia [20] in Section 2.4.3.

2.4.1 The small-amplitude mechanism

To understand why there is a constant swimming speed at large Deborah numbers, consider the small-amplitude waving sheet as an oscillatory shear probe. By virtue of being at small amplitudes, the sheet is probing the linear viscoelastic regime of the fluid, as defined by Eq. (1.10).

Recall that the first-order velocity field surrounding the sheet in an Oldroyd-B fluid is the same as it would be in a Newtonian fluid. Also recall, from Section 1.1.3, that this velocity field consists of a periodic array of counter-rotating vortices. At all points, excluding lines directly between the vortices and the centreline of the vortices, the velocity field associated with these vortices is a local shear flow. The locations of the vortices are tied to the shape of the sheet. Thus, as the wave passes along the length of the sheet, the vortices are dragged with it and as such, each point in the fluid is experiencing an oscillatory shear flow.

To understand the swimmer as an oscillatory shear probe, we look at the shear stress and strain rate. However, these are not just the xy-components of the corresponding tensors as they would be for a simple oscillatory shear probe. This is because the xy-axis is defined in relationship to the sheet, not to the local shear at any given point. To find the shear rate and stress for our oscillatory shear probe, we would have to transform the corresponding tensors from the xy-basis to some local basis, aligned with the shear at each point in the fluid. Rather than performing these local transformations, we will simply look at all of components of the strain rate and stress tensors as, in general, they all contribute to the shear strain rate and stress.

The non-zero components of the first-order strain rate tensor and vorticity tensor (which we will need later) are given by

$$D_{xx}^{(1)} = -D_{yy}^{(1)} = -y\cos(x)e^{-y}, \tag{2.31a}$$

$$D_{xy}^{(1)} = y\sin(x)e^{-y}, \tag{2.31b}$$

$$\Omega_{xy}^{(1)} = -\sin(x)e^{-y}. \tag{2.31c}$$

The components of the first-order polymeric stress tensor are given by

$$\tau_{xx}^{(1)} = -\tau_{yy}^{(1)} = 2e^{-y}y\frac{\mathrm{De}\sin(x) - \cos(x)}{1+\mathrm{De}^2}, \tag{2.32a}$$

$$\tau_{xy}^{(1)} = 2e^{-y}y\frac{\sin(x) + \mathrm{De}\cos(x)}{1+\mathrm{De}^2}. \tag{2.32b}$$

Notice the similarity between this and the linear oscillatory shear response of an Oldroyd-B fluid, see Eqs. (1.10) and (1.14). Each component of the polymeric stress has two components, one in-phase with the corresponding strain rate and another out-of-phase. The in-phase component corresponds to the viscous response of the viscoelastic agents in the fluid, that is η' in Eq. (1.10). Whereas, the out-of-phase component corresponds to the elastic response of the viscoelastic agent, that is η'' in Eq. (1.10). The viscous response is the response to the instantaneous flow field and the elastic response corresponds to the viscoelastic agents' 'memory' of the flow field they experienced at previous times. As is clear when considering the averages in Eq. (2.15b), it is only the out-of-phase, or memory, components that contribute to the swimming speed.

This provides a simple mechanistic explanation for the constant swimming speed at large Deborah numbers. At large Deborah numbers, the viscoelastic agents do not have time to react to the oscillating shear flow created by the waving sheet. As such, they provide no contribution to the viscous response of the fluid and the response is purely elastic. In this regime, the elastic response is characterised by the storage modulus $G' = \eta''\omega$, which is constant [68]. In the large Deborah number limit, the storage modulus corresponding to an oscillatory shear strain is constant. Therefore, the elastic response of the polymers is independent of the Deborah number. This is the origin of the constant swimming speed at large Deborah numbers.

We have now established an explanation for the existence of the plateau swimming speed. Yet, why is this plateau swimming speed slower than the swimming speed of the same swimmer in a Newtonian fluid? To answer this question, recall from Section 2.2 that Eq. (2.19) is sufficient to predict the small-amplitude swimming speed. We can understand why the sheet slows down in a viscoelastic fluid by considering the $\langle \Omega_{xy}^{(1)}(\tau_{xx}^{(1)} - \tau_{yy}^{(1)})\rangle$ term in Eq. (2.19b). By analysing this term, we show that the sheet slows down, due to the geometry of the vortex array.

Figure 2.3 shows a schematic of the physical mechanism responsible for the slowing down of Taylor's sheet in the upper Oldroyd-B fluid. The schematic

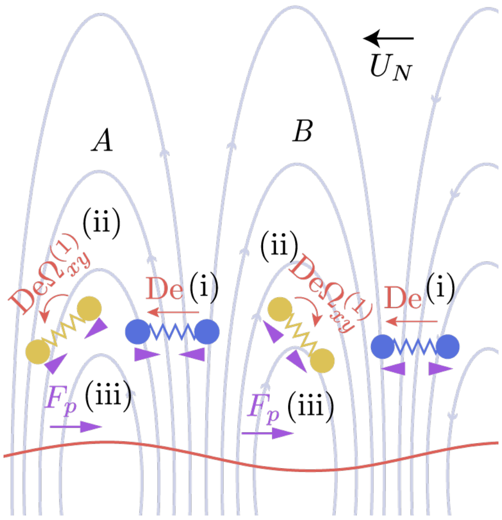

Figure 2.3 A schematic of the physical mechanism responsible for the slow down of Taylor's sheet in an Oldroyd-B fluid. This image is in the frame of reference where the wave is stationary, thus the fluid is drifting to the left at a speed c. The streamlines of the vortex array around the sheet are shown in grey. The blue dumbbells represent the xx-component of the first-order elastic response to the local oscillatory shear flow. The yellow dumbbells represent the elastic response after it has been rotated by the vortices. See the text for more details.

is drawn in a frame of reference that follows the wave. In this frame, the fluid drifts to the left at a speed c. As in Section 1.1.3, the motion of the material points of the sheet creates a vortex array, which pushes the sheet to the left at a speed U_N. The sheet is slowed by a three step process shown in Fig. 2.3. These steps are not sequential; but aid in understanding the process. Step (i), there is a first-order elastic response (blue dumbbells) to the local oscillatory strain rate, $D^{(1)}_{xx}$, created as the fluid drifts past the sheet. This is the out-of-phase component of $\tau^{(1)}_{xx}$ and can be understood as viscoelastic agents (dumbbells) oriented in the x-direction being stretched in the x-direction. Step (ii), this first-order elastic response is rotated by the vortices creating the second-order polymeric stress $\tau^{(2)}_{xy}$ (yellow dumbbells). Step (iii), this second-order polymeric stress pushes on the sheet with a polymeric force F_p as the viscoelastic agents relax.

This three-step process occurs in both the anticlockwise-rotating vortices, such as A, and the clockwise-rotating vortices, such as B. The strain rate $D^{(1)}_{xx}$ created by the vortices is arranged relative to the vorticity $\Omega^{(1)}_{xy}$, such that the polymeric stresses in both A and B push the sheet in the same direction, as illustrated in Fig. 2.3. Viscoelastic agents in vortex A 'remember' recently travelling through a region of positive $D^{(1)}_{xx}$. As the anticlockwise-rotating vortex has a negative vorticity $\Omega^{(1)}_{xy}$, this leads to a negative $\tau^{(2)}_{xy}$. Conversely, viscoelastic agents in vortex B remember travelling through a region of negative $D^{(1)}_{xx}$. The clockwise-rotating vortex has a positive vorticity $\Omega^{(1)}_{xy}$, so once more we have a negative $\tau^{(2)}_{xy}$. This leads to a net polymeric force pushing the sheet to the right, the same direction as the wave. In order to be force-free, the sheet must swim more quickly to the right. As U_N is to the left, this results in slowing the sheet down.

We can summarise the small-amplitude mechanism as follows. When the wave passes down the sheet, the vortex array is dragged along with it. At a given point in the fluid, the passing vortex array creates a local oscillatory shear. There is a linear viscoelastic response to this oscillatory shear. The out-of-phase elastic part of this linear viscoelastic response interacts with the vortex array, creating a net push on the sheet. The direction of the wave breaks the symmetry of the vortices, resulting in a net push on the sheet by the viscoelastic agents. Due to the geometry of the vortex array, the resulting net push is in the same direction as the wave. As the vortices themselves push the sheet in the opposite direction to the wave, this elastic mechanism results in a slowing down of the sheet.

This mechanism explains why the sheet slows down and why there is a plateau at large Deborah numbers, in the small-amplitude regime. Now, we consider the moderate-amplitude case and show that the small-amplitude mechanism is still dominant at moderate amplitudes and small Deborah numbers.

2.4.2 The moderate-amplitude mechanism

Figure 2.2 shows that at moderate wave amplitudes, the scaled swimming speed U/U_N of the sheet behaves in a similar manner as it is does at small wave amplitudes. The scaled swimming speed decreases monotonically, reaching a plateau value at large Deborah numbers. At all Deborah numbers, this scaled swimming speed is faster than that predicted by the small-amplitude calculation. In this subsection, we attempt to understand this change in behaviour at moderate amplitudes.

At moderate wave amplitudes, there are higher frequency responses to the local oscillatory shear flow created by the passing vortex array. These are the typical non-linear viscoelastic responses found in simple large amplitude oscillatory shear experiments [80]. These non-linear responses depend on the Deborah number to a higher order than the linear response. As such, these non-linear responses can be neglected at small Deborah numbers. This is corroborated by Fig. 2.4.

Figure 2.4 shows the numerically-calculated hydrodynamic fields surrounding the sine-waving sheet with amplitudes $bk = 0.01$ and $bk = 0.5$ at $\beta = 0.5$ and $\mathrm{De} = 0.0$, 1.0 and 10. In each figure we plot the components of the polymeric stress that were relevant in the small-amplitude case: τ_{xy} and $(\tau_{xx} - \tau_{yy})$ and the flow-type

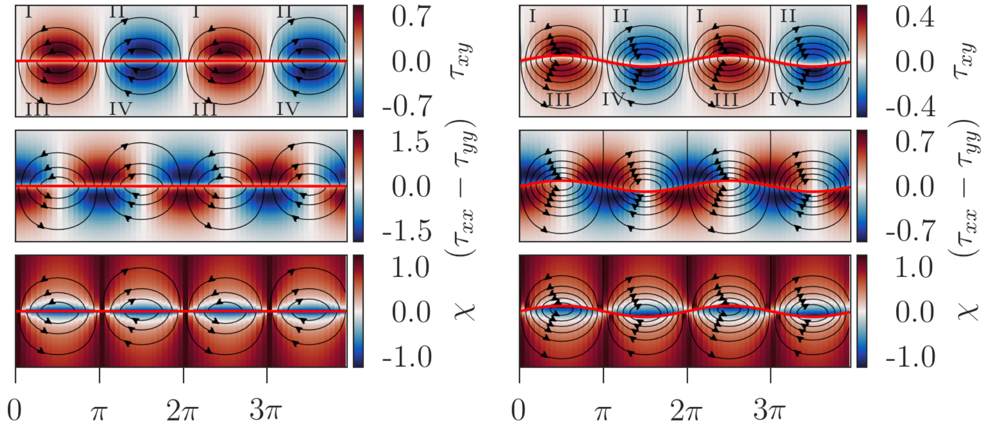

(a) $bk = 0.01$ and $\mathrm{De} = 0.0$. $U = U_N = 5.00 \times 10^{-5}\ c$.

(b) $bk = 0.5$ and $\mathrm{De} = 0.0$. $U = U_N = 9.58 \times 10^{-2}\ c$.

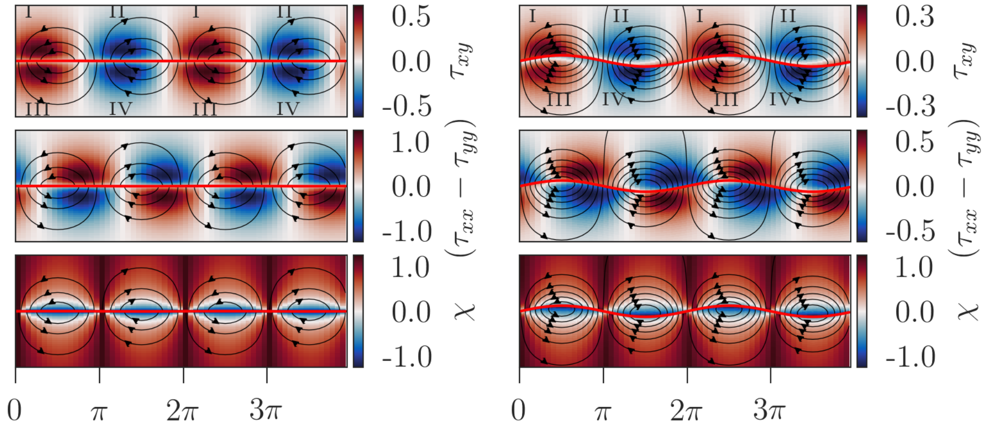

(c) $bk = 0.01$ and $\mathrm{De} = 1.0$. $U = 0.750U_N$.

(d) $bk = 0.5$ and $\mathrm{De} = 1.0$. $U = 0.791U_N$.

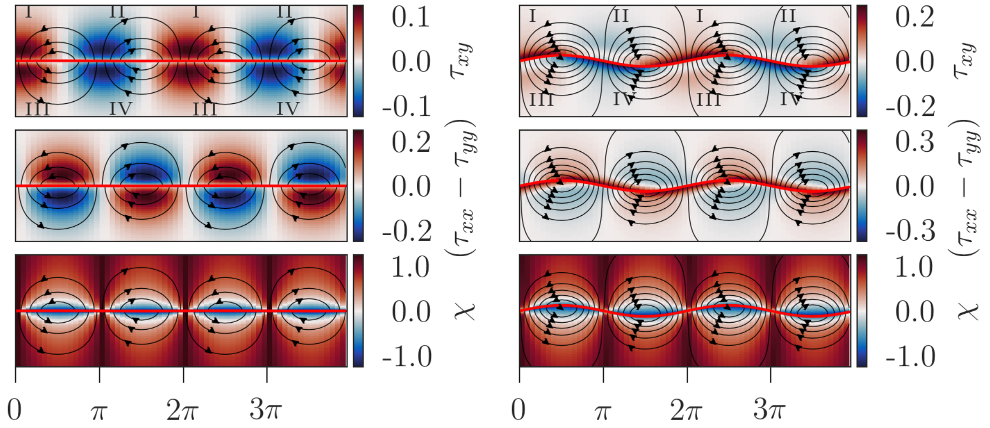

(e) $bk = 0.01$ and $\mathrm{De} = 10.0$. $U = 0.505U_N$.

(f) $bk = 0.5$ and $\mathrm{De} = 10.0$. $U = 0.535U_N$.

Figure 2.4 The polymeric stress tensor $\boldsymbol{\tau}$ and flow parameter χ surrounding a sine-waving sheet with amplitude $bk = 0.01$ and $bk = 0.5$ and $\mathrm{De} = 0.0$, 1.0 and 10.0. In all cases $\beta = 0.5$ and $-5 \leq yk \leq 5$. The stress tensor components are in units of $100\eta_p kc$ and $\eta_p kc$ for the $bk = 0.01$ and $bk = 0.5$ cases, respectively.

parameter χ [81]. The flow-type parameter is defined as

$$\chi = \frac{|\mathbf{D}| - |\mathbf{\Omega}|}{|\mathbf{D}| + |\mathbf{\Omega}|}. \tag{2.33}$$

Based on the invariants of the velocity gradient tensor, χ is designed to determine the type of flow at every point in space, independent of local orientation: $\chi = 1$ corresponds to purely extensional flow, $\chi = 0$ – to shear, and $\chi = -1$ – to purely rotational flows. Note that the flow type parameter does not measure the magnitude of the flow, only its topology. Superimposed over these fields are the streamlines for the flow with occasional arrows showing the direction of the flow.

The $bk = 0.01$ plots show good agreement with two predictions made by the small amplitude analysis: (i) The topology of the flow field is unaffected by the Deborah number at small wave amplitudes; and (ii) the polymeric stress drifts downstream as the Deborah number increases because the out-of-phase components begin to dominate. For $bk = 0.5$, we find that prediction (i) is still valid: the topology of the flow does not change much as the Deborah number increases. However, the validity of prediction (ii) depends on Deborah number. At $\mathrm{De} = 1.0$, the polymeric stress approximately drifts downstream as in the small-amplitude case. However, at large Deborah numbers the polymeric stress is very different from the small-amplitude prediction. At $\mathrm{De} = 10.0$, the polymeric stress has clustered around the sheet, decaying very quickly as we move into the rest of the fluid. This suggests that the non-linear viscoelastic responses to the oscillatory shear can indeed be neglected at small Deborah numbers. However, they become relevant at larger Deborah numbers.

At small Deborah numbers and moderate wave amplitudes, the constituents of the small-amplitude mechanism are still dominant. Thus, we expect this mechanism to still apply. The slowing down is still due to the interactions of the linear viscoelastic response to the local oscillatory shear with the vortex arrays. However, the relative decrease in swimming speed at moderate wave amplitudes is weaker than at small wave amplitudes. We can understand this by considering the shape of the sheet, i.e. its position in the flow field. It is clear from Fig. 2.4 that the key difference between the small and moderate amplitude cases is the proximity of the sheet to the different regions of the flow field. We believe this is why the scaled swimming speeds are greater at moderate wave amplitudes and small Deborah numbers.

To understand this further, we must consider the polymeric 'shear' stress τ_{xy} in

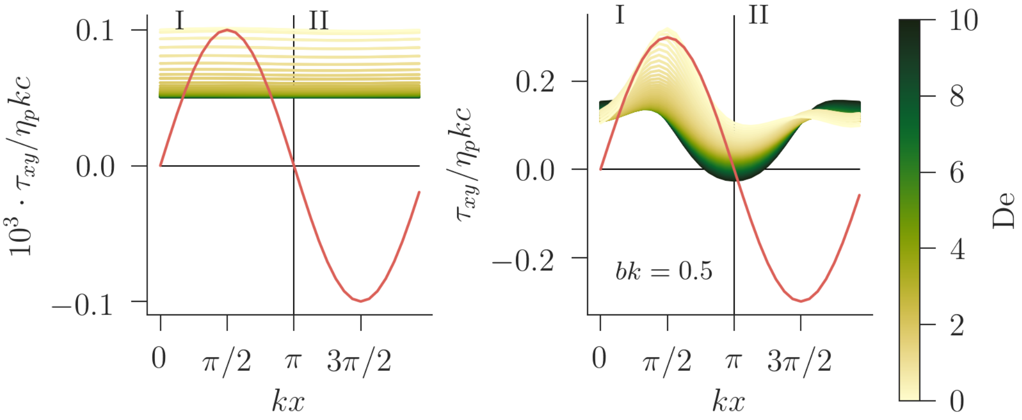

Figure 2.5 The polymeric shear stress in the upper fluid evaluated along the length of a sine-waving sheet, with amplitudes $bk = 0.01$ (left) and $bk = 0.5$ (right) at various Deborah numbers. In both cases, the viscosity ratio is $\beta = 0.5$. At small-amplitudes, the shear stress changes with Deborah number evenly along the length of the sheet; whereas at moderate amplitudes, the effect is much more pronounced in region I than region II.

more detail. We have identified changes in the polymeric shear stress as being responsible for slowing the sheet down. Positive shear stress above the sheet and negative shear stress below the sheet both push it in the negative x-direction, which is the direction of swimming in our plots. As the Deborah number increases, the average of this shear polymeric stress along the length of the sheet decreases — resulting in slower swimming speeds. To understand the differences between the small and moderate amplitude cases, consider the four extrema in shear polymeric stress per period, labelled I-IV in Fig. 2.4.

Due to the symmetry of the problem, extremum IV is the negative of extremum I, and extremum III the negative of extremum II. Let us just consider the upper fluid, which is the same as the lower due to this symmetry. At small wave amplitudes, the sheet is approximately located along the centreline of the vortex array and is equally close to all of the extrema of the polymeric shear stress. Whereas, at moderate amplitudes, this is no longer the case. The sheet is closer to extremum I than II (or IV than III in the lower fluid). The slowing mechanism is more pronounced near these extrema. Thus, whereas the slowing mechanism is applied evenly along the sheet at small amplitudes, at moderate amplitudes, the mechanism is stronger in the region $0 < x < \pi$, containing extremum I, than the region $\pi < x < 2\pi$, containing extremum II. As a result of this, the sheet is proportionally slowed down less at moderate amplitudes because the slowing mechanism happens less in some regions of the sheet.

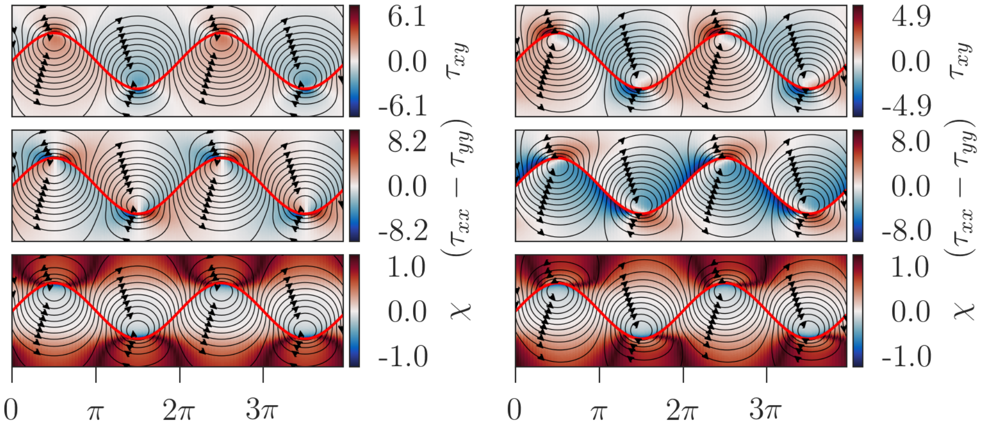

(a) De = 0.0. $U = U_N = 0.2649c$. **(b)** De = 1.0. $U = 0.806U_N$.

Figure 2.6 Colour plots of the polymeric stress tensor $\boldsymbol{\tau}$ and flow parameter χ in an Olrdoyd-B fluid surrounding a sine-waving sheet with amplitude $bk = 2.5$. The viscosity ratio is $\beta = 0.5$, $-5 \leq yk \leq 5$and the Deborah numbers are De = 0.0 and De = 1.0. The stress tensor components are in units of $\eta_p k^2 c$.

This explanation is corroborated by Fig. 2.5, which shows the polymeric shear stress in the upper fluid evaluated along the length of the sheet, at various Deborah numbers. For $bk = 0.01$, the polymeric shear stress is evenly reduced along the length of the sheet by increasing Deborah number. Whereas, for $bk = 0.5$, the reduction of the polymeric shear stress is stronger near extremum I than extremum II.

At large Deborah numbers, we can no longer neglect the non-linear viscoelastic responses. This is responsible for the vastly different polymeric stress distribution in Fig. 2.4f. In this regime, there is no longer a clear separation between the viscoelastic response and the interaction of that response with the vortices. In fact, the $\langle \tau_{xy}^{(2)} \rangle$ that we found in the small-amplitude calculation is one of the second-order non-linear viscoelastic responses. However, the presence of the plateau swimming speed suggests that at large Deborah numbers, the viscoelastic agents do not have time to react to the local shear flow. Thus, they only provide an elastic response that is independent of ω and the sheet's swimming speed is then unaffected by increasing Deborah number. Further study is required to understand the moderate-amplitude, large Deborah-number regime in more detail.

Interestingly, even at these large Deborah numbers, where the non-linear viscoelastic response is important, the topology of the flow field is unchanged at

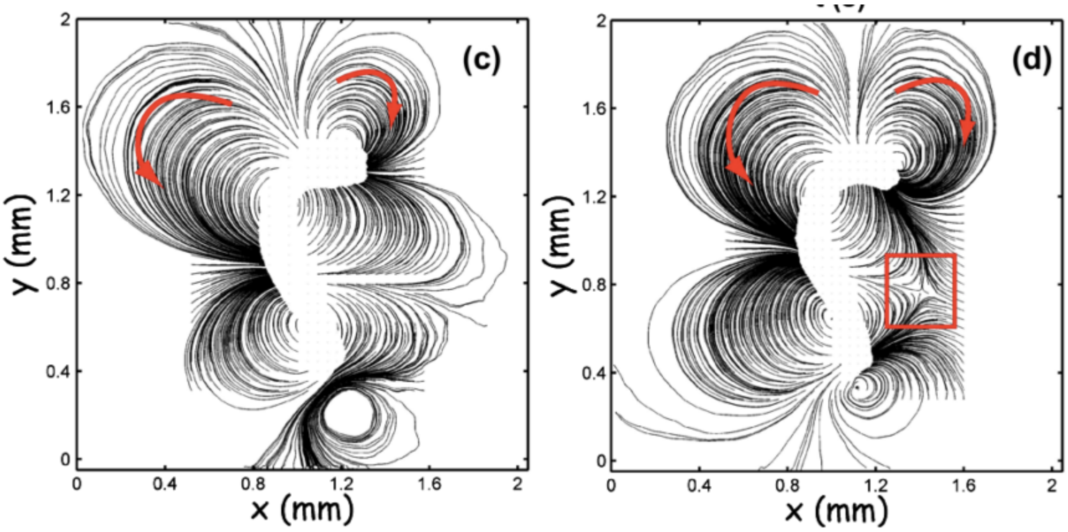

Figure 2.7 The flow field surrounding *C. elegans* worms in a Newtonian (left) and viscoeastic (right) fluid at similar times in the organisms' stroke. For both images Re $< 10^{-3}$ and in the viscoelastic case, De $= 3.0$. The streamlines have been calculated from instantaneous velocity fields obtained by PIV measurements. Adopted from [20].

moderate amplitudes. At large amplitudes, this is no longer the case, as shown in Fig. 2.6. Even at small Deborah numbers the topology of the flow is changed as the Deborah number increases, as demonstrated by the flow-type parameter plots.

We now compare our solutions to Taylor's waving sheet swimming in an Oldroyd-B fluid to Shen and Arratia's [20] observations of the flow field around a swimming nematode. We suggest our mechanism applies for such a swimmer.

2.4.3 Comparison to *C. elegans*

We can compare our finite-amplitude numerical results to the scaled swimming speeds of *C. elegans* in CMC solutions observed by Shen and Arratia [20], as shown in Fig. 1.7. Their *C. elegans* worms had a wave amplitude of $bk \approx 0.6$ and the viscosity ratio of their fluid was $\beta = 0.05$. Thus, from the numerical results shown in Fig. 2.2, we would predict that the scaled swimming speeds are only slightly faster than that of the small-amplitude calculation. This is not the case for *C. elegans*, where the 'plateau' (De ≈ 5) scaled swimming speed is $U/U_N \approx 0.5 \gg \beta$. This discrepancy is almost certainly because the worm *C. elegans* is a three-dimensional worm, which is poorly modelled by an infinite two-dimensional sheet.

However, the mechanism discussed in Section 2.4.1 should apply for any vortex array — not just that created by Taylor's sheet. Figure 2.7 shows Particle Image Velocimetry (PIV) measurements of the velocity field surrounding *C. elegans* worms made by Shen and Arratia [20]. This clearly shows the presence of a finite vortex array around the swimmer. This finite vortex array will create local oscillatory shear, just like the vortex array created by Taylor's sheet. There will be a viscoelastic response to this local oscillatory shear, which, when interacting with the vortices, will slow down the worm. At large Deborah numbers, the CMC in the solution does not have time to react to the local oscillatory shear; and so, it just provides an elastic response, which is independent of the frequency of the *C. elegans* kinematics. Thus, we observe a plateau swimming speed.

In this section, we have discussed the mechanism responsible for the behaviour of the swimming speed of the sheet as a function of Deborah number in the the different wave-amplitude regimes. We now show how we can use this mechanistic understanding of a moderate-amplitude swimmer to design a new swimmer, based on Taylor's sheet, which avoids the mechanism at small Deborah numbers.

2.5 Enhanced swimming in viscoelastic fluids

The analysis of moderate amplitude sine-waving sheets suggests that, at small Deborah numbers, the reduction in swimming speed as the Deborah number increases is still due to the small-amplitude mechanism. It also suggests that if an extremum of the shear polymeric stress τ_{xy} is far from the sheet, then it does not contribute to the slowing down of the sheet. If we can design a transverse wave swimmer with no extrema of shear polymeric stress near the organism, then perhaps we can avoid the small-amplitude mechanism completely. Here, we give an example of one such swimmer: a Gaussian peristaltic swimmer.

To begin, note that for a sine wave it is the peaks that are close to the extrema of shear polymeric stress in the fluid above the sheet. In contrast, the troughs are far from the extrema in the upper fluid. Now, consider a sheet with a Gaussian waveform with amplitude b and width a given by

$$f(\zeta) = b - 2b \exp\left\{ \frac{-(\zeta - \pi)^2}{a^2} \right\} \text{ for } 0 < \zeta < 2\pi, \tag{2.34}$$

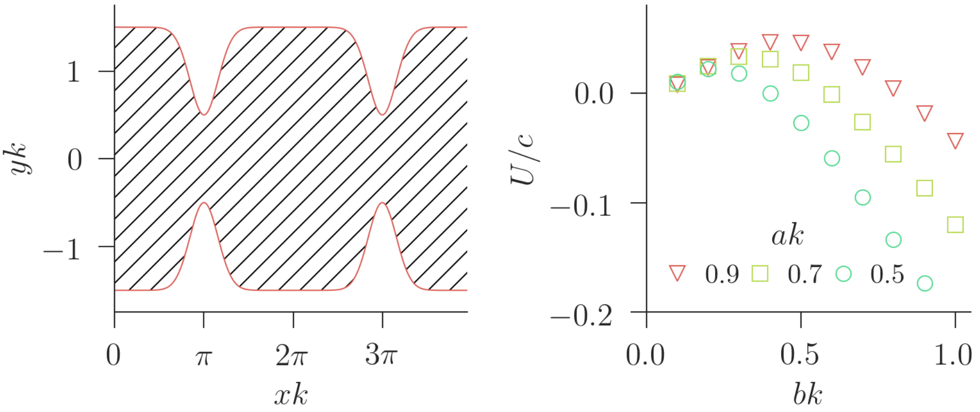

(a) A Gaussian peristaltic swimmer with $ak = 0.7$, $bk = 0.5$

(b) Speed of peristaltic swimmer with amplitude b in a Newtonian fluid.

Figure 2.8 A schematic of a Gaussian peristaltic swimmer and its swimming speed U, scaled by the wave speed c, against amplitude b for various widths a. The waveform of the upper edge is given by $f(\zeta) = 3b - 2b\exp\{-(\zeta-\pi)^2/a^2\}$ (for $0 < \zeta < 2\pi$) with $bk = 0.5$. The hatched regions are the interior of the organism; whereas, the clear regions are the surrounding fluid. At small amplitudes, the organism swims against the wave like a sheet. However, at large amplitudes, the organism swims in the same direction as the wave.

where $f(\zeta + 2\pi) = f(\zeta)$ such that the waveform is periodic. Although the derivative of this waveform is not continuous, provided that the dimensionless width a is sufficiently small, this discontinuity will be negligible. As this is still a transverse wave, the core mechanism of vortex creation is still present. The extrema of the polymeric stress are arranged in the same relationship to the shape of the sheet as for the sine waveform.

The key difference between the sine waveform and the Gaussian waveform is that the latter is without peaks, thus there should be no extrema of polymeric shear stress in the upper fluid that are close to the sheet. However, we will still expect the extrema of shear polymeric stress in the lower fluid to be close to the remaining troughs. Thus, we expect the sheet to still be slowed down.

To avoid the troughs in the lower region, consider the following. Rather than a thin sheet, consider a sheet with some thickness d. And rather than a transverse wave propagating along the sheet as a whole, imagine that there is some internal mechanism that can contract regions of the sheet such that there is a transverse wave propagating along each edge of sheet. This is shown for a Gaussian waveform in Fig. 2.8a.

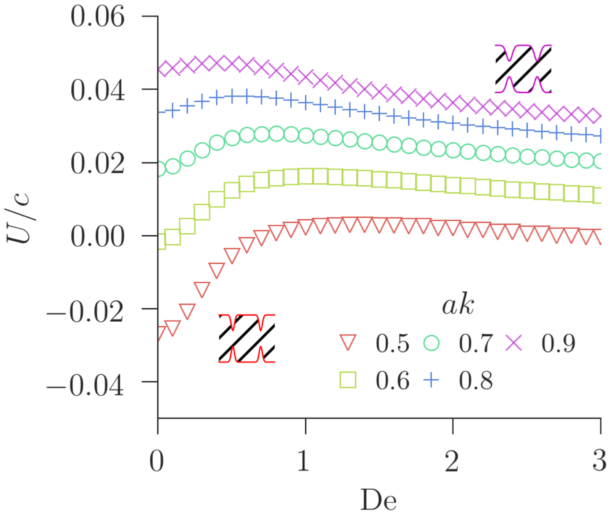

Figure 2.9 The swimming speed U, in the negative x-direction, against Deborah number De for a Gaussian peristaltic swimmer for different spike widths a. The waveform of the upper edge is given by $f(\zeta) = 3b - 2b\exp\{-(\zeta - \pi)^2/a^2\}$ $(0 < \zeta < 2\pi)$. The swimming speeds are scaled by the wave speed c. For small De, the swimming speed is more positive than in the Newtonian case, but at a larger De, it becomes more negative. The peak swimming speed occurs at higher De for thinner spikes.

This peristaltic swimmer has an up-down symmetry for any waveform, like the sine-waving sheet. Thus, the regions above and below the fluid are the same, and we can use our numerical solver described in Section 2.3 to find the swimming speed of the new swimmer. We can find the Newtonian swimming speeds by setting De $= 0$.

The swimming speed U_N of this peristaltic swimmer in a Newtonian fluid against wave amplitude is shown at various widths, a, in Fig. 2.8b. At all amplitudes the swimming speed of the peristaltic Gaussian swimmer is worse than a sine-waving sheet at similar amplitudes. At small wave amplitudes, the organism swims in the opposite direction to the wave, like a sheet. However, at large wave amplitudes, the peristaltic swimmer swims in the same direction as the wave.

This Newtonian behaviour is explained by a similar vortex mechanism as the sine-waving sheet. Similarly to the sheet, the vertical motion of the material points of the organism creates an array of counter-rotating vortices. The clockwise-rotating vortices are associated with troughs and the anticlockwise-rotating vortices associated with the peaks. As the peaks of the Gaussian waveform have been flattened relative to the sine waveform, the anticlockwise-rotating vortices are much weaker than their clockwise-rotating counterparts. Thus, compared to a sine-waving sheet, there are fewer vortices per wavelength pushing the sheet, which explains why the new swimmer is worse than its sine-waving colleague.

At small amplitudes, the centre of the vortex is above the edge of the swimmer. Just as with the sine wave, the vortices push in the opposite direction to the wave. Looking at the flow fields surrounding these swimmers at different amplitudes (not shown), it is apparent that as the wave amplitude increases the centre of the clockwise-rotating vortices decreases. For a given width, there is some amplitude where this centre crosses into the interior of the peristaltic swimmer. In this scenario, the vortex begins to push in the same direction as the wave, and thus, the organism swims in that direction. It is unclear what causes the lowering of the centre of the vortex, for the peristaltic swimmer. It does not seem to occur for a sheet with the Gaussian waveform.

In an Oldroyd-B fluid, the Gaussian peristaltic swimmer does not extend into the regions of large shear polymeric stress. Thus, we expect that the small-amplitude mechanism responsible for the slow down of the sheet as Deborah number increases will not occur at small Deborah numbers for the new swimmer. In fact, we find that there is a mechanism, which initially enhances the swimming speed of the organism as the Deborah number is increased from zero. This is shown in Fig. 2.9 for a Gaussian wave with amplitude $bk = 0.5$ at various widths. Note that the pushing effect of the polymers is related to the direction of the wave, as opposed to being related to the direction of swimming. Thus, the enhanced propulsion speed only occurs if the swimmer swims against the direction of the wave in a Newtonian fluid.

Figure 2.10 shows the polymeric stress fields, $\boldsymbol{\tau}$ and flow type parameter χ for the fluid above a Gaussian peristaltic swimmer, with amplitude $bk = 0.5$ and width $a = 0.7$ at Deborah numbers $\mathrm{De} = 0.0$ and $\mathrm{De} = 1.0$. As expected, the extrema of the shear polymeric stress do not occur near the edge of the swimmer, which explains why we do not observe a slow down as in the case of the sine-waving sheet. This separation of the shear stress from the swimmer is shwon in Fig. 2.11. However, note that unlike a sine-waving sheet at this amplitude, increasing the Deborah number has changed the flow field surrounding the organism, as illustrated by the flow-type parameter.

Using our small-amplitude mechanism as a design principle, we successfully designed a peristaltic swimmer that avoids the mechanism at small Deborah numbers. This suggests that our understanding of the mechanism at moderate

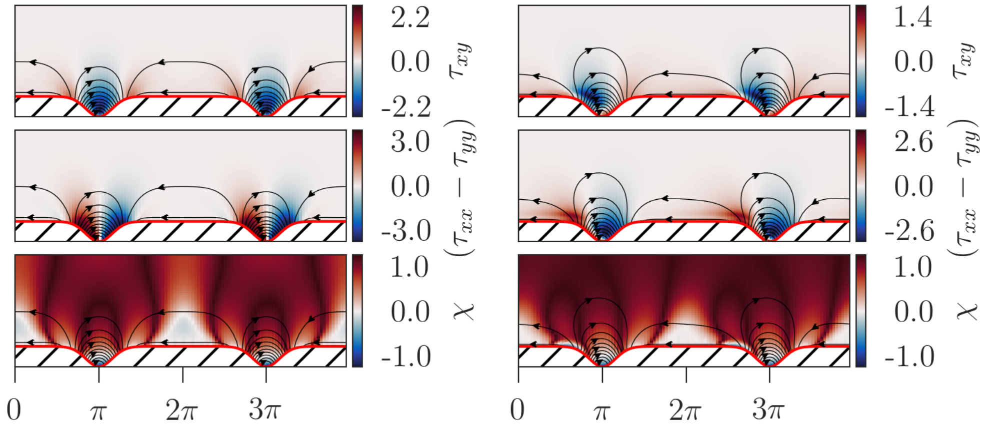

(a) De $= 0.0$. $U = 1.834 \times 10^{-2}c$ **(b)** De $= 1.0$. $U = 1.501 U_N$.

Figure 2.10 The polymeric stress tensor $\boldsymbol{\tau}$ and flow parameter χ above a Gaussian peristaltic swimmer with amplitude $bk = 0.5$ and spike width $a = 0.7$. Here, $\beta = 0.5$, $0 < yk < 5$. The stress tensor components are in units of $\eta_p k^2 c$.

amplitudes and small Deborah numbers is correct. The flow field surrounding the new swimmer is changed by the introduction of viscoelasticity, which leads to it swimming more quickly in the negative x-direction.

2.6 Conclusion

In an Oldroyd-B fluid, the swimming speed of a small-amplitude sine-waving Taylor's sheet decreases monotonically with Deborah number, reaching a plateau swimming speed at large Deborah numbers. In this chapter, we have provided a mechanistic explanation of this behaviour.

The vortices created by the sheet generate local oscillatory shear at each point in the fluid. At small amplitudes, there is a linear viscoelastic response to this local oscillatory shear. The linear viscoelastic response interacts with the vortices. Due to the geometry of the vortices, this response then pushes the sheet in the direction of the wave. This results in the slowing down of the sheet. At large Deborah numbers, the viscoelastic agents in the fluid do not have time to react to the local oscillatory shear and so, respond purely elastically. This elastic response is independent of the frequency of the wave. Thus, in this regime, the swimming speed is independent of Deborah number.

We have shown that at moderate amplitudes, the mechanism described above is

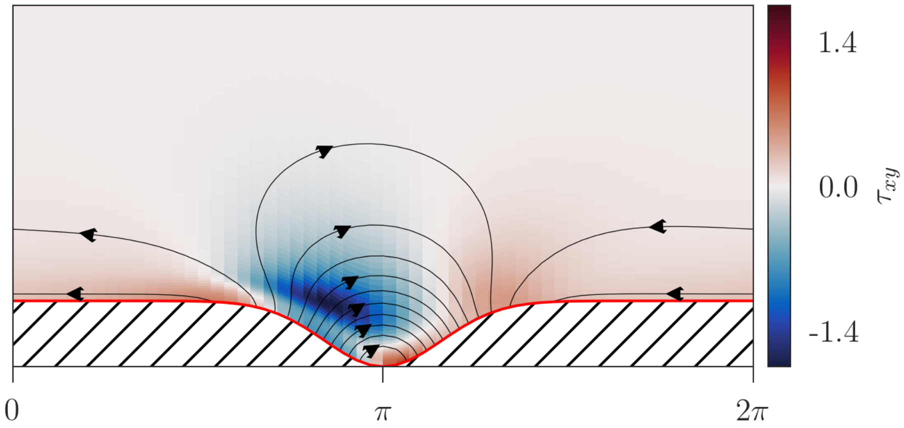

Figure 2.11 The polymeric shear stress τ_{xy} above a Gaussian peristaltic swimmer with amplitude $bk = 0.5$ and spike width $a = 0.7$. Here, $\beta = 0.5$, $0 < yk < 5$ and $\mathrm{De} = 1.0$. The extrema of the shear stress is far from the sheet, reducing the slow down caused by the presence of viscoelastic agents, compared to a sine waving sheet.

responsible for the slow down of the sheet at small Deborah numbers. However, at larger Deborah numbers, non-linear viscoelastic effects become important. Furthermore, at large Deborah numbers, the viscoelastic agents still do not have time to react to the local oscillatory shear and respond elastically, leading to plateau swimming speeds at moderate wave amplitudes.

This mechanism is universal in that it occurs for any microswimmer that creates a vortex array like Taylor's sheet. For example, this mechanism is probably responsible for the slowing down of *C. elegans*.

Using this mechanism as a guide, we have designed a Gaussian peristaltic swimmer that is far from all the regions of large polymeric shear stress and, as such, avoids the mechanism entirely. This peristaltic swimmer does not slow down as the Deborah number is initially increased. In fact at small Deborah numbers, it swims faster than in a Newtonian fluid. The success of this design suggests that our mechanism for moderate-amplitude swimming in a viscoelastic fluid is correct.

Now that we have established the mechanism in this simplest of cases, we consider the more complicated, but also more common situation, of swimming next to a wall.

Chapter 3

Swimming next to a wall in a viscoelastic fluid

3.1 Introduction

In Chapter 2, we examined Taylor's sheet swimming through the bulk of a viscoelastic fluid. While this situation is simpler, it is perhaps not as biologically relevant as swimming next to a wall, given that many microorganisms in their natural habitat swim in confined geometries. Many studies have considered swimming next to a boundary; but few of them do so in a viscoelastic fluid. In this chapter, we provide a mechanistic explanation for the behaviour of Taylor's sheet when swimming next to a wall in a viscoelastic fluid.

Following the success of Taylor's sheet [5] in understanding swimming in the bulk of a Newtonian fluid, Katz [74] extended the small-amplitude calculation to include the effects of swimming next to a solid boundary. Katz's analysis showed that a sine-waving sheet (with amplitude b, wavenumber k, wave speed c and with a solid planar boundary at a distance h from its centreline) swims in the opposite direction to the wave, with a speed U_N. To the lowest order in bk, the speed is given by

$$U_N = c\frac{b^2k^2}{2}\left(\frac{\sinh^2(hk)+h^2k^2}{\sinh^2(hk)-h^2k^2}\right). \tag{3.1}$$

Notably, for any finite value of h, this speed is larger than $U_{BN} = cb^2k^2/2$, the swimming speed in the bulk of a Newtonian fluid. However, this conclusion relies on the assumption that the organism maintains the same kinematics next to a wall as in the bulk. Katz's work later inspired various investigations into swimming close to a surface for different model swimmers [74, 82–88]. With the notable exception of [28–30], these studies are also concerned with microswimming in Newtonian fluids. However, many biological microswimmers have ecological environments in which they are both swimming through a viscoelastic fluid and next to a boundary. Examples range from sperm moving in a mucus film along the cervix wall [14, 63, 89] to bacterial pathogens invading biofilms of different bacterial species [17]. In this Chapter, we will mathematically investigate the swimming of microorganisms in viscoelastic fluids next to a boundary, using Taylor's waving sheet as a model swimmer.

The first step in investigating the swimming of Taylor's sheet in a viscoelastic fluid next to a boundary was taken by Elfring and Lauga [75], who used a boundary integral method to calculate the swimming speed of a small-amplitude Taylor sheet swimming next to a boundary in an Oldroyd-B fluid. They found that to the lowest order in bk, the swimming speed U is given by

$$U = c\frac{b^2k^2}{2}\left(\frac{1+\beta\mathrm{De}^2}{1+\mathrm{De}^2}\right)\left(\frac{\sinh^2(hk)+h^2k^2}{\sinh^2(hk)-h^2k^2}\right). \tag{3.2}$$

Recall that Lauga [22] extended the small-amplitude Taylor's waving sheet calculation and found that the swimming speed of a sine-waving sheet in an Oldroyd-B fluid is, to lowest order in bk, given by

$$U_B = c\frac{b^2k^2}{2}\left(\frac{1+\beta\mathrm{De}^2}{1+\mathrm{De}^2}\right), \tag{3.3}$$

where $\mathrm{De} = \lambda ck$ is the Deborah number of the fluid, with λ being the longest relaxation time of the fluid and $\beta = \eta_s/(\eta_s + \eta_p)$, with η_s and η_p being the solvent and polymer viscosities, respectively. This is similar to the wall case, in that Eq. (3.3) is U_{BN} multiplied by some factor, depending here on De and β as opposed to h.

Thus, Eq. (3.2) is a combination of the swimming speeds U_N and U_B, i.e. U is U_{BN} multiplied by both of the factors that multiply U_{BN} in Eqs. (3.1) and (3.3). Furthermore, the effects of viscoelasticity and the boundary factorise. In Chapter 2, we discussed a mechanistic explanation for Eq. (3.3). The purpose of this chapter is to provide such a mechanistic explanation of the interplay

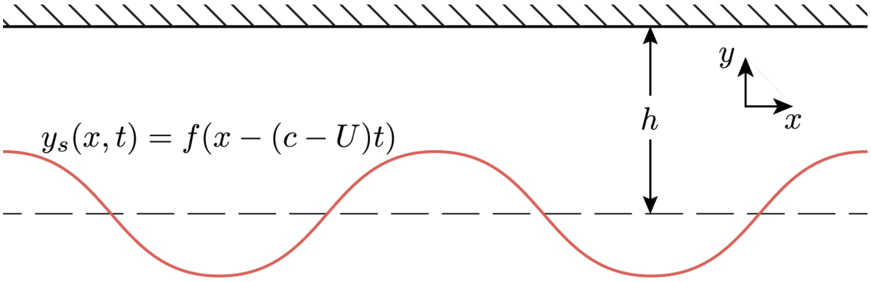

Figure 3.1 A schematic of a cross-section of Taylor's sheet a distance h below a wall with a waveform $f(x)$.

between viscoelasticity of the fluid and the presence of a solid wall.

3.1.1 The model

In this chapter, we solve the problem of Taylor's waving sheet swimming through an Oldroyd-B fluid below a wall. Recall from Section 1.1.3 that the sheet is a microswimmer that propagates a wave at a speed c in the positive x-direction. The sheet traces out a shape y_s in the xy-plane. At a time t, this shape is given by

$$y_s(x,t) = f(k(x-(c-U)t)), \tag{3.4}$$

where f is the waveform, k is the associated wavenumber and U is the swimming speed of the sheet in the negative x-direction. The wall is at a distance h above the centreline of the organism, see Fig. 3.1.

To examine the situation sketched in Fig. 3.1, we solve a slightly more general problem of the sheet, in a channel with walls both above and below it, placed at distances h_+ and h_- from the centreline, respectively. We then return to the original single-wall problem by taking $h_+ \to h$ and $h_- \to \infty$.

To find the swimming speed, we first calculate the velocity fields $\boldsymbol{u}_\pm = (u_\pm, v_\pm)^T$ in the surrounding fluid. Here and throughout this chapter, "+" and "−" denote above and below the sheet, respectively. Due to the presence of the walls in both domains, the fluid above and below are equivalent and so we drop the ± unless necessary. To find the velocity fields, we solve the Stokes-Oldroyd-B equations

$$-\nabla p + 2\eta_s \nabla \cdot \mathbf{D} + \nabla \cdot \boldsymbol{\tau} = \mathbf{0}, \tag{3.5a}$$

$$\nabla \cdot \boldsymbol{u} = 0, \tag{3.5b}$$

$$\boldsymbol{\tau} + \lambda \overset{\triangledown}{\boldsymbol{\tau}} = 2\eta_p \mathbf{D}, \tag{3.5c}$$

where p are the pressure fields, $\boldsymbol{\tau}$ are the polymeric contributions to the stress, $\mathbf{D} = (\nabla \boldsymbol{u} + \nabla \boldsymbol{u}^T)/2$ is the strain rate tensor. The upper-convected Maxwell derivative is given by

$$\overset{\triangledown}{\boldsymbol{\tau}} = \partial_t \boldsymbol{\tau} + \boldsymbol{u} \cdot \nabla \boldsymbol{\tau} - \nabla \boldsymbol{u}^T \cdot \boldsymbol{\tau} - \boldsymbol{\tau} \cdot \nabla \boldsymbol{u}.$$

See Section 1.2.3 for more details.

The boundary conditions are the usual no-slip boundary conditions at the sheet and the wall, given by

$$\boldsymbol{u}\big|_{y=y_s} = \boldsymbol{u}_s, \tag{3.6a}$$

$$\boldsymbol{u}\big|_{y=h} = \boldsymbol{u}_w, \tag{3.6b}$$

where $\boldsymbol{u}_s$ and $\boldsymbol{u}_w$ are the velocity of the material points of the sheet and the wall, respectively.

This chapter is organised as follows. In Section 3.2, we consider a small-amplitude Taylor's sheet swimming between two boundaries in an Oldroyd-B fluid. We re-derive the result obtained by Elfring and Lauga [75], Eq. (3.2), using the same method as we have used for previous small-amplitude calculations, in order to obtain explicit expressions for the velocity and stress fields around the swimmer. In Section 3.3, we adapt the numerical solver used in Chapter 2 to allow for swimming between two boundaries, and use it to find the swimming speed of sine-waving sheets of any amplitude. Finally, in Section 3.4, we use the velocity and stress fields calculated in the previous sections to explain the origin of Eqs. (3.1) and (3.2), and discuss the emerging mechanism of propulsion.

3.2 Small-amplitude analysis

In this section, we outline an alternative to Elfring and Lauga's calculation of the swimming speed of a sine-waving sheet ($f(\zeta) = b\sin(\zeta)$) in an Oldroyd-B fluid between two boundaries. This alternative method more closely mirrors the approach used in Chapter 2 and in the process finds the hydrodynamic fields surrounding the sheet. These hydrodynamic fields will be useful in investigating the physical mechanism responsible for decoupling the effects of the wall and the viscoelasticity in Eq. (3.2).

We begin by simultaneously introducing dimensionless variables and removing any explicit time dependence, with the help of a transformation to starred quantities

$$
\begin{gathered}
x^* = k(x - ct),\ y^* = ky,\ y_s^* = ky_s,\ h^* = hk, \\
U^* = \frac{U}{c},\ u^* = 1 + \frac{u}{c},\ v^* = \frac{v}{c}, \\
p^* = \frac{p}{\eta ck},\ \boldsymbol{\tau}^* = \frac{\boldsymbol{\tau}}{\eta_p ck},\ \boldsymbol{\Sigma}^* = \frac{\boldsymbol{\Sigma}}{\eta ck}.
\end{gathered}
$$

In this frame, we are co-moving with the wave. The velocity of the walls is $\boldsymbol{u}_w^* = -\boldsymbol{e}_x$ and the shape of the sheet is approximately fixed in time, such that $y_s^*(x^*) = \epsilon\sin(x^*) + \mathcal{O}(\epsilon^3)$, where $\epsilon = bk$ is the dimensionless wave amplitude. Our goal is to find the steady state velocity field surrounding the sheet and, from this, to calculate the sheet's swimming speed. From now on, we will drop the *s.

We expand the fields p, $\boldsymbol{u}$ and $\boldsymbol{\tau}$ into Taylor series about $\epsilon = 0$. For example, the pressure fields are given by

$$
p = \sum_{n=0}^{\infty} p^{(n)}\epsilon^n, \tag{3.7}
$$

where $p^{(n)}$ is the 'nth-order' contribution to the pressure field.

The velocity field is the solution to Eq. (3.5), subject to the no-slip boundary conditions of Eq. (3.6). The first order velocity of the material points of the sheet are given by

$$
u_s = -1 + \mathcal{O}(\epsilon^2), \tag{3.8a}
$$

$$
v_s = -\epsilon\cos(x) + \mathcal{O}(\epsilon^2). \tag{3.8b}
$$

The swimming speed of the sheet is found by averaging the velocity field along the length of the sheet and, up to the second order in ϵ, the swimming speed of the sheet is given by

$$U = -\langle y_s\, \partial_y u^{(1)}\Big|_{y=0}\rangle \epsilon - \langle u^{(2)}\Big|_{y=0}\rangle \epsilon^2, \tag{3.9}$$

where the $\langle ... \rangle$ above are x-averages.

Substituting the Taylor expansion of each of the fields into Eq. (3.5) and considering each power of ϵ separately, we have, for the zeroth-order, the following set of equations

$$\begin{aligned} -\nabla p^{(0)} + \beta \nabla^2 \boldsymbol{u}^{(0)} + (1-\beta)\nabla \cdot \boldsymbol{\tau}^{(0)} &= \mathbf{0}, \\ \nabla \cdot \boldsymbol{u}^{(0)} &= 0, \\ \boldsymbol{\tau}^{(0)} &= \mathbf{D}^{(0)}, \\ \boldsymbol{u}^{(0)}\Big|_{y=y_s} = \boldsymbol{u}^{(0)}\Big|_{y=h} &= -\boldsymbol{e}_x, \end{aligned}$$

which has the solution $p^{(0)} = 0$, $\boldsymbol{\tau}^{(0)} = \mathbf{0}$, and $\boldsymbol{u}^{(0)} = -\boldsymbol{e}_x$. This zeroth-order solution does not contribute to the swimming speed of the sheet directly. However, it is used to find the higher order solutions.

The argument we used in Section 2.2 to show that the first order solution is the same for an Oldroyd-B fluid as for a Newtonian fluid is also valid here. Thus, the solution to the first order set of equations is the same as those Katz [76] found for the Newtonian case. The set of first-order equations is given by

$$-\nabla p^{(1)} + \beta \nabla^2 \boldsymbol{u} + \nabla \cdot (1-\beta)\boldsymbol{\tau}^{(1)} = \mathbf{0}, \tag{3.10a}$$

$$\nabla \cdot \boldsymbol{u}^{(1)} = 0, \tag{3.10b}$$

$$(1 - \mathrm{De}\; \partial_x)\boldsymbol{\tau}^{(1)} = \mathbf{D}^{(1)}, \tag{3.10c}$$

$$\boldsymbol{u}^{(1)}\Big|_{y=y_s} = -\cos(x)\boldsymbol{e}_y, \;\; \boldsymbol{u}^{(1)}\Big|_{y=h} = \mathbf{0}, \tag{3.10d}$$

where we have used $\boldsymbol{u}^{(0)}$. Katz's solution is given by

$$u_{\pm}^{(1)} = (1 + A_{\pm} - B_{\pm} y)\sin(x)\sinh(y) + A_{\pm} y \sin(x)\cosh(y), \tag{3.11a}$$

$$v_{\pm}^{(1)} = -(A_{\pm} y + B_{\pm})\cos(x)\sinh(y) - (1 - B_{\pm} y)\cos(x)\cosh(y), \tag{3.11b}$$

where

$$A_{\pm} = \frac{\sinh^2(h_{\pm})}{\sinh^2(h_{\pm}) - h_{\pm}^2}, \; B_{\pm} = \frac{\pm\sinh(h_{\pm})\cosh(h_{\pm}) \pm h_{\pm}}{\sinh^2(h_{\pm}) - h_{\pm}^2}.$$

The contribution of this field to the swimming speed is given by the first term of Eq. (3.9), which is given by

$$-\langle y_s\, \partial_y u^{(1)}\Big|_{y=0}\rangle \epsilon = \epsilon^2 (A + \frac{1}{2}) + \mathcal{O}(\epsilon^3). \tag{3.12}$$

Here, we have dropped the explicit ± notation again, but we note that this contribution to the swimming speed is different for each region of the fluid. Below, we ensure that the total swimming speed is the same, regardless of whether we use the fluid velocity above or below the sheet. Before doing this, we will calculate the second term in Eq. (3.9).

The second-order set of governing equations is given by

$$-\nabla p^{(2)} + \beta \nabla^2 \boldsymbol{u}^{(2)} + (1-\beta)\nabla \cdot \boldsymbol{\tau}^{(2)} = \boldsymbol{0}, \tag{3.13a}$$

$$\nabla \cdot \boldsymbol{u}^{(2)} = 0, \tag{3.13b}$$

$$(1 - \mathrm{De}\,\partial_x)\boldsymbol{\tau}^{(2)} = \mathbf{D}^{(2)} - \mathrm{De}\Big[\boldsymbol{u}^{(1)} \cdot \nabla \boldsymbol{\tau}^{(1)} - (\nabla \boldsymbol{u}^{(1)})^T \cdot \boldsymbol{\tau}^{(1)} - \boldsymbol{\tau}^{(1)} \cdot \nabla \boldsymbol{u}^{(1)}\Big]. \tag{3.13c}$$

We have left out the boundary conditions, which we deal with later. We only need the x-average of $\boldsymbol{u}^{(2)}$ to find the second-order swimming speed. We find this x-average by considering the x-averages of the x-component of Eq. (3.13a) and the xy-component of Eq. (3.13c), giving

$$\beta \partial_{yy} \langle u^{(2)} \rangle + (1-\beta)\partial_y \langle \tau_{xy}^{(2)} \rangle = 0, \tag{3.14a}$$

$$\begin{aligned} \langle \tau_{xy}^{(2)} \rangle = \partial_y \langle u^{(2)} \rangle - \mathrm{De}\Big[&\langle u^{(1)} \partial_x \tau_{xy}^{(1)} \rangle + \langle v^{(1)} \partial_y \tau_{xy}^{(1)} \rangle - \\ &\langle D_{xy}^{(1)} (\tau_{xx}^{(1)} + \tau_{yy}^{(1)}) \rangle + \langle \Omega_{xy}^{(1)} (\tau_{xx}^{(1)} - \tau_{yy}^{(1)}) \rangle\Big], \end{aligned} \tag{3.14b}$$

where $\boldsymbol{\Omega} = (\nabla \boldsymbol{u}^T - \nabla \boldsymbol{u})/2$ is the vorticity tensor, and we have ignored the x-averages of x-derivatives of x-periodic functions, which must vanish. Since the first order fields are known, Eq. (3.14) is simply an ordinary differential equation for $\langle u^{(2)} \rangle$, the solution to which is given by

$$\langle u_\pm^{(2)} \rangle = E_\pm + F_\pm y + \frac{(1-\beta)\mathrm{De}^2}{4(1+\mathrm{De}^2)} \Big[G_\pm \cosh(2y) + H_\pm \sinh(2y) \Big], \tag{3.15}$$

where

$$\begin{aligned} G_\pm &= (2 + 4A_\pm + A_\pm^2 - B_\pm^2) - 4B_\pm(1 + A_\pm)y + 2(A_\pm^2 + B_\pm^2)y^2, \\ H_\pm &= 2A_\pm(B_\pm + 2(1 + A_\pm)y - 2B_\pm y^2). \end{aligned}$$

Here, $E_\pm$ and $F_\pm$ are arbitrary constants.

Until now, the solutions in the domains above and below the sheet were completely independent. Their coupling is now ensured by applying appropriate boundary conditions, which determine the constants $E_\pm$ and $F_\pm$. Similar to the solution developed by Katz [76] for Taylor's sheet swimming between two boundaries in a Newtonian fluid, we require that: (i) the swimming speeds we calculate from the upper and lower fluids match; and that, (ii) the sheet is, on average and to the second order, force-free in the x-direction. The first-order flow field, which is the same as the first-order Newtonian flow field, does not apply a net-force to the sheet [76]; while the second order flow field contributes a force per unit area $\boldsymbol{\Sigma}^{(2)} \cdot \boldsymbol{n}_\pm \big|_{y=0}$, where $\boldsymbol{n}_\pm = \pm \boldsymbol{e}_y + \mathcal{O}(\epsilon)$ are the normals of the sheet. To the second order, these boundary conditions are given by

$$\langle u_\pm^{(2)} \rangle \Big|_{y=\pm h_\pm} = 0, \tag{3.16a}$$

$$\langle y_s \partial_y \, u_+^{(1)} \Big|_{y=0} \rangle \epsilon + \langle u_+^{(2)} \rangle \Big|_{y=0} \epsilon^2 = \langle y_s \partial_y \, u_-^{(1)} \Big|_{y=0} \rangle \epsilon + \langle u_-^{(2)} \rangle \Big|_{y=0} \epsilon^2, \tag{3.16b}$$

$$\beta \partial_y \langle u_+^{(2)} \rangle \Big|_{y=0} + (1-\beta) \langle \tau_{xy,+}^{(2)} \rangle \Big|_{y=0} = \beta \partial_y \langle u_-^{(2)} \rangle \Big|_{y=0} + (1-\beta) \langle \tau_{xy,-}^{(2)} \rangle \Big|_{y=0}, \tag{3.16c}$$

which result in

$$E_\pm = \frac{(1+\beta\mathrm{De}^2)}{(1+\mathrm{De}^2)} \frac{h_\pm(A_\mp - A_\pm)}{(h_+ + h_-)} + \frac{(1-\beta)\mathrm{De}^2}{(1+\mathrm{De}^2)}(A_\pm^2 - B_\pm^2), \tag{3.17a}$$

$$F_\pm = \frac{(1+\beta\mathrm{De}^2)}{(1+\mathrm{De}^2)} \frac{(A_\mp - A_\pm)}{(h_+ + h_-)} + \frac{(1-\beta)\mathrm{De}^2}{h_\pm(1+\mathrm{De}^2)}(J_\pm \cosh^2(h_\pm) + K_\pm \sinh^2(h_\pm)), \tag{3.17b}$$

where

$$\begin{aligned}J_\pm &= (1 - 2h_\pm B_\pm) + h_\pm^2(A_\pm^2 - B_\pm^2),\\ K_\pm &= (1 + 2A_\pm)(1 - 2h_\pm B_\pm) + (1 - h_\pm^2)(A_\pm^2 - B_\pm^2).\end{aligned}$$

Substituting the first and second order velocity fields into Eq. (3.9), we finally arrive at

$$\begin{aligned}U &= \frac{\epsilon^2(1+\beta\mathrm{De}^2)}{(h_+ + h_-)(1+\mathrm{De}^2)}\left[h_-\left(A_+ + \frac{1}{2}\right) + h_+\left(A_- + \frac{1}{2}\right)\right]\\ &= \frac{\epsilon^2(1+\beta\mathrm{De}^2)}{2(h_+ + h_-)(1+\mathrm{De}^2)}\left[h_-\left(\frac{\sinh^2(h_+) + h_+^2}{\sinh^2(h_+) - h_+^2}\right) + h_+\left(\frac{\sinh^2(h_-) + h_-^2}{\sinh^2(h_-) - h_-^2}\right)\right].\end{aligned} \tag{3.18}$$

In the limit of $h_+ \to hk$ and $h_- \to \infty$, we recover Eq. (3.2) as mentioned above. The main implication of this result is the observation that the effects of swimming next to a wall and swimming in an Oldroyd-B fluid decouple at small wave amplitudes. The mechanism of this decoupling is discussed in Section 3.4; but first we adapt our numerical solver to be able to calculate the swimming speed of the sheet, at finite wave amplitudes, near a solid boundary.

3.3 Finite-amplitude numerics

Here, we will adapt our numerical solver from Chapter 2 to solve Eq. (3.5), subject to the boundary conditions of Eq. (3.6) for an arbitrary wave, with any amplitude or waveform. As we stated in the introduction, the numerical method used here is similar to what we used in Section 2.3 and so this section will be somewhat repetitive.

In a similar fashion to the small-amplitude analysis, the only difference for the numerical solver between swimming in the bulk of a fluid and swimming next to a wall is the boundary conditions used.

We begin by performing the following transformation to the starred variables

$$
\begin{gathered}
x^* = k(x - (c - U)t),\ y^* = ky,\ f^* = kf,\ h_\pm^* = h_\pm k, \\
U^* = \frac{U}{c},\ u^* = 1 - U^* + \frac{u}{c},\ v^* = \frac{v}{c}, \\
p^* = \frac{p}{\eta c k},\ \boldsymbol{\tau}^* = \frac{\boldsymbol{\tau}}{\eta_p c k},\ \boldsymbol{\Sigma}^* = \frac{\boldsymbol{\Sigma}}{\eta c k},
\end{gathered}
$$

which render the problem dimensionless. Note that this transformation is different from the small-amplitude transformation because, in this frame of reference, the shape of the sheet is exactly independent of time, as opposed to being independent of time only in the limit of small wave amplitudes. Again, we drop the *s in what follows.

We introduce the stream-function $\psi(x, y)$ (with $u = \partial_y \psi$ and $v = -\partial_x \psi$) and solve the curl and divergence of Eq. (3.5a), along with the constitutive relation in Eq. (3.5c), which gives us

$$\beta \nabla^4 \psi - (1 - \beta)\Big[\partial_{xy}(\tau_{yy} - \tau_{xx}) + \Box^2 \tau_{xy}\Big] = 0, \tag{3.19a}$$

$$\nabla^2 p - (1 - \beta)\Big[\partial_{xx}\tau_{xx} + 2\partial_{xy}\tau_{xy} + \partial_{yy}\tau_{yy}\Big] = 0, \tag{3.19b}$$

$$\tau_{xx} - 2\partial_{xy}\psi + \mathrm{De}\Big[(\partial_y\psi\partial_x - \partial_x\psi\partial_y)\tau_{xx} - 2\tau_{xx}\partial_{xy}\psi - 2\tau_{xy}\partial_{yy}\psi\Big] = 0, \tag{3.19c}$$

$$\tau_{xy} + \Box^2\psi + \mathrm{De}\Big[(\partial_y\psi\partial_x - \partial_x\psi\partial_y)\tau_{xy} + \tau_{xx}\partial_{xx}\psi - \tau_{yy}\partial_{yy}\psi\Big] = 0, \tag{3.19d}$$

$$\tau_{yy} + 2\partial_{xy}\psi + \mathrm{De}\Big[(\partial_y\psi\partial_x - \partial_x\psi\partial_y)\tau_{yy} + 2\tau_{xy}\partial_{xx}\psi + 2\tau_{yy}\partial_{xy}\psi\Big] = 0, \tag{3.19e}$$

where $\Box^2 = \partial_{xx} - \partial_{yy}$, $\beta = \eta_s/(\eta_s + \eta_p)$ is the viscosity ratio, and $\mathrm{De} = \lambda c k$ is the Deborah number of the fluid.

We perform a pair of independent transformations from original coordinates (x, y) into a new set of coordinates $(\eta_\pm, \xi_\pm)$ in each domain. After this transformation, each domain is a periodic rectangular strip. The transformations are given by

$$\eta_\pm = x, \tag{3.20a}$$

$$\xi_\pm = 1 - 2\frac{\pm h_\pm - y}{\pm h_\pm - f(x)}. \tag{3.20b}$$

In each domain, $\xi_\pm = 1$ corresponds to the domain's wall, while $\xi_\pm = -1$ corresponds to the sheet, i.e. the lower domain has been flipped. The solutions in these domains only couple to each other through the boundary conditions at the sheet.

In each deformed domain $(\eta,\xi)\in[0,2\pi)\times[-1,1]$, the hydrodynamic variables are represented by truncated Fourier-Chebyshev series. For example, the pressure field, p, is given by

$$p(\eta,\xi)=\sum_{n=0}^{N-1}\sum_{m=0}^{M-1}p^{(nm)}F_n(\eta)T_m(\xi), \tag{3.21}$$

where $T_m(\xi)=\cos(m\arccos(\xi))$ is the mth Chebyshev polynomial, and

$$F_n(\eta)=\begin{cases}\sin(\frac{n+1}{2}\eta) & n \text{ odd}\\ \cos(\frac{n}{2}\eta) & n \text{ even,}\end{cases}$$

is the nth Fourier mode. In this chapter, we find that a resolution of $N=33$ and $M=80$ is typically required to achieve the desired error of no more than 0.5% in the swimming speed of the sheet.

The $NM\times NM$ spectral derivative matrices in the original (x,y)-space are calculated from the spectral derivative matrices in the transformed (η,ξ)-space. For each domain, this is given by

$$\left(\frac{\partial}{\partial x}\right)_\pm=\frac{\partial}{\partial\eta_\pm}+(\xi_\pm-1)\frac{f'(\eta_\pm)}{\pm h_\pm-f(\eta_\pm)}\frac{\partial}{\partial\xi_\pm}, \tag{3.22a}$$

$$\left(\frac{\partial}{\partial y}\right)_\pm=\frac{2}{\pm h_\pm-f(\eta_\pm)}\frac{\partial}{\partial\xi_\pm}. \tag{3.22b}$$

To calculate products of the fields represented in the spectral space, we use the Fast Fourier transform [78] with the following collocation points

$$\eta_{n_c}=\frac{2\pi n_c}{N_c}, \tag{3.23a}$$

$$\xi_{m_c}=\cos\left(\frac{\pi m_c}{M_c-1}\right). \tag{3.23b}$$

We evaluate the fields in the real space, calculate their product and transform the result back to the spectral space. Here, $n_c\in[0,N_c)$, $m_c\in[0,M_c)$, and the collocation resolution (N_c,M_c) is selected to satisfy $N_c>1.5N$ and $M_c>1.5M$ in order to avoid aliasing issues [77, 78].

Representing five governing equations in the truncated Fourier-Chebyshev basis for each fluid domain yields a set of $10NM$ non-linear algebraic equations that need to be complemented by the boundary conditions. The periodicity of the problem is implicitly enforced by the choice of a Fourier basis in the η-direction. As a result, we need six boundary conditions in each domain, along the lines $\xi = \pm 1$. When discretised, this generates $12N$ boundary conditions, which we must substitute into the original set of $10NM$ discretised governing equations. We use different boundary conditions for the $n = 0$ and the $n \neq 0$ Fourier modes — as the unknown swimming speed U appears in the zeroth mode of the velocity of the material points of the sheet and the x-derivative of the zeroth Fourier mode vanishes.

For the $n \neq 0$ mode we have to replace the equations in Eq. (3.19a), with the no-slip boundary conditions at both the sheet and the wall, Eq. (3.6), where the velocities of the material points of the sheet and the walls are given by [5]

$$u_s(x) = -\frac{Q}{\sqrt{1 + f'(x)^2}}, \tag{3.24a}$$

$$v_s(x) = -\frac{Qf'(x)}{\sqrt{1 + f'(x)^2}}, \tag{3.24b}$$

$$\boldsymbol{u}_w = (U - 1)\boldsymbol{e}_x, \tag{3.24c}$$

where

$$Q = \int_0^{2\pi} \sqrt{1 + f'(x)^2}\, \mathrm{d}x.$$

The four boundary conditions are (for the $n \neq 0$ Fourier modes) therefore,

$$\partial_y \psi|_{\xi=-1} = u_s, \tag{3.25a}$$

$$-\partial_x \psi|_{\xi=-1} = v_s, \tag{3.25b}$$

$$\partial_y \psi|_{\xi=1} = U - 1, \tag{3.25c}$$

$$-\partial_x \psi|_{\xi=1} = 0. \tag{3.25d}$$

At both the sheet and the wall, we require that $\boldsymbol{n}\cdot\nabla\cdot\boldsymbol{\Sigma} = 0$, where $\boldsymbol{n}$ is the normal to the surface, in order to fix the divergence- and curl-free terms of Eq. (3.5a). This yields the final two boundary conditions for the $n \neq 0$ Fourier modes:

$$\begin{aligned}\Big[f'(\eta)\partial_x p - \partial_y p + \beta(f'(\eta)\partial_y - \partial_x)\nabla^2\psi +& \\ + f'(\eta)\partial_x \tau_{xx} + (f'(\eta)\partial_y + \partial_x)\tau_{xy} + \partial_y \tau_{yy}\Big]_{\xi=-1} &= 0,\end{aligned} \tag{3.26a}$$

$$\Big[\partial_y p + \beta\partial_x \nabla^2\psi - \partial_x \tau_{xy} - \partial_y \tau_{yy}\Big]_{\xi=1} = 0, \tag{3.26b}$$

where $(0, -1)^T$ is the normal to the wall, and $(-f'(\eta), 1)^T$ the normal to the

	$n = 0$	$0 < n < N$
$0 \leq m < M - 4$	Equations (3.19a) to (3.19e)	Equations (3.19a) to (3.19e)
$m = M - 4$	Equation (3.27d)(+) (3.27e)(−) Equations (3.19b) to (3.19e)	Equation (3.25d) Equations (3.19b) to (3.19e)
$m = M - 3$	Equation (3.27c) Equations (3.19b) to (3.19e)	Equation (3.25c) Equations (3.19b) to (3.19e)
$m = M - 2$	Equation (3.27b) Equation (3.27a) Equations (3.19c) to (3.19e)	Equation (3.25b) Equation (3.26b) Equations (3.19c) to (3.19e)
$m = M - 1$	Equation (3.25a) Equation (3.26a) Equations (3.19c) to (3.19e)	Equation (3.25a) Equation (3.26a) Equations (3.19c) to (3.19e)

Table 3.1 An outline of how the $10NM$ descretised equations are constructed from the differential equations in Eq. (3.19) and the various boundary conditions Eqs. (3.25) to (3.27).

surface of the sheet.

For the $n = 0$ mode, we replace Eqs. (3.25a), (3.25b), (3.25d) and (3.26b) with alternative boundary conditions. Firstly, we fix the physically irrelevant constant terms in both ψ and p to some arbitrary values. Secondly, we require that the average x-force applied to the walls, the sheet and each fluid domain vanish. This is achieved by requiring that the force applied by each fluid to its corresponding wall vanishes. We also need to require that the total force applied by both fluids to the sheet vanishes also. For the final $n = 0$ condition, we require that the swimming speed calculated in each domain matches. Thus, the $n = 0$ boundary conditions are given by

$$p|_{\xi=1} = 0, \tag{3.27a}$$

$$\psi|_{\xi=1} = 0, \tag{3.27b}$$

$$\left[\beta\Box^2\psi - \tau_{xy}\right]_{\xi=1} = 0, \tag{3.27c}$$

$$\begin{aligned}&\left[f'(\eta_+)p_+ - 2\beta f'(\eta_+)\partial_{xy}\psi_+ - \beta\Box^2\psi_+ - f'(\eta_+)\tau_{xx,+} + \tau_{xy,+}\right]_{\xi_+=-1} - \\ &\left[f'(\eta_-)p_- - 2\beta f'(\eta_-)\partial_{xy}\psi_- - \beta\Box^2\psi_- - f'(\eta_-)\tau_{xx,-} + \tau_{xy,-}\right]_{\xi_-=-1} = 0,\end{aligned} \tag{3.27d}$$

$$\partial_y\psi_+|_{\xi_+=1} = \partial_y\psi_-|_{\xi_-=1}, \tag{3.27e}$$

where the absence of a ± implies that the boundary condition applies to both domains.

For each Fourier mode, we replace the four highest Chebyshev modes of the discretised Eq. (3.19a) and the two modes of Eq. (3.19b) with the boundary conditions presented above. Combining everything together gives the set of $10NM$ non-linear discretised equations, with the structure outlined in Table 3.1. With the solution to this set of equations, the swimming speed of the sheet is given by

$$U = \partial_y \psi|_{\xi=1} + 1. \tag{3.28}$$

To solve this set of non-linear equations, we use a Newton-Raphson method [78] with an analytically calculated Jacobian. For each set of parameters, we must start from the Newtonain case De = 0 and use its solution as the initial guess for a slightly higher De, repeating this process until the target Deborah number is reached. At sufficiently large De, the step in Deborah number becomes too small for computation times to be reasonable. Where this is the case, we only report up to that value in De.

3.3.1 Results

Let us verify that our numerical method correctly reproduces the small-amplitude prediction Eq. (3.2). In Fig. 3.2, we plot the swimming speed for a sheet with $bk = 0.01$ as a function of the Deborah number De for various distances to the wall and various viscosity ratios. As expected for this amplitude, the numerically computed swimming speeds (symbols) agree well with the analytical prediction of Eq. (3.2) (solid line). This demonstrates that the effects of swimming next to a wall decouple from the effects of swimming in a viscoelastic fluid at small amplitudes.

The situation changes significantly for finite values of the wave amplitude. In Fig. 3.3, we plot the swimming speed for a sine-waving sheet, with $bk = 0.5$ as a function of the Deborah number De for various distances to the wall and viscosity ratios. We observe that the numerical data now deviates significantly from the small-amplitude prediction in Eq. (3.2). Despite this deviation, for most values of h and β the swimming speed follows the same trend as predicted by Eq. (3.2): starting from its Newtonian value, it decreases monotonically with De and reaches a ‘plateau’ value at large Deborah numbers. However, for sufficiently small h ($hk = 1.05, 1.1$) at $\beta = 0.5$ and $\beta = 0.9$, the swimming speed breaks this trend and exhibits a non-monotonic dependence on De, reaching speeds faster than the Newtonian case for $\beta = 0.9$. These results are further discussed in the

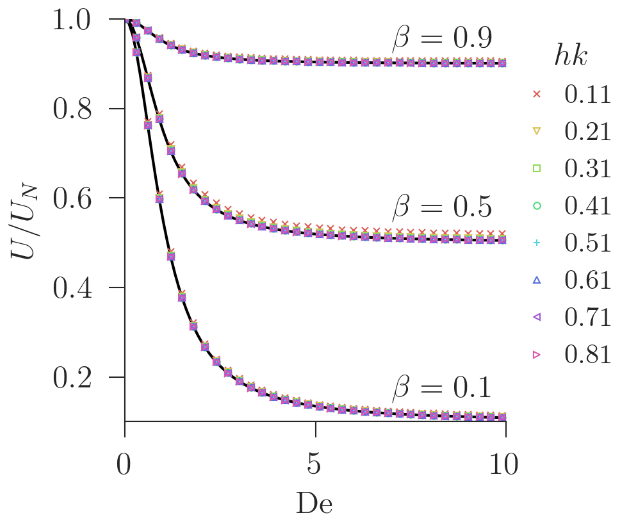

Figure 3.2 The swimming speed U of a small-amplitude ($bk = 0.01$) sine-waving sheet swimming next to a wall as the function of the Deborah number De for various viscosity ratios β and distances from the wall h. The swimming speeds are normalised by the swimming speed, U_N, of the same geometric situation in a Newtonian fluid. The numerical results (symbols) agree with the small-amplitude predictions (solid line).

next section.

3.4 Discussion

As we have demonstrated in Section 3.2, at small wave amplitudes, the influence of the polymeric stress on the swimming speed is the same for both swimming in the bulk and next to a wall. In other words, the effects of the boundary and viscoelastic agents decouple. The swimming speed is given by the product of the corresponding contributions, see Eq. (3.2). Let us discuss the mechanism of this behaviour.

Recall from Section 1.1.3 that the motion of the material points of the sheet creates a periodic array of vortices. In this chapter, we refer to these as 'sheet vortices'. These vortices push on the sheet, resulting in it swimming in the negative x-direction. When this configuration of sheet vortices is placed next to a solid boundary, as shown in Fig. 3.4, it generates a non-zero velocity at the boundary. In order to satisfy the no-slip boundary condition at the wall another array of vortices is created, which is localised near the wall and has the same periodicity as the sheet vortices, but each corresponding vortex has an opposite opposite sense. Along the boundary, the velocity of these 'wall vortices' has the same magnitude but opposite direction of the velocity of the sheet vortices, thus satisfying the no-slip boundary condition for the total velocity field. In turn, the wall vortices make a contribution to the velocity along the surface of the sheet, which causes an increase in the speed of the sheet vortices, in order to satisfy

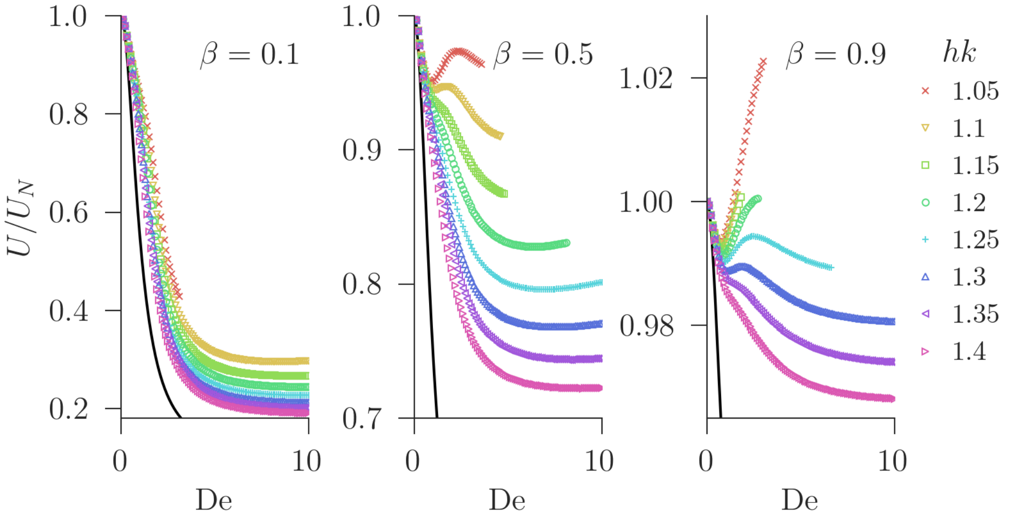

Figure 3.3 The swimming speed U of a finite-amplitude ($bk = 0.5$) sine-waving sheet swimming next to a wall as the function of the Deborah number De for various viscosity ratios β and distances from the wall h. The swimming speeds are normalised by the swimming speed, U_N, of the same geometric situation in a Newtonian fluid.

the no-slip boundary conditions at the sheet. It is this speed up of the sheet vortices which is responsible for the speeding up of the sheet in the presence of a boundary. The presence of the wall vortices also causes the sheet vortices to rise from the line $y = 0$. This has little effect on the Newtonian swimming speed; but, as we will see later, is important when considering the effects of viscoelasticity on swimming speed.

This argument is further corroborated by rearranging the first order velocity field Eq. (3.11) in the following form, with dimensional quantities

$$\begin{aligned}
u^{(1)} = {} & \frac{c}{2}((A+B)ky - A - 1)\sin(k(x-ct))\exp(-ky) + \\
& \frac{c}{2}((A-B)ky + A + 1)\sin(k(x-ct))\exp(ky), \\
v^{(1)} = {} & \frac{c}{2}((A+B)ky + B - 1)\cos(k(x-ct))\exp(-ky) + \\
& \frac{c}{2}((B-A)ky - B - 1)\cos(k(x-ct))\exp(ky),
\end{aligned}$$

where we have dropped the ±, as the fluid domains are equivalent and the distinction between them is unimportant. In the upper domain, the terms proportional to $\exp(-ky)$ and $\exp(ky)$ correspond to the sets of vortices which are localised at the sheet and at the wall, respectively. The centres of these vortices

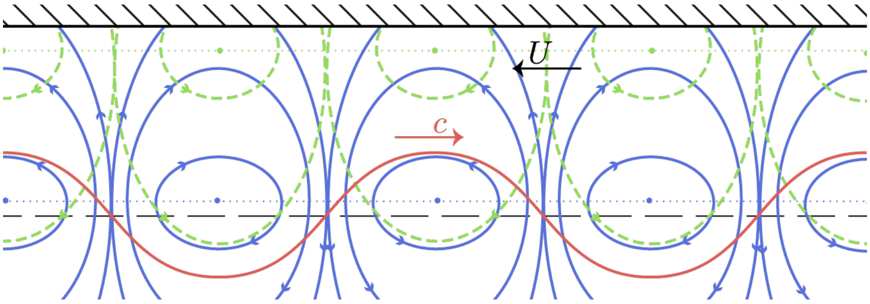

Figure 3.4 A *gedankenexperiment* demonstrating the sheet vortices (blue isolines) generated by the small-amplitude vertical motion of the material points of the sheet, and the velocity field it generates at an imaginary surface. Note that this velocity field does not satisfy the no-slip boundary conditions. The surface velocity is cancelled by the wall vortices (green isolines), as discussed in the text.

are located along the lines $ky = \omega_s$ and $ky = \omega_w$, where

$$\omega_s = \frac{A+1}{A+B} = \frac{h^2k^2}{hk + \sinh(hk)\cosh(hk) + \sinh^2(hk)},$$
$$\omega_w = \frac{A+1}{B-A} = \frac{h^2k^2}{hk + \sinh(hk)\cosh(hk) - \sinh^2(hk)}.$$

For $hk > 1$, $\omega_s \ll hk$ and $\omega_w \approx hk$, thus justifying the sheet and wall labels of the arrays of vortices.

With the identification of the sheet and wall vortices, we can now separate their contributions to the swimming speed. The sheet vortices still push the sheet in the negative x-direction, as the relationship between the vortices and the shape of the sheet is unchanged by the introduction of the wall. For small h, the wall vortices push the sheet in the positive x-direction, which slows the sheet down. The magnitude of the slowing force applied by the wall vortices is always less than the increase in the magnitude of the force applied by the sheet vortices. Thus, the sheet is sped up by the introduction of the wall. This is due to an increase in the speed of the sheet vortices.

Let us consider the effect that the viscoelasticity of the fluid has on the swimming speed. In Chapter 2, we described the mechanism responsible for the sheet swimming more slowly in a viscoelastic fluid than in a Newtonian fluid. We showed that the array of vortices surrounding the sheet created local oscillatory shear at each point in the fluid. There is a linear viscoelastic response to this local oscillatory shear. It is the interaction of this response with the vortex array which causes the sheet to slow down. The flow field surrounding the sheet next

Figure 3.5 A schematic of the advection term's contribution to the swimming speed in a Oldroyd-B fluid next to a wall. This image is in the frame of reference where the wave is stationary, thus the fluid is moving to the left at a speed c. The streamlines of the sheet vortex array are shown in grey. The blue dumbbells represent the xy-component of the first-order elastic response to the local oscillatory shear flow. The yellow dumbbells represent the elastic response after it has been advected by the vortices. See the text for more details.

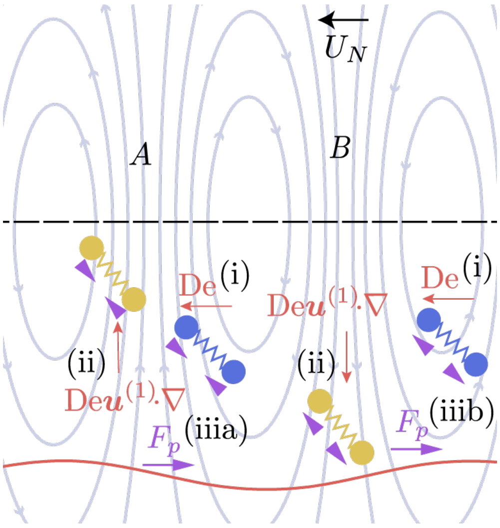

to a boundary is just the superposition of two vortex arrays. As a result, this mechanism is still occurring. Moreover, because the vortex arrays are out of phase with each other, the linear response to the sheet vortices does not interact with the wall vortices and vice-versa. Thus, each array of vortices is undergoing this mechanism separately. There are two additional considerations to the mechanism that must be made when swimming next to a wall: (a) the viscoelastic agents can now push on the wall; and (b) the objects being pushed no longer coincide with the centreline of the vortex array.

For consideration (a), pushing against the wall causes the entire fluid to move in order for the wall to remain force-free. Thus, pushing on the wall in the negative x-direction results in the sheet swimming more quickly in the positive x-direction. As the flow field associated with each vortex array scales as $\exp(-r)$, where r is the distance from the centre of the vortices, each vortex array applies a stronger polymeric force against the closer of the two surfaces. Thus, the majority of the polymeric contribution to the swimming speed is from the following: (i) the linear viscoelastic response to the local oscillatory shear created by the sheet vortices, interacting with the sheet vortices and pushing on the sheet; and (ii) the linear viscoelastic response to the local oscillatory shear created by the wall vortices, interacting with the wall vortices and pushing on the wall.

For consideration (b), we now have to include the effects of the advection terms $u^{(1)}\partial_x\tau_{xy}^{(1)} + v^{(1)}\partial_y\tau_{xy}^{(1)}$ in Eq. (3.13c), in addition to the rotational term $\Omega_{xy}^{(1)}(\tau_{xx}^{(1)} - \tau_{yy}^{(1)})$ we considered in Section 2.4. Figure 3.5 shows a schematic of this advection term for the sheet vortices. There is an analogous advection mechanism occurring at the wall with the wall vortices.

Just as with the rotational term, this mechanism can be understood as a three-step process. Again, these are steps are explanatory rather than sequential. Step (i), there is a first-order elastic response (blue dumbbells) to the local oscillatory strain rate $D_{xy}^{(1)}$ created by the vortex array. This can be understood as viscoelastic agents (dumbbells) being sheared, for example, a viscoelastic agent oriented in the y-direction stretched in the x-direction. Step (ii), this elastic response is advected by the vortices, this advection is in addition to the simple linear advection of the relative drift caused by the motion of the wave. This step causes a branch in the process. Either the advection moves the elastic response away from the sheet, as in region A, leading to step (iiia); or toward the sheet, as in region B, leading to step (iiib). Step (iii), the elastic response pushes on the sheet. For (iiia), due to the motion away from the sheet, the polymeric force F_p is decreased. For (iiib), the polymeric force is conversely increased.

Along the centreline of the vortices $D_{xy}^{(1)} = 0$, thus if the sheet coincides with this centreline then these advection terms do not contribute to the swimming speed, as we saw in Chapter 2. However, with the introduction of the wall, the sheet vortices are raised slightly. Therefore, the sheet is slightly below the centreline of the vortices, as shown in Fig. 3.5. In this case, in A, the viscoelastic agents 'remember' travelling through a region, where $D_{xy}^{(1)}$ is positive. In B, the viscoelastic agents remember travelling through a region where $D_{xy}^{(1)}$ is negative. Thus in A, the advection term results in a decrease in positive shear and in B the advection term results in an increase in negative shear. Both of these correspond to a net polymeric force F_p in the positive x-direction. In order to be force free, the sheet must swim more quickly in this direction, resulting in a decrease in the swimming speed.

At the wall, the vorticity term in Eq. (3.13c) speeds the sheet up. This is because viscoelastic agents that 'remember' travelling through regions of positive (negative) $D_{xx}^{(1)}$ are now rotated clockwise (anticlockwise), resulting in a positive $\tau_{xy}^{(2)}$. However, the wall is above the wall vortices, so the advection term does not change sign. This is because, above the vortex array, viscoelastic agents in A (B) 'remember' travelling through a region of negative (positive) $D_{xy}^{(1)}$ and are moved towards (away from) the wall. Thus, the advection term at wall also slows the sheet down. At both the sheet and the wall, the magnitude of the vorticity term is larger than the magnitude of the advection term. Therefore, in total, viscoelastic agents at the sheet slow the sheet down and viscoelastic agents at the wall speed the sheet up. Just as with the Newtonian swimming speed, the magnitude of the polymeric contribution to the speed by the sheet vortices is greater than the magnitude of the polymeric contribution to the speed by the wall vortices. Therefore, the slowing down of the sheet in a viscoelastic fluid is caused by the interaction of the sheet vortices with the viscoelastic agents.

Note that although the contributions to the swimming speed from the sheet and wall vortices are independent, they do not factorise, as in Eq. (3.2), independently. It is only the combination of the contributions that factorise.

To summarize, at small amplitudes the velocity field surrounding Taylor's sheet next to a wall can be decomposed into an array of sheet vortices and an array of wall vortices. The model organism swims as a result of the sheet vortices pushing on the sheet. These sheet vortices are faster than the corresponding vortices in the absence of the wall, resulting in faster swimming speeds. In a viscoelastic fluid, it is predominately the interaction of the sheet vortices with the viscoelastic agents that slow the sheet down. This is the same mechanism as for swimming in the bulk of the fluid. There is a linear viscoelastic response to the local oscillatory shear created by the sheet vortices. This interacts with the sheet vortices, and results in a net polymeric force applied to the sheet. Due to the topology of the vortex array, this force opposes the direction of swimming and the sheet must swim more slowly in order to be force-free. Thus, the swimming of Taylor's waving sheet next to a wall can be understood as swimming in the bulk of the fluid with faster sheet vortices.

Now, we turn to the case of finite-amplitude swimming. As shown in Fig. 3.3, at $bk = 0.5$ the swimming speed deviates significantly from the small amplitude prediction of Eq. (3.2). Most notably, the effects of the wall and the viscoelasticity no longer factorise. In the majority of cases, the trend of the velocity decreasing with the Deborah number persists. However, the plateau De value of the swimming speed U_∞ is larger than the asymptotic prediction of Eq. (3.2), $U_\infty > (1-\beta)U_N$, and increases as the boundary is brought closer to the swimmer. Moreover, in some cases the swimming speed no longer decreases monotonically and can even increase to swimming speeds greater than the Newtonian value. Interestingly, this effect is more pronounced at larger β, which corresponds to more dilute solutions, just as with the monotonicity of swimming speed in the bulk of the fluid at large wave amplitudes found in Chapter 2.

To understand this behaviour, we use similar plots as in the previous chapter for the analysis of the swimming in the bulk. We plot the spatial distribution of the

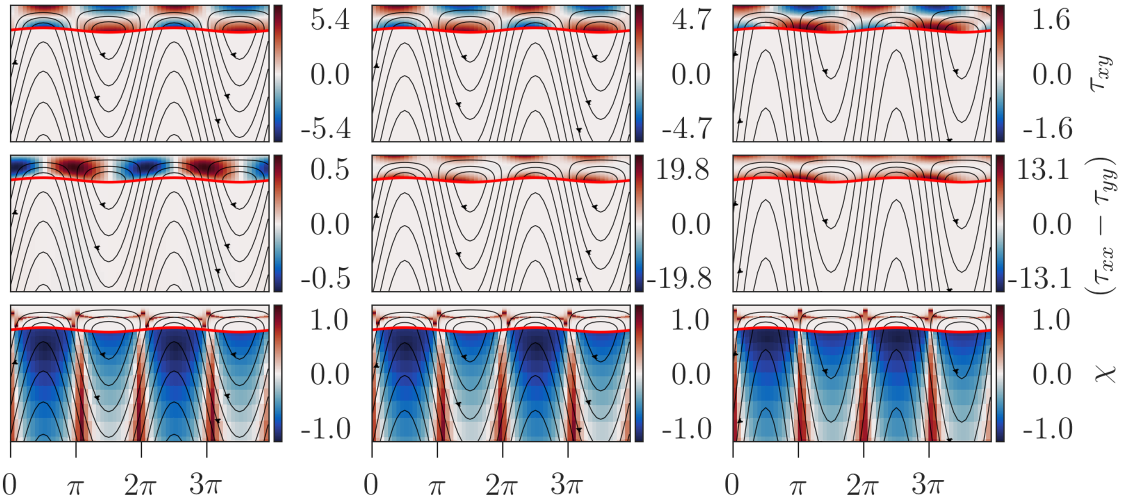

Figure 3.6 The polymeric stress, $\boldsymbol{\tau}$ surrounding a sine-waving sheet with amplitude $bk = 0.01$ near a wall a distance $h_{+}k = 0.11$ above it in an Oldroyd-B fluid with $\beta = 0.5$ and $\mathrm{De} = 0.0$ (left), $\mathrm{De} = 0.5$ (middle) and $\mathrm{De} = 3.2$ (right). The wall below the sheet is at $h_{-}k = 13.0$ which is far enough away to have no effect, however, the fluid domain is only shown until $ky = -0.5$. The swimming speed of the sheet in each situation is $U = U_N = 0.0242c$ (left), $U = 0.905U_N$ (middle), $U = 0.559U_N$ (right).

elastic stresses in he fluid along with the flow type parameter $\chi = \frac{|\mathbf{D}|-|\boldsymbol{\Omega}|}{|\mathbf{D}|+|\boldsymbol{\Omega}|}$ [81]. Due to the invariants of the velocity gradient tensor, $\chi = 1$ corresponds to purely extensional flow, $\chi = 0$ – to shear flow, and $\chi = -1$ – to purely rotation flow. Recall that the flow type parameter does not measure the magnitude of the flow, only its topology.

Figure 3.6 shows these plots at small amplitude, $bk = 0.01$ at $hk = 0.11$, for comparison with the larger-amplitude case. As in the absence of the wall, at these small amplitudes, the topology of the flow field is unaffected by the Deborah number. The xy-component of the polymeric stress simply drifts downstream, as we found in Chapter 2 when swimming in the bulk of an Oldroyd-B fluid. However, there are regions of large normal stresses $\tau_{xx} - \tau_{yy}$ in the regions of pure extensional flow near the sheet and the wall. These regions are not present in the bulk of the fluid at $bk = 0.01$, see Fig. 2.4.

To begin investigating the moderate-amplitude mechanism, we consider the case of a moderate viscosity ratio and a moderate distance to the wall, that is $\beta = 0.5$ and $h_{+}k = 1.2$. At these parameters, the scaled swimming speed has qualitatively similar behaviour as the small-amplitude case, but with larger scaled swimming speeds, see Fig. 3.3. In Fig. 3.7, we plot the same polymeric stress components

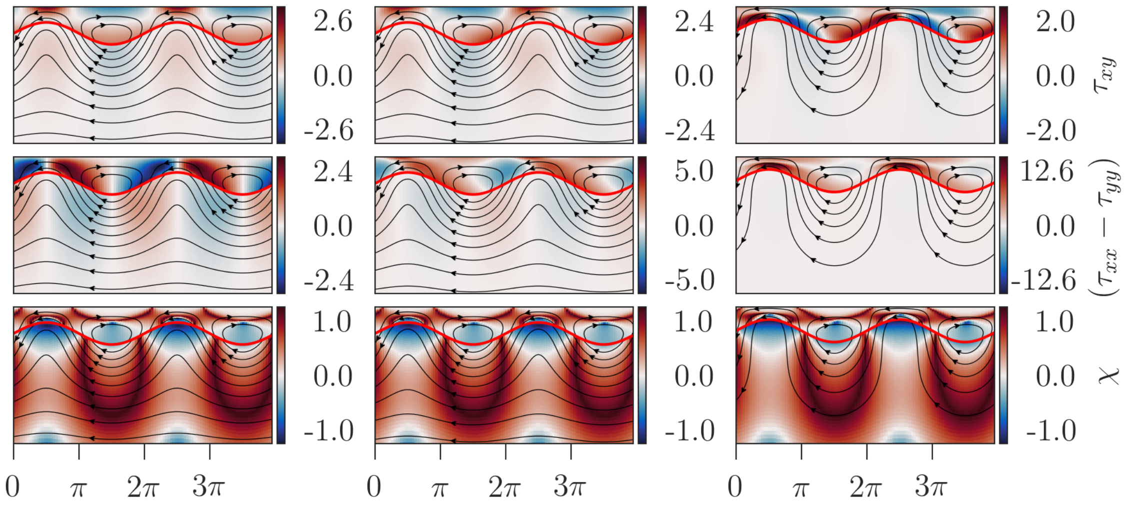

Figure 3.7 The polymeric stress, $\boldsymbol{\tau}$ surrounding a sine-waving sheet with amplitude $bk = 0.5$ near a wall a distance $h_+k = 1.2$ above it in an Oldroyd-B fluid with $\beta = 0.5$ and De $= 0.0$ (left), De $= 0.5$ (middle) and De $= 3.2$ (right). The wall below the sheet is at $h_-k = 13.0$ which is far enough away to have no effect, however, the fluid domain is only shown until $ky = -5$. The swimming speed of the sheet in each situation is $U = U_N = 0.362c$ (left), $U = 0.959U_N$ (middle), $U = 0.854U_N$ (right).

as in Fig. 3.6 for this finite-amplitude case. Similarly, we observe formation of lines of strong extensional flow that generate large normal stresses $\tau_{xx} - \tau_{yy}$. The topology of the flow is also not affected by the Deborah number. The main difference between this case and the small-amplitude case is the fact that the shear stress τ_{xy} is not simply advected downstream as De increases. Instead, there is a more complicated non-linear viscoelastic response. In contrast to swimming in the bulk, this non-linear viscoelastic response is present even at small Deborah numbers.

At the small Deborah number of De $= 0.5$, extra positive (red) τ_{xy} is advected from the wall to the sheet, increasing the sheet's speed. We believe this is what causes the higher scaled swimming speeds at smaller h_+k. This only happens in the vortices around the peaks of the sheet, which are closer to the wall. At the larger Deborah number of De $= 3.2$, in addition to a region with extra positive τ_{xy}, there is a region with extra negative τ_{xy} which pushes the sheet against the direction of swimming, in competition with the positive region.

Now, we turn to the case of non-monotonic behaviour of the swimming speed with the Deborah number. In Fig. 3.8, we compare the stress distributions for $\beta = 0.5$ and $\beta = 0.9$ for $hk = 1.05$ and De $= 2.7$. For $\beta = 0.5$ these values approximately

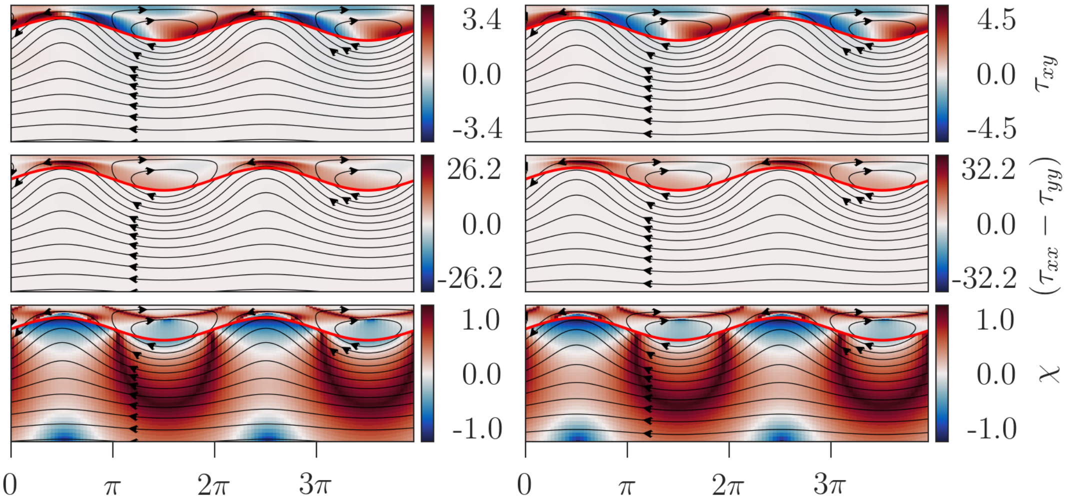

Figure 3.8 A comparison between the stress distributions around a sheet with the amplitude $bk = 0.5$ at a distance $h_+k = 1.05$ from the upper wall with De $= 2.7$: $\beta = 0.5$ (left) and $\beta = 0.9$ (right). The wall below the sheet is at $h_-k = 13.0$ which is far enough away to have no effect, however, the fluid domain is only shown until $ky = -5$. The swimming speed in each case is $U = 0.992U_N$ (left) and $U = 1.020U_N$ (right) with $U_N = 0.440c$.

correspond to the local maximum of the swimming speed, although its value is still smaller than the Newtonian one, while at these parameters the case with $\beta = 0.9$ exhibits swimming speeds larger than U_N, see Fig. 3.3. We note that now both the trough and crest vortices are equally close to the wall, somewhat in contrast to Fig. 3.7. This behaviour is also observed in the Newtonian case De $= 0$, not shown. However, in Fig. 3.8 there are no significant differences between the stress distributions for $\beta = 0.5$ and $\beta = 0.9$ cases besides the numerical values of the stresses, and we conclude that whether the swimming speed is larger or smaller than its Newtonian counterpart is determined by a numerical competition between the wall and sheet stresses that cannot be deduced from hand-waving arguments.

This mechanism could be responsible for the enhanced swimming of the cylindrical sheet in a Boger fluid, observed by Dasgupta et al. [21]. Recall that they suspended a cylindrical sheet of radius $R_1 \approx 5.7\,\text{cm}$ into a tank of radius $R_2 \approx 10.15\,\text{cm}$. They deformed by sheet by stetching it into an ellipse with major and minor semiaxes of $a_2 = 6.8\,\text{cm}$ and $a_1 = 4.6\,\text{cm}$, respectively. We can estimate the parameters for comparison to our calculations with the following

$$\begin{aligned} k &= 2/R_1, \\ b &= (a_2 - a_1)/2, \\ h &= R_2 - R_1. \end{aligned}$$

This gives $bk \approx 0.4$ and $hk \approx 1.5$. Also, for their Boger fluid $\beta \approx 0.7$ and $\mathrm{De} \approx 0.4$–0.8 [21]. This set of parameters does not result in enhanced swimming speeds for our numerical calcualtions of the infinite sheet. However, there are some differences between the cylindrical sheet and the infinite sheet. Firstly, the cylindrical sheet is not propagating a sine wave, but instead an 'ellipitcal wave'. Secondly, the cylindrical sheet is confinining itself on the inside, with $h_i k \approx 2R_1(2/R_1) = 4$ for this boundary. Further investigation is required to determine if the enhanced propulsion is caused by the same mechanism for the cylindrical sheet and for the infinite sheet.

3.5 Conclusion

We have provided a mechanistic explanation for the small wave-amplitude swimming speed of a Taylor sheet derived by Elfring and Lauga [75], and explain why the effects of fluid's viscoelasticity and the presence of a solid boundary decouple. When swimming next to a wall in both a Newtonian and viscoelastic fluid, the vortex array, created by the motion of the sheet, is faster than swimming in the bulk and this leads to a speed increase for the swimmer. Just as in the bulk of a viscoelastic fluid, the swimmer can be viewed as a oscillatory shear probe. The elastic response to this oscillatory shear probe is responsible for the slow down of the sheet. The mechanism responsible for the slow down is more complicated than in the case of swimming next to the wall, as now we must account for advection as well as rotation effects, but is broadly the same mechanism. Thus, when swimming next to a wall in a viscoelastic fluid, the sheet can be understood by considering how it swims in the bulk of a viscoelastic fluid, but with faster sheet vortices.

We also adapted our numerical solver to allows us to study finite-amplitude sheets close to and away from solid walls. We observed that at moderate amplitudes the swimming speed is no longer a monotonic function of the Deborah number, and can even become larger than the corresponding Newtonian value. This is similar to the behaviour we observed for large amplitude swimmers far from a wall. Interestingly, this effect seems to be the stronger, the more dilute the viscoelastic solution is (large values of β).

This result suggests that small amounts of polymer, either excreted or naturally present in the solution, can aid propulsion next to solid boundaries, although the speed increase reported in this work is minute. Our numerical data is not sufficient to determine whether this increase would eventually lead to swimming speeds larger than the Newtonian values for all values of β, at what values of De this can be achieved, and how significant this speed up might be. Further study is required to address these questions.

Chapter 4

Swimming in the depletion region of a viscoelastic fluid

4.1 Introduction

In Chapters 2 and 3, we investigated the effects of viscoelasticity on microswimming in both open and confined geometries, using the Oldroyd-B model. We developed a physical mechanism to explain the slowing down of the sheet as the Deborah number increases. Shen and Arratia's [20] results show that these Oldroyd-B calculations can qualitatively predict the behaviour of the nematode *C. elegans* in viscoelastic fluids. We suggested that our physical mechanism would apply in such circumstances.

However, the Oldroyd-B model is a continuum model, which assumes that the viscoelastic agents in the fluid behave as though they are near their ‘at-rest’ configurations. While these assumptions were not too problematic for reasonably large microswimmers, such as *C. elegans*, we now consider far smaller microorganisms. Crucially, we argue that for smaller microswimmers, especially those with flagella, call into question the validity of the Oldroyd-B model. This is for the following reasons: (i) the effects of the changing conformations of the viscoelastic agents become important; and (ii) it is doubtful that polymer solutions behave as a continuum on these smaller length scales.

Let us consider performing the same experiments as Shen and Arratia [20] performed with nematodes; but using spermatozoa instead. Both of these organisms are planar-wave swimmers, which create vortices in the surrounding fluid. Provided the surrounding fluid is adequately described by the Oldroyd-B equations, we would expect the mechanism described in Chapter 2 to occur, slowing down the spermatozoa. However, spermatozoa propagate waves at a much higher rate than nematodes. As a result, there are much larger deformations of the viscoelastic agents in the fluid around a spermatozoon than around a nematode.

To make things more concrete, we can use the Deborah number De of the problem to estimate the extent of these deformations. That is to say that deformations will be large for larger Deborah numbers, and small for smaller Deborah numbers. The carboxymethyl cellulose solutions used by Shen and Arratia [20] have relaxation times in the range $\lambda \approx 0.4$–$5.6\,\mathrm{s}$. *C. elegans* propagates waves at a frequency of $f \approx 2\,\mathrm{Hz}$, which results in reasonably small Deborah numbers in the range of $\mathrm{De} = \lambda f \approx 0.8$–$11.2$. In contrast, the waves of the spermatozoa of the sea urchin L. pictus have a frequency of $f \approx 30\,\mathrm{Hz}$ [41], leading to much larger Deborah numbers in the range of $\mathrm{De} \approx 12$–168. Thus, the deformations in the fluid surrounding a spermatozoon are much larger than those surrounding a nematode. Correspondingly, we can suppose that the Oldroyd-B equations will not model the fluid around the spermatozoon as well as it models that around the nematode.

The difference between nematodes and spermatozoa is exacerbated if we consider the size of the organisms. *C. elegans* worms have a diameter of $\approx 80\,\mu\mathrm{m}$, which is much larger than the typical radius of gyration of a polymer. Therefore, we can reasonably view the fluid as a continuum. In contrast, the flagellum of a spermatozoon has a diameter of $\approx 200\,\mathrm{nm}$ [14]. This is comparable in size to the radius of gyration of high-molecular-weight polymer coils, such as 10 MDa polyacrylamide (PAAm) in dilute solution, which has a radius of gyration of $\approx 200\,\mathrm{nm}$[90] or bovine/porcine submaxillary mucin in water, which have radii of gyrations of $\approx 250\,\mathrm{nm}$[91]. As such, for a flagellum, we cannot expect continuum models of the fluid to be valid, much less the Oldroyd-B equations.

As cross-sections of the flagellum move through the fluid, they hydrodynamically collide with the polymer coils. These cross-sections are of similar size to the polymer coils and are moving at very high speeds. We can estimate the speed V of the cross-sections as $V \approx 4bf$, where b is the amplitude of the wave propagated by the spermatozoa. For the spermatozoa of *L. pictus*, we have $b \approx 5\,\mu\mathrm{m}$ [41]; and so $V \approx 600\,\mu\mathrm{m\,s^{-1}}$. The time it takes for the cross-sections to move by the radius of gyration of the PAAm polymer coils is $R_g/V \approx 0.3\,\mathrm{ms}$. This is much less than the Zimm relaxation time λ of these coils, which is given by

$\lambda = \eta_s R_g^3/(k_B T) \approx 1.9\,\mathrm{ms}$, where $k_B T$ is the thermal energy. From this back of the envelope calculation we can expect that polymer coils in the vicinity of the flagellum will undergo very violent deformations, possibly even breaking. We cannot expect the fluid to be described by the Oldroyd-B equations in such situations.

Similar arguments have been made by Martinez et al. [19], regarding their experiments of *E. coli*, a flagellated microswimmer, swimming in a polyvinylpyrrolidone (PVP) solution. As discussed in Section 1.3, Martinez et al. found that, for low-molecular-weight PVP, *E. coli* with fixed kinematics have the same swimming speed as they would in a Newtonian fluid. At higher molecular weights, where viscoelasticity becomes important, they found that *E. coli* with fixed kinematics swim faster than they would in a Newtonian fluid.

To explain this, Martinez et al. developed a novel mechanism to account for the changing conformation of the polymers, using arguments similar to those we have made above. Crucially, they noted that the flagella bundle of an *E. coli* bacterium has a diameter of ≈20 nm. This is roughly the same size as a PVP coil in the high molecular-weight solution, which has a radius of gyration, R_g, of ≈60 nm. They also noted that the flagella of an *E. coli* bacterium moves so quickly that the time it takes for the flagella bundle to move a distance R_g is $\approx 0.3\lambda$, where λ is the Zimm relaxation time of the polymer coil.

Martinez et al. supposed that polymer coils in the vicinity of the flagella bundle are "strongly stretched as quasi-stationary objects". They claimed that flagella revisit locations in the fluid so quickly that the stretched polymers never have a chance to relax back to their at-rest configurations. This is reminiscent of the coil-stretch transition [92] of polymer coils in strong constant shear flows. After spending long times in such flows, polymers transition from the 'coil' state to the 'stretch' state. In the stretch state, polymers are close to being maximally extended. The energy barrier required to transition back to the normal coil state is extremely large, due to hydrodynamic interactions with the solvent. This leads to much larger relaxation times than the Zimm relaxation times for a polymer coil in its at-rest configuration, considered above. As such, we can expect Martinez et al.'s quasi-stationary objects to have longer relaxation times than in their at-rest configurations.

Because of this mechanism, they hypothesised that the flagella travel through a fluid effectively depleted of viscoelastic agents. In this depletion region, the polymers in the fluid do not contribute to the viscosity. In contrast, the cell body rotates much more slowly than the flagella. Therefore, polymers near the cell body are not sufficiently stretched to cease contributing to the fluid viscosity. Using a modified version of Purcell's model [9] for an *E. coli* bacterium swimming in a Newtonian fluid, Martinez et al. were able to correctly reproduce their observed data without any fitting parameters. To do so, they made the following modification: the flagella 'see' a fluid with a viscosity equal to that of the solvent; whereas, the cell body sees a fluid with a viscosity equal to the zero-shear-rate viscosity of the polymer solution.

Martinez et al.'s 'semi-continuum' model for an *E. coli* bacterium in a polymer solution uses a very simple approximation to account for the effects of the conformational changes of the viscoelastic agents. That is, deformations of the viscoelastic agents stop them behaving viscoelastically and contributing to the viscosity of the fluid. Martinez et al. were able to explain their data by only considering the difference in the viscosities between the depleted and undepleted regions. They did not consider the viscoelasticity in the undepleted region of the fluid.

In this chapter, we consider a similar semi-continuum model for Taylor's waving sheet. Like Martinez et al., we investigate how the viscosity difference between the two regions affects the swimming of the sheet. However, we also consider the viscoelastic behaviour in the undepleted region, using the Oldroyd-B model for the fluid in this region. In the depleted region, we assume that the fluid is Newtonian as there are no viscoelastic agents.

We now mathematically define the problem in hand.

4.1.1 The model

We use Taylor's sheet to investigate the swimming of flagellated microorganisms in viscoelastic fluids, where the mechanism describe in Section 4.1 is present. We assume that the sheet is sufficiently 'thin' and moving quickly enough that any polymer coils caught in its path are completely stretched-out. That is, they do not contribute anything to the viscosity of the solution and they do not contribute to the polymeric stress. We also assume that the relaxation time of these fully stretched-out polymer coils is so long compared to the time period of the sheet's motion that, on time scales of the fluids motion, there is a fixed region surrounding

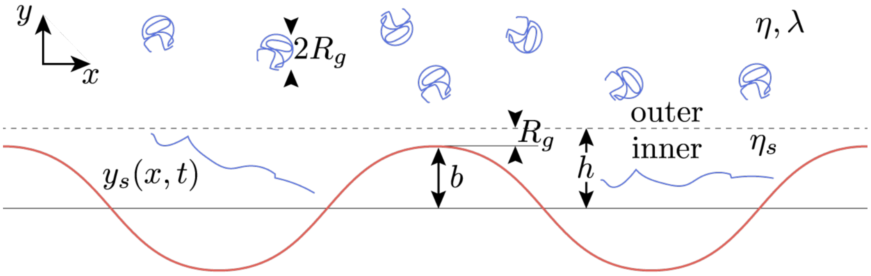

Figure 4.1 A schematic of a swimming sheet with a depletion region of thickness h. Polymer coils in the inner fluid are maximally stretched and the viscosity in this region is just the viscosity of the solvent, η_s. The outer fluid contains normal polymer coils, thus we have the usual total viscosity $\eta = \eta_s + \eta_p$, where η_p is the contribution to the viscosity by the polymer coils. The polymer coils in the outer fluid have a viscoelastic response with a longest relaxation time λ.

the centre of the sheet of thickness $2h = 2(b + R_g)$, which is entirely depleted of viscoelastic agents. See Fig. 4.1.

As in Section 1.1.3, the sheet is propagating a wave with a waveform $f(\zeta)$ and wave speed c, such that it traces out the shape $y_s(x,t) = f(k(x - (c - U)t))$ at a time t, where k is the associated wavenumber and U is the swimming speed of the sheet in the negative x-direction.

In the depletion region, the fluid is Newtonian with the viscosity of the solvent, η_s. In the outer fluid, the polymer coils are present and we have the total fluid viscosity, $\eta = \eta_s + \eta_p$. To allow us to distinguish between the effects of viscosity and the effects of this viscosity difference we will consider two scenarios. One where the outer fluid is Newtonian and another where the outer fluid is viscoelastic and governed by the Oldroyd-B equation with a longest relaxation time λ.

To find the swimming speed of the sheet, we first find the velocity field $\boldsymbol{u}_{i,o} = (u_{i,o}, v_{i,o})^T$ in the fluids. Here, and elsewhere in this chapter, the subscripts "i" and "o" correspond to quantities in the inner and outer fluid, respectively.

If the outer fluid is Newtonian, then both velocity fields must satisfy the Stokes equations and we must solve the following

$$-\nabla p_{i,o} + \eta_{i,o}\nabla^2 \boldsymbol{u}_{i,o} = \boldsymbol{0}, \tag{4.1a}$$

$$\nabla \cdot \boldsymbol{u}_{i,o} = 0, \tag{4.1b}$$

where $p_{i,o}$ is the pressure field, and $\eta_{i,o}$ the viscosity in the corresponding fluid.

In the scenario where the outer fluid is viscoelastic, we must solve the Oldroyd-B-Stokes' equations for the outer fluid, while solving the regular Stokes' equations for the inner fluid. Thus, we have

$$-\nabla p_i + \eta_s \nabla^2 \boldsymbol{u}_i = \mathbf{0}, \tag{4.2a}$$

$$-\nabla p_o + \eta_s \nabla^2 \boldsymbol{u}_o + \nabla \cdot \boldsymbol{\tau} = \mathbf{0}, \tag{4.2b}$$

$$\nabla \cdot \boldsymbol{u}_{i,o} = 0, \tag{4.2c}$$

$$\boldsymbol{\tau} + \lambda \overset{\triangledown}{\boldsymbol{\tau}} = 2\eta_p \mathbf{D}_o, \tag{4.2d}$$

$$\tag{4.2e}$$

where η_p is the polymeric viscosity, $\mathbf{D}_{i,o} = (\nabla \boldsymbol{u}_{i,o} + \nabla \boldsymbol{u}_{i,o}^T)/2$ is the strain rate tensor and $\boldsymbol{\tau}$ is the polymeric stress in the outer fluid. Here, the upper-convected derivative is given by

$$\overset{\triangledown}{\boldsymbol{\tau}} = \partial_t \boldsymbol{\tau} + \boldsymbol{u}_o \cdot \nabla \boldsymbol{\tau} - \nabla \boldsymbol{u}_o^T \cdot \boldsymbol{\tau} - \boldsymbol{\tau} \cdot \nabla \boldsymbol{u}_o.$$

In addition to these governing equations, we have the usual no-slip boundary conditions at the sheet given by

$$\boldsymbol{u}_i\big|_{y=y_s} = \boldsymbol{u}_s, \tag{4.3}$$

where $\boldsymbol{u}_s = (u_s, v_s)^T$ is the velocity of the material points of the sheet. We also need boundary conditions at the interface. Firstly, we require that the velocity field is continuous at the interface. Secondly, we require that the interface is in mechanical equilibrium and so, the total force applied to the interface by the fluid regions must vanish. Thus, we have

$$\boldsymbol{u}_i\big|_{y=h} = \boldsymbol{u}_o\big|_{y=h}, \tag{4.4a}$$

$$\mathbf{\Sigma}_i \cdot \boldsymbol{n}_i\big|_{y=h} + \mathbf{\Sigma}_o \cdot \boldsymbol{n}_o\big|_{y=h} = \mathbf{0}, \tag{4.4b}$$

where $\boldsymbol{n}_{i,o}$ are the inward-pointing normals of the interface and $\mathbf{\Sigma}_{i,o}$ is the total stress in each fluid. In the inner fluid or a Newtonian outer fluid, we have

$$\mathbf{\Sigma}_{i,o} = -p_{i,o} + 2\eta_{i,o} \mathbf{D}_{i,o}; \tag{4.5}$$

whereas, for an Oldroyd-B outer fluid, we have

$$\mathbf{\Sigma}_o = -p_o + 2\eta_s \mathbf{D}_o + \boldsymbol{\tau}. \tag{4.6}$$

As $\boldsymbol{n}_i = -\boldsymbol{n}_o$, the mechanical equilibrium condition can be thought of as 'force continuity' if we use the same upward normal for the interface $\boldsymbol{n} = \boldsymbol{n}_o$.

With these boundary conditions, we are ignoring any mixing between the regions that occur due to the motion of the fluid. That is, we are assuming that the mechanism responsible for the creation of the depletion region is sufficiently fast that we can ignore the mixing over the typical time scales of the fluid flow. Man and Lauga [93] have looked at a similar Newtonian two-fluid problem. They explicitly forbade mixing of the fluids, by requiring that there is no y-velocity at the interface, i.e. $v_i|_{y=h} = v_o|_{y=h} = 0$, instead of requiring that there is no y-force acting the interface, as we have here. We have been somewhat vague about the mechanism responsible for creating the depletion region and, without a detailed model of this, we cannot decide between these two sets of boundary conditions on physical grounds. However, we note that if $h = 0$, then the vanishing y-velocity is incompatible with the kinematics of the sheet. With our choice of boundary conditions, setting $h = 0$ recovers boundary conditions for swimming solely in the outer fluid. For this reason, we prefer the boundary conditions listed above.

We use two techniques to solve this problem for a sine-waving sheet. First, we find the swimming speed in the small-amplitude limit, before using our numerical solver to find the swimming speed for finite-amplitude waves. We then use this analysis to develop a mechanistic understanding of the behaviour of the swimming speed as function of Deborah number. We show that the behaviour of the sheet in this situation can be understood by considering the outer fluid as a 'soft wall'. We then show that viscoelasticity in the outer fluid turns off this soft wall mechanism and introduces a new mechanism, similar to that developed in Chapter 2.

In Section 4.2, we solve the problem in the small-amplitude limit. We then show our numerical solver can be adapted for this problem in Section 4.3. In Section 4.4, we describe the results found from the previous two sections. Finally, we discuss our findings in Section 4.5.

4.2 Small-amplitude analysis

In this section, we solve the depletion region problem with both a Newtonian and viscoelastic outer fluid for a small-amplitude sine-waving sheet. We follow a similar strategy as in the previous chapters, where we perform Taylor expansions of the hydrodynamic fields. There is an up-down symmetry to the problem, so we only need to consider the fluid above the sheet. We consider the outer fluid being Newtonian and viscoelastic separately.

4.2.1 Newtonian outer fluid

Here, we solve Eq. (4.1), subject to the boundary conditions Eqs. (4.3) and (4.4) for a sine-waving sheet with $f(\zeta) = b\sin(\zeta)$.

We will begin by performing a transformation to starred quantities, which both dedimensionalises the problem and removes any explicit time dependence, given by

$$\begin{gathered} x^* = k(x - ct),\ y^* = ky,\ y_s^* = ky_s,\ h^* = hk, \\ U^* = \frac{U}{c},\ u_{i,o}^* = 1 + \frac{u_{i,o}}{c},\ v_{i,o}^* = \frac{v_{i,o}}{c}, \\ p_{i,o}^* = \frac{p_{i,o}}{\eta_{i,o}ck},\ \boldsymbol{\Sigma}_{i,o}^* = \frac{\boldsymbol{\Sigma}_{i,o}}{\eta_{i,o}ck}. \end{gathered} \tag{4.7}$$

Recall that, in these coordinates the shape of the sheet is given by $y_s^*(x^*) = \epsilon\sin(x^*) + \mathcal{O}(\epsilon^3)$, where $\epsilon = bk$ is the dimensionless wave amplitude. From now on we will drop the *s for clarity.

We expand the hydrodynamic fields, $\boldsymbol{\Sigma}_{i,o}$, $p_{i,o}$ and $\boldsymbol{u}_{i,o}$ into Taylor series about $\epsilon = 0$. For example, the pressure field in the outer fluid is given by

$$p_{i,o} = \sum_{n=0}^{\infty} p_{i,o}^{(n)}\epsilon^n. \tag{4.8}$$

where $p_{i,o}^{(n)}$ is the 'nth-order' contribution to the pressure field.

The kinematics of the sheet have not changed from the original Taylor's waving sheet problem, so in our coordinates, which are co-moving with the wave, the velocity of the material points of the sheet are given by

$$u_s = -1 + \mathcal{O}(\epsilon^2), \tag{4.9a}$$

$$v_s = -\epsilon\cos(x) + \mathcal{O}(\epsilon^2). \tag{4.9b}$$

Given the velocity field $\boldsymbol{u}_i$, the swimming speed of the sheet is, to the second order, given by

$$U = -\langle y_s \, \partial_y u_i^{(1)}\Big|_{y=0}\rangle \epsilon - \langle u_i^{(2)}\Big|_{y=0}\rangle \epsilon^2, \tag{4.10}$$

where $\langle ... \rangle$ are x-averages.

We now substitute the Taylor expanded hydrodynamic fields into Eq. (4.1) and the boundary conditions. We consider each power of ϵ separately. For the zeroth order we have

$$\begin{aligned}
-\nabla p_{i,o}^{(0)} + \beta_{i,o} \nabla^2 \boldsymbol{u}_{i,o}^{(0)} &= \boldsymbol{0}, \\
\nabla \cdot \boldsymbol{u}_{i,o}^{(0)} &= 0, \\
\boldsymbol{u}_i^{(0)}\Big|_{y=0} &= -\boldsymbol{e}_x, \\
\boldsymbol{u}_i^{(0)}\Big|_{y=h} &= \boldsymbol{u}_o^{(0)}\Big|_{y=h}, \\
\beta \left[\partial_y u_i^{(0)} + \partial_x v_i^{(0)}\right]_{y=h} &= \left[\partial_y u_o^{(0)} + \partial_x v_o^{(0)}\right]_{y=h}, \\
\beta \left[-p_i^{(0)} + 2\partial_y v_i^{(0)}\right]_{y=h} &= \left[-p_o^{(0)} + 2\partial_y v_o^{(0)}\right]_{y=h},
\end{aligned}$$

where $\beta_{i,o} = \eta_{i,o}/\eta$ such that $\beta_i = \beta = \eta_s/\eta$ and $\beta_o = 1$. This has the trivial solution $p_{i,o}^{(0)} = 0$ and $\boldsymbol{u}_{i,o}^{(0)} = -\boldsymbol{e}_x$. The zeroth-order flow field is simply an artefact of our choice of reference frame and has no physical relevance in the Newtonian case. However, when we consider the effects of viscoelasticity, this solution will be important.

To the first order, we have the following set of equations to solve

$$-\nabla p_{i,o}^{(1)} + \beta_{i,o} \nabla^2 \boldsymbol{u}_{i,o}^{(1)} = \boldsymbol{0}, \tag{4.11a}$$

$$\nabla \cdot \boldsymbol{u}_{i,o}^{(1)} = 0, \tag{4.11b}$$

$$\boldsymbol{u}_i^{(1)}\Big|_{y=0} = -\cos(x)\boldsymbol{e}_y, \tag{4.11c}$$

$$\boldsymbol{u}_i^{(1)}\Big|_{y=h} = \boldsymbol{u}_o^{(1)}\Big|_{y=h}, \tag{4.11d}$$

$$\beta \left[\partial_y u_i^{(1)} + \partial_x v_i^{(1)}\right]_{y=h} = \left[\partial_y u_o^{(1)} + \partial_x v_o^{(1)}\right]_{y=h}, \tag{4.11e}$$

$$\beta \left[-p_i^{(1)} + 2\partial_y v_i^{(1)}\right]_{y=h} = \left[-p_o^{(1)} + 2\partial_y v_o^{(1)}\right]_{y=h}. \tag{4.11f}$$

To solve this set of equations, we introduce stream-functions $\psi_{i,o}$ in each fluid domain. These stream-functions are defined via their relationship to their respective velocity fields, $u_{i,o}^{(1)} = \partial_y \psi_{i,o}$ and $v_{i,o}^{(1)} = -\partial_x \psi_{i,o}$. This relationship is chosen so that Eq. (4.11b) is automatically satisfied for any choice of $\psi_{i,o}$. In

Stokes' flow, these stream-functions both satisfy the biharmonic equation

$$\nabla^4 \psi_{i,o} = 0, \tag{4.12}$$

which has the general periodic solution

$$\psi_{i,o} = (A_{i,o} y + B_{i,o}) \sin(x) e^{-y} + (C_{i,o} y + D_{i,o}) \sin(x) e^{y}. \tag{4.13}$$

Here, we have ignored any terms proportional to $\cos(x)$ as they are incompatible with Eq. (4.11c). The velocity field must vanish as $y \to \infty$. So, above the sheet, we must have $C_o = D_o = 0$. Substituting $\psi_{i,o}$ into Eq. (4.11a) and solving for the associated pressure fields $p^{(1)}_{i,o}$ yields

$$p^{(1)}_i = -2(A_i e^{-y} + C_i e^{y}) \cos(x), \tag{4.14a}$$

$$p^{(1)}_o = -2A_o e^{-y} \cos(x). \tag{4.14b}$$

Substituting $\psi_{i,o}$ and $p^{(1)}_{i,o}$ into Eqs. (4.11c) to (4.11f) gives a set of linear equations, which govern the remaining constants

$$A_i - B_i + C_i + D_i = 0, \tag{4.15a}$$

$$B_i - D_i = -1, \tag{4.15b}$$

$$(A_i(1-h) - B_i)e^{-h} + (C_i(1+h) - D_i)e^{h} = (A_o(1-h) - B_o)e^{-h}, \tag{4.15c}$$

$$(A_i h + B_i)e^{-h} + (C_i h + D_i)e^{h} = (A_o h + B_o)e^{-h}, \tag{4.15d}$$

$$\beta\left[(A_i(h-1) - B_i)e^{-h} + (C_i(1+h) - D_i)e^{h}\right] = (A_o(h-1) - B_o)e^{-h}, \tag{4.15e}$$

$$\beta[(A_i h + B_i)e^{-h} - (C_i h + D_i)e^{h}] = (A_o h + B_o)e^{-h}. \tag{4.15f}$$

To solve Eq. (4.15), we first combine Eqs. (4.15c) to (4.15f) to remove terms proportional to e^h, yielding

$$\begin{aligned} 2\beta(A_i(1-h) + B_i)e^{-h} &= (1+\beta)(A_o(1-h) + B_o)e^{-h}, \\ 2\beta(A_i h + B_i)e^{-h} &= (1+\beta)(A_o h + B_o)e^{-h}, \end{aligned}$$

which has the solution

$$A_o = \frac{2\beta}{1+\beta} A_i, \ B_o = \frac{2\beta}{1+\beta} B_i. \tag{4.16}$$

Next, we substitute Eq. (4.16) into Eq. (4.15), giving

$$A_i - B_i + C_i + D_i = 0, \tag{4.17a}$$

$$B_i + D_i = -1, \tag{4.17b}$$

$$(A_i(1-h) - B_i)\alpha_0 e^{-h} + (C_i(1+h) + D_i)e^h = 0, \tag{4.17c}$$

$$(A_i h + B_i)\alpha_0 e^{-h} + (C_i h + D_i)e^h = 0. \tag{4.17d}$$

Here, $\alpha_0 = (1-\beta)/(1+\beta) = (\eta - \eta_s)/(\eta + \eta_s)$ is the dimensionless viscosity difference between the fluids.

The solution to Eq. (4.17) is given by

$$A_i = \frac{q_{\alpha_0}(h)^2 + p_{\alpha_0}(h)q_{\alpha_0}(h) + \alpha_0 h}{2(q_{\alpha_0}(h)^2 - \alpha_0 h^2)}, \tag{4.18a}$$

$$B_i = \frac{q_{\alpha_0}(h)^2 + p_{\alpha_0}(h)q_{\alpha_0}(h) + \alpha_0 h - \alpha_0 h^2}{2(q_{\alpha_0}(h)^2 - \alpha_0 h^2)}, \tag{4.18b}$$

$$C_i = \frac{-q_{\alpha_0}(h)^2 + p_{\alpha_0}(h)q_{\alpha_0}(h) + \alpha_0 h}{2(q_{\alpha_0}(h)^2 - \alpha_0 h^2)}, \tag{4.18c}$$

$$D_i = \frac{q_{\alpha_0}(h)^2 - p_{\alpha_0}(h)q_{\alpha_0}(h) - \alpha_0 h - \alpha_0 h^2}{2(q_{\alpha_0}(h)^2 - \alpha_0 h^2)}. \tag{4.18d}$$

Here, $q_{\alpha_0}(h) = (e^h - \alpha_0 e^{-h})/2$ and $p_{\alpha_0}(h) = (e^h + \alpha_0 e^{-h})/2$.

Before using Eq. (4.18) to find the first term of Eq. (4.10), we will show that the second term vanishes. As always, the x-average in the second term commutes with the y-substitution. Thus, we only have to find the x-average of $u_{i,o}^{(2)}$. Taking the x-average of the x-component of the second-order terms of Eq. (4.1a), we have

$$\partial_{yy}\langle u_{i,o}^{(2)}\rangle = 0,$$

which has the trivial solutions

$$\langle u_{i,o}^{(2)}\rangle = I_{i,o} + J_{i,o}y.$$

Firstly, we know that to the second order, the velocity field far from the sheet must vanish, thus $I_o = J_o = 0$. To find I_i and J_i, we require both velocity and force continuity at the interface, Eq. (4.4), which gives

$$\langle u_i^{(2)}\rangle\Big|_{y=h} = \langle u_o^{(2)}\rangle\Big|_{y=h},$$

$$\beta\,\partial_y\langle u_i^{(2)}\rangle\Big|_{y=h} = \partial_y\langle u_o^{(2)}\rangle\Big|_{y=h}$$

Thus, $I_i = J_i = 0$ and $\langle u_i^{(2)} \rangle \Big|_{y=0} = 0$.

Now, using Eq. (4.18), we find that the first term in Eq. (4.10) and thus the swimming speed itself is given by

$$\begin{aligned} U &= \frac{1}{2}(2A_i - B_i - 2C_i - D_i)\epsilon^2, \\ &= \frac{\epsilon^2}{2}\left(\frac{q_{\alpha_0}(h)^2 + \alpha_0 h^2}{q_{\alpha_0}(h)^2 - \alpha_0 h^2}\right). \end{aligned} \tag{4.19}$$

We now turn to the viscoelastic case.

4.2.2 Oldroyd-B outer fluid

Here, we now consider the effects of viscoelasticity in the outer fluid on the swimming speed of the sheet. We solve Eq. (4.2), subject to the boundary conditions in Eqs. (4.3) and (4.4).

We perform the same transformation to starred quantities as in Eq. (4.7); but in addition we scale $\boldsymbol{\tau}$ by $\eta_p ck$, such that

$$\boldsymbol{\tau}^* = \frac{\boldsymbol{\tau}}{\eta_p ck}.$$

As before, we drop the *s from now on. We Taylor expand our hydrodynamic fields, including $\boldsymbol{\tau}$, around $\epsilon = 0$ as in Eq. (4.8).

It is trivial to show that we get the same zeroth-order solution as we do in the Newtonian case, with $\boldsymbol{\tau}^{(0)} = \mathbf{0}$. Unlike swimming next to a wall or in the bulk of a fluid, the boundary conditions are not the same for Newtonian and viscoelastic fluids. As such, the argument we used in Section 2.2 to show that the first-order velocity for a viscoelastic fluid is the same as for a Newtonian fluid does not work. However, this argument does show that the general solution for the velocity field in the outer fluid must be the same as in the Newtonian case. Consider the first order set of equations we must solve

$$-\nabla p_i^{(1)} + \beta \nabla^2 \boldsymbol{u}_i^{(1)} = \mathbf{0}, \tag{4.20a}$$

$$-\nabla p_o^{(1)} + \beta \nabla^2 \boldsymbol{u}_o^{(1)} + (1-\beta)\nabla \cdot \boldsymbol{\tau} = \mathbf{0}, \tag{4.20b}$$

$$\nabla \cdot \boldsymbol{u}_{i,o}^{(1)} = 0, \tag{4.20c}$$

$$(1 - \mathrm{De}\ \partial_x)\boldsymbol{\tau}^{(1)} = \mathbf{D}^{(1)}, \tag{4.20d}$$

$$\left.\boldsymbol{u}_i^{(1)}\right|_{y=0} = -\cos(x)\boldsymbol{e}_y, \tag{4.20e}$$

$$\left.\boldsymbol{u}_i^{(1)}\right|_{y=h} = \left.\boldsymbol{u}_o^{(1)}\right|_{y=h}, \tag{4.20f}$$

$$\beta \left[\partial_y u_i^{(1)} + \partial_x v_i^{(1)}\right]_{y=h} = \left[\partial_y u_o^{(1)} + \partial_x v_o^{(1)} + \tau_{xy}^{(1)}\right]_{y=h}, \tag{4.20g}$$

$$\beta \left[p_i^{(1)} + 2\partial_y v_i^{(1)}\right]_{y=h} = \left[p_o^{(1)} + 2\partial_y v_o^{(1)} + \tau_{yy}^{(1)}\right]_{y=h}, \tag{4.20h}$$

where $\mathrm{De} = \lambda ck$ and we have used the solution $\boldsymbol{u}_o^{(0)} = -\boldsymbol{e}_x$ in Eq. (4.20d). We begin by introducing stream-functions $\psi_{i,o}$ in both fluids via their relationships to the velocity fields, $u_{i,o}^{(1)} = \partial_y \psi_{i,o}$ and $v_{i,o}^{(1)} = -\partial_x \psi_{i,o}$.

As already argued, the stream-functions have the same general solution as in the Newtonian case. However, unlike in the Newtonian case, we cannot dismiss the 'out-of-phase' components, that is the terms in $\psi_{i,o}$ proportional to $\cos(x)$. The linear viscoelastic response to the fluid flow contains an out-of-phase component in the outer fluid, which must be matched by the Newtonian stress of the inner fluid. This leads to the inclusion of the terms of $\psi_{i,o}$ proportional to $\cos(x)$. Thus, we have

$$\begin{aligned}\psi_{i,o} = (A_{i,o}y + B_{i,o})\sin(x)e^{-y} + (C_{i,o}y + D_{i,o})\sin(x)e^{y} + \\ + (E_{i,o}y + F_{i,o})\cos(x)e^{-y} + (G_{i,o}y + H_{i,o})\cos(x)e^{y}.\end{aligned} \tag{4.21}$$

As before, the first order velocity field far from the sheet must vanish, thus, $C_o = D_o = G_o = H_o = 0$.

We solve Eq. (4.20d) to find the polymeric stress $\boldsymbol{\tau}^{(1)}$ associated with Eq. (4.21), giving

$$\tau_{xx}^{(1)} = -\tau_{yy}^{(1)} = \frac{2}{1+\mathrm{De}^2}\Bigg[\Big((A_o - \mathrm{De}E_o)(y-1) + (B_o - \mathrm{De}F_o)\Big)\cos(x)e^{-y} + \\ + \Big((E_o + \mathrm{De}A_o)(y-1) + (F_o + \mathrm{De}B_o)\Big)\sin(x)e^{-y}\Bigg], \tag{4.22a}$$

$$\tau_{xy}^{(1)} = \frac{2}{1+\mathrm{De}^2}\Bigg[\Big((A_o - \mathrm{De}E_o)(y-1) + (B_o - \mathrm{De}F_o)\Big)\sin(x)e^{-y} + \\ + \Big((E_o + \mathrm{De}A_o)(y-1) + (F_o + \mathrm{De}B_o)\Big)\cos(x)e^{-y}\Bigg]. \tag{4.22b}$$

Using Eqs. (4.20a) and (4.20b), the associated pressure fields are given by

$$p_i^{(1)} = 2E_i\sin(x)e^{-y} + 2G_i\sin(x)e^{y} - 2A_i\cos(x)e^{-y} - 2C_i\cos(x)e^{y}, \tag{4.23a}$$

$$p_o^{(1)} = \frac{-2}{1+\mathrm{De}^2}\Bigg[\Big((1+\beta\mathrm{De}^2)A_o - (1-\beta)\mathrm{De}E_o\Big)\cos(x)e^{-y} + \\ + \Big((1+\beta\mathrm{De}^2)E_o - (1-\beta)\mathrm{De}A_o\Big)\sin(x)e^{-y}\Bigg]. \tag{4.23b}$$

We can write the boundary conditions in Eq. (4.20) in terms of the coefficients in Eq. (4.21) by noting that the in-phase and out-of-phase components of each equation must be satisfied independently. Thus, we have the following 12 equations to solve

$$A_i - B_i + C_i + D_i = 0, \tag{4.24a}$$

$$B_i + D_i = 1, \tag{4.24b}$$

$$-(A_i(h-1) + B_i)e^{-h} + (C_i(h+1) + D_i)e^{h} = -(A_o(h-1) + B_o)e^{-h}, \tag{4.24c}$$

$$(A_ih + B_i)e^{-h} + (C_ih + D_i)e^{h} = (A_oh + B_o)e^{-h}, \tag{4.24d}$$

$$E_i - F_i + G_i + H_i = 0, \tag{4.24e}$$

$$F_i + H_i = 0, \tag{4.24f}$$

$$-(E_i(h-1) + F_i)e^{-h} + (G_i(h+1) + H_i)e^{h} = -(E_o(h-1) + F_o)e^{-h}, \tag{4.24g}$$

$$(E_ih + F_i)e^{-h} + (G_ih + H_i)e^{h} = (E_oh + F_o)e^{-h}, \tag{4.24h}$$

$$\begin{split}\beta \Big[(A_i(h-1)+B_i)e^{-h} + (C_i(h+1)+D_i)e^{h}\Big] = \\ \frac{e^{-h}}{1+\mathrm{De}^2}\Big[(1+\beta\mathrm{De}^2)(A_o(h-1)+B_o) - (1-\beta)\mathrm{De}(E_o(h-1)+F_o)\Big],\end{split} \tag{4.24i}$$

$$\begin{split}\beta \Big[(A_i h+B_i)e^{-h} - (C_i h+D_i)e^{h}\Big] = \\ \frac{e^{-h}}{1+\mathrm{De}^2}\Big[(1+\beta\mathrm{De}^2)(A_o h+B_o) - (1-\beta)\mathrm{De}(E_o h+F_o)\Big],\end{split} \tag{4.24j}$$

$$\begin{split}\beta \Big[(E_i(h-1)+F_i)e^{-h} + (G_i(h+1)+H_i)e^{h}\Big] = \\ \frac{e^{-h}}{1+\mathrm{De}^2}\Big[(1+\beta\mathrm{De}^2)(E_o(h-1)+F_o) + (1-\beta)\mathrm{De}(A_o(h-1)+B_o)\Big],\end{split} \tag{4.24k}$$

$$\begin{split}\beta \Big[(E_i h+F_i)e^{-h} - (G_i h+H_i)e^{h}\Big] = \\ \frac{e^{-h}}{1+\mathrm{De}^2}\Big[-(1+\beta\mathrm{De}^2)(E_o h+F_o) - (1-\beta)\mathrm{De}(A_o h+B_o)\Big].\end{split} \tag{4.24l}$$

To solve Eq. (4.24), we follow the same strategy as in the Newtonian case. First, we eliminate the terms proportional to e^h, from the force and velocity continuity equations giving

$$\begin{split}2\beta(1+\mathrm{De}^2)(A_i(h-1)+B_i) =& ((1+\beta)+2\beta De^2)(A_o(h-1)+B_o) + \\ &-(1-\beta)\mathrm{De}(E_o(h-1)+F_o),\end{split} \tag{4.25a}$$

$$\begin{split}2\beta(1+\mathrm{De}^2)(A_i h+B_i) =& ((1+\beta)+2\beta De^2)(A_o h+B_o) + \\ &-(1-\beta)\mathrm{De}(E_o h+F_o),\end{split} \tag{4.25b}$$

$$\begin{split}2\beta(1+\mathrm{De}^2)(E_i(h-1)+F_i) =& ((1+\beta)+2\beta De^2)(E_o(h-1)+F_o) + \\ &+(1-\beta)\mathrm{De}(A_o(h-1)+B_o),\end{split} \tag{4.25c}$$

$$\begin{split}2\beta(1+\mathrm{De}^2)(E_i h+F_i) =& -((1+\beta)+2\beta De^2)(E_o h+F_o) + \\ &-(1-\beta)\mathrm{De}(A_o h+B_o),\end{split} \tag{4.25d}$$

which has the solution

$$A_o = (1-\alpha)A_i + \gamma E_i, \tag{4.26a}$$

$$B_o = (1-\alpha)B_i + \gamma F_i, \tag{4.26b}$$

$$E_o = (1-\alpha)E_i - \gamma A_i, \tag{4.26c}$$

$$F_o = (1-\alpha)F_i - \gamma B_i. \tag{4.26d}$$

Here, $\alpha = (1-\beta^2)/((1+\beta)^2+4\beta^2\mathrm{De}^2)$ and $\gamma = 2\beta(1-\beta)\mathrm{De}/((1+\beta)^2+4\beta^2\mathrm{De}^2)$. For all β and De, $0 \le \alpha \le 1$ and $0 \le \gamma \le 1/2$. In the Newtonian case where $\mathrm{De} = 0$, we have $\alpha = \alpha_0$ and $\gamma = 0$ and we recover Eq. (4.16).

Second, we substitute Eq. (4.26) into Eqs. (4.24c), (4.24d), (4.24g) and (4.24h) to get the following

$$(A_i(h-1)+B_i)\alpha e^{-h} - (C_i(h+1)+D_i)e^{h} = (E_i(h-1)+F_i)\gamma e^{-h}, \tag{4.27a}$$

$$(A_i h+B_i)\alpha e^{-h} + (C_i h+D_i)e^{h} = (E_i h+F_i)\gamma e^{-h}, \tag{4.27b}$$

$$-(E_i(h-1)+F_i)\alpha e^{-h} + (G_i(h+1)+H_i)e^{h} = (A_i(h-1)+B_i)\gamma e^{-h}, \tag{4.27c}$$

$$(E_i h+F_i)\alpha e^{-h} + (G_i h+H_i)e^{h} = -(A_i h+B_i)\gamma e^{-h}. \tag{4.27d}$$

Now, we just have to solve Eq. (4.27) combined with Eqs. (4.24a), (4.24b), (4.24e) and (4.24f) to find the first-order solution. Doing so, we find Eq. (4.28), shown overleaf.

In Eq. (4.28), $p_\alpha(h) = (e^h + \alpha e^{-h})/2$ and $q_\alpha(h) = (e^h - \alpha e^{-h})/2$ as before and

$$\begin{gathered}
\mathcal{R}_0 = 2\alpha^2 + \gamma^2,\ \mathcal{P}_0(h) = 2 + 16h^2 + 16h^4,\ \mathcal{Q}_0(h) = -4\alpha(1+2h^2), \\
\mathcal{P}_1(h) = 1 - 4h + 4h^2 - 8h^3,\ \mathcal{Q}_1(h) = 4\alpha(1-2h), \\
\mathcal{P}_2(h) = 1 - 4h + 8h^2 - 8h^3 + 8h^4,\ \mathcal{Q}_2(h) = \alpha(-1+2h-2h^2), \\
\mathcal{P}_3(h) = -(1 + 4h + 4h^2 + 8h^3),\ \mathcal{Q}_3(h) = \alpha(3+2h+4h^2), \\
\mathcal{P}_4(h) = 1 + 4h + 8h^2 + 8h^3 + 8h^4,\ \mathcal{Q}_4(h) = -\alpha(3+2h+6h^2), \\
\mathcal{Q}_5(h) = \gamma(1-2h),\ \mathcal{Q}_6(h) = \gamma(1-2h+2h^2),\ \mathcal{Q}_7(h) = \gamma(1-2h+4h^2).
\end{gathered}$$

The first term of the swimming speed in Eq. (4.10), which we will label U_s, is given by

$$\begin{aligned}
U_s &= -\langle y_s\, \partial_y u_i^{(1)}\big|_{y=0}\rangle\epsilon = \frac{1}{2}(2A_i - B_i - 2C_i - D_i)\epsilon^2, \\
&= \epsilon^2\left(\frac{16\left(q_\alpha(h)^4 - \alpha^2h^4\right) + \gamma^2\left(\mathcal{P}_8(h) - 4e^{-2h}\alpha + e^{-4h}\mathcal{R}_0\right)}{32\left(q_\alpha(h)^2 - \alpha h^2\right)^2 + 2\gamma^2\left(\mathcal{P}_0(h) + e^{-2h}\mathcal{Q}_0(h) + e^{-4h}\mathcal{R}_0\right)}\right),
\end{aligned} \tag{4.29}$$

where $\mathcal{P}_8(h) = 2(1-8h^4)$.

To find the second term of the swimming speed in Eq. (4.10), we must find the x-average of the second-order x-velocity fields. Just as in the Newtonian case, we need to solve the x-average of the second-order x-components of Eqs. (4.2a) and (4.2b) as well as the x-average of the second-order xy-component

$$A_i = \frac{8\Big(q_\alpha(h)^2 - \alpha h^2\Big)\Big(q_\alpha(h)^2 + p_\alpha(h)q_\alpha(h) + \alpha h\Big) + \gamma^2\Big(\mathcal{P}_1(h) + e^{-2h}\mathcal{Q}_1(h)\Big)}{16\Big(q_\alpha(h)^2 - \alpha h^2\Big)^2 + \gamma^2\Big(\mathcal{P}_0(h) + e^{-2h}\mathcal{Q}_0(h) + e^{-4h}\mathcal{R}_0\Big)}, \tag{4.28a}$$

$$B_i = \frac{8\Big(q_\alpha(h)^2 - \alpha h^2\Big)\Big(q_\alpha(h)^2 + p_\alpha(h)q_\alpha(h) + \alpha h - \alpha h^2\Big) + \gamma^2\Big(\mathcal{P}_2(h) + e^{-2h}\mathcal{Q}_2(h)\Big)}{16\Big(q_\alpha(h)^2 - \alpha h^2\Big)^2 + \gamma^2\Big(\mathcal{P}_0(h) + e^{-2h}\mathcal{Q}_0(h) + e^{-4h}\mathcal{R}_0\Big)}, \tag{4.28b}$$

$$C_i = \frac{8\Big(q_\alpha(h)^2 - \alpha h^2\Big)\Big(p_\alpha(h)q_\alpha(h) - q_\alpha(h)^2 + \alpha h\Big) + \gamma^2\Big(\mathcal{P}_3(h) + e^{-2h}\mathcal{Q}_3(h) - e^{-4h}\mathcal{R}_0\Big)}{16\Big(q_\alpha(h)^2 - \alpha h^2\Big)^2 + \gamma^2\Big(\mathcal{P}_0(h) + e^{-2h}\mathcal{Q}_0(h) + e^{-4h}\mathcal{R}_0\Big)}, \tag{4.28c}$$

$$D_i = \frac{8\Big(q_\alpha(h)^2 - \alpha h^2\Big)\Big(q_\alpha(h)^2 - p_\alpha(h)q_\alpha(h) - \alpha h - \alpha^2 h\Big) + \gamma^2\Big(\mathcal{P}_4(h) + e^{-2h}\mathcal{Q}_4(h) + e^{-4h}\mathcal{R}_0\Big)}{16\Big(q_\alpha(h)^2 - \alpha h^2\Big)^2 + \gamma^2\Big(\mathcal{P}_0(h) + e^{-2h}\mathcal{Q}_0(h) + e^{-4h}\mathcal{R}_0\Big)}, \tag{4.28d}$$

$$E_i = \frac{4\gamma\Big((1 + 2h^2)q_\alpha(h)^2 + 2(h + h^2)p_\alpha(h)q_\alpha(h) + \alpha^2 h\Big) + \gamma^2 e^{-2h}\mathcal{Q}_5(h)}{16\Big(q_\alpha(h)^2 - \alpha h^2\Big)^2 + \gamma^2\Big(\mathcal{P}_0(h) + e^{-2h}\mathcal{Q}_0(h) + e^{-4h}\mathcal{R}_0\Big)}, \tag{4.28e}$$

$$F_i = -H_i = \frac{4\gamma\Big((1 + 2h^2)q_\alpha(h)^2 + 2hp_\alpha(h)q_\alpha(h) + \alpha^2 h\Big) + \gamma^2 e^{-2h}\mathcal{Q}_6(h)}{16\Big(q_\alpha(h)^2 - \alpha h^2\Big)^2 + \gamma^2\Big(\mathcal{P}_0(h) + e^{-2h}\mathcal{Q}_0(h) + e^{-4h}\mathcal{R}_0\Big)}, \tag{4.28f}$$

$$G_i = \frac{4\gamma\Big(q_\alpha(h)^2 + 2hp_\alpha(h)q_\alpha(h) + \alpha^2 h^2 e^{-h}\Big) + \gamma^2 e^{-2h}\mathcal{Q}_7(h)}{16\Big(q_\alpha(h)^2 - \alpha h^2\Big)^2 + \gamma^2\Big(\mathcal{P}_0(h) + e^{-2h}\mathcal{Q}_0(h) + e^{-4h}\mathcal{R}_0\Big)}. \tag{4.28g}$$

of Eq. (4.2d). Thus, we have

$$\partial_{yy}\langle u_i^{(2)}\rangle = 0, \tag{4.30a}$$

$$\beta\partial_{yy}\langle u_o^{(2)}\rangle + (1-\beta)\partial_y\langle\tau_{xy}^{(2)}\rangle = 0, \tag{4.30b}$$

$$\begin{aligned}\langle\tau_{xy}^{(2)}\rangle = \partial_y\langle u_o^{(2)}\rangle - \mathrm{De}\Big[&\langle u_o^{(1)}\partial_x\tau_{xy}^{(1)}\rangle + \langle v_o^{(1)}\partial_y\tau_{xy}^{(1)}\rangle \\ &- \langle D_{o,xy}^{(1)}(\tau_{xx}^{(1)} + \tau_{yy}^{(1)})\rangle + \langle\Omega_{o,xy}^{(1)}(\tau_{xx}^{(1)} - \tau_{yy}^{(1)})\rangle\Big],\end{aligned} \tag{4.30c}$$

where $\boldsymbol{\Omega}_{i,o} = (\nabla\boldsymbol{u}_{i,o}^T - \nabla\boldsymbol{u}_{i,o})/2$. We will address the boundary conditions later. Combining Eqs. (4.30a) and (4.30c) produces an ordinary differential equation for $\langle u_o^{(2)}\rangle$, the solution to which is

$$\langle u_i^{(2)}\rangle = I_i + J_i y, \tag{4.31a}$$

$$\langle u_o^{(2)}\rangle = I_o + J_o y - \frac{(1-\beta)\mathrm{De}^2 e^{-2y}}{2(1+\mathrm{De}^2)}K_o(y), \tag{4.31b}$$

where

$$\begin{aligned}K_o(y) = A_o^2(1-4y+2y^2) + 4A_oB_o(y-1) + 2B_o^2 +& \\ E_o^2(1-4y+2y^2) + 4E_oF_o(y-1) + 2F_o^2&.\end{aligned}$$

As always, the velocity field must vanish far from the sheet, thus $I_o = J_o = 0$. Velocity and force continuity at the interface, Eq. (4.4), provide our final two boundary conditions and we have

$$\begin{aligned}\langle u_i^{(2)}\rangle\Big|_{y=h} &= \langle u_o^{(2)}\rangle\Big|_{y=h}, \\ \beta\,\partial_y\langle u_i^{(2)}\rangle\Big|_{y=h} &= \beta\,\partial_y\langle u_o^{(2)}\rangle\Big|_{y=h} + (1-\beta)\,\langle\tau_{xy}^{(2)}\rangle\Big|_{y=h}.\end{aligned}$$

Solving this and using Eq. (4.26), we find that the second term of the swimming speed in Eq. (4.10), which we will label U_p, is given by

$$\begin{aligned}U_p = -\langle u_i^{(2)}\Big|_{y=0}\rangle\epsilon^2 = -I_i = \frac{(1-\beta)\mathrm{De}^2 e^{-2h}}{2(1+\mathrm{De}^2)}K_o(h)& \\ = \frac{(1-\beta)\mathrm{De}^2}{2(1+\mathrm{De}^2)}\left[\frac{\mathcal{R}_1\Big(4(1-2h^2)q_\alpha(h)^2 + 4\alpha h + e^{-2h}(\gamma^2 - 4h\mathcal{R}_2 + 2h^2\mathcal{R}_0)\Big)}{16\Big(q_\alpha(h)^2 - \alpha h^2\Big)^2 + \gamma^2\Big(\mathcal{P}_0(h) + e^{-2h}\mathcal{Q}_0(h) + e^{-4h}\mathcal{R}_0\Big)}\right]\epsilon^2&,\end{aligned} \tag{4.32}$$

where $\mathcal{R}_1 = (1-\alpha)^2 + \gamma^2$ and $\mathcal{R}_2 = \alpha^2 + \gamma^2$. Thus, the swimming speed of the sheet, U, to the lowest order in wave amplitude is given by

$$U = U_s + U_p. \tag{4.33}$$

With Eq. (4.33), we have a complete expression for the small-amplitude swimming speed of a sheet in a viscoelastic fluid with a depletion region. We will now consider swimming at finite amplitudes.

4.3 Finite-amplitude numerics

In this section, we adapt the spectral method solver we have developed in the previous chapters so that we can solve the depletion region problem for finite-amplitude waves. We begin by bounding the fluid domains by introducing walls above and below the sheet at a distance h_o from the centreline of the sheet. With the introduction of the wall, we need the additional boundary condition

$$\boldsymbol{u}_o\big|_{y=h_o} = \boldsymbol{u}_w. \tag{4.34}$$

We also re-label the thickness of the depletion region to h_i.

We limit ourselves to waveforms with up-down symmetry. Thus, the region above and below the sheet are the same and we only need consider the former. To summarise, we have a Newtonian inner fluid from $y = y_s(x,t)$ to $y = h_i$ and an outer fluid from $y = h_i$ to $y = h_o$, which is either Newtonian or governed by the Oldroyd-B equation. We take h_o to be sufficiently large that increasing it further does not change the calculated swimming speed of the sheet.

Our task is to find the velocity field in the inner fluid. From this, we can calculate the swimming speed of the sheet. To do this we solve either Eq. (4.1) or Eq. (4.2), depending on whether the outer fluid is Newtonian or viscoelastic, along with the boundary conditions Eqs. (4.3), (4.4) and (4.34).

We begin by both removing any explicit time dependence and by dedimensionalising the problem with the following transformation to starred quantities

$$x^* = k(x - (c - U)t),\ y^* = ky,\ f^* = kf,\ h_{i,o}^* = kh_{i,o}$$
$$U^* = \frac{U}{c},\ u_{i,o}^* = 1 - \frac{U}{c} + \frac{u_{i,o}}{c},\ v_{i,o}^* = \frac{v_{i,o}}{c},$$
$$p_{i,o}^* = \frac{p_{i,o}}{\eta_{i,o}ck},\ \boldsymbol{\tau}^* = \frac{\boldsymbol{\tau}}{\eta_p ck},\ \boldsymbol{\Sigma}_{i,o}^* = \frac{\boldsymbol{\Sigma}_{i,o}}{\eta_{i,o}ck}.$$

In this frame, which is co-moving with the wave, the shape of the sheet is fixed in time, such that $y_s^*(x^*) = kf(x^*)$. From now on we will drop the *s for clarity.

In our frame, the material points of the walls are moving with a velocity $\boldsymbol{u}_w = -(1 - U)\boldsymbol{e}_x$ and the material points of the sheet are moving with a velocity $\boldsymbol{u}_s = (u_s, v_s)^T$, given by

$$u_s(x) = -\frac{Q}{\sqrt{1 + f'(x)^2}}, \tag{4.35a}$$
$$v_s(x) = -\frac{Qf'(x^*)}{\sqrt{1 + f'(x)^2}},, \tag{4.35b}$$

where
$$Q = \int_0^{2\pi} \sqrt{1 + f'(x)^2}\mathrm{d}x,$$
as was originally found by Taylor [5].

Next, we transform the (x, y)-coordinates into two independent coordinate systems for the inner and outer domains $(\eta_{i,o}, \xi_{i,o})$, which are related to the original coordinates via

$$\eta_{i,o} = x, \tag{4.36a}$$
$$\xi_i = 1 - 2\frac{y - h_i}{kf(x) - h_i}, \tag{4.36b}$$
$$\xi_o = 1 - 2\frac{y - h_o}{h_i - h_o}. \tag{4.36c}$$

In these new coordinates, both domains are periodic rectangular strips, for which the Fourier-Chebyshev basis has good convergence properties. In the inner domain, $\xi_i = 1$ corresponds to the interface and $\xi_i = -1$ corresponds to the sheet; whereas in the outer domain, $\xi_o = -1$ corresponds to the interface and $\xi_i = 1$ corresponds to the outer wall.

We introduce a two-dimensional stream-function $\psi_{i,o}(x, y)$, which is defined via its relationship to $\boldsymbol{u}_{i,o} = (u_{i,o}, v_{i,o})^T$: $u_{i,o} = \partial_y \psi_{i,o}$ and $v_{i,o} = -\partial_x \psi_{i,o}$. We then separate the stream-function from the pressure field by solving the curl and divergence of the force balance equation, which is either Eq. (4.1a) or Eqs. (4.2a) and (4.2b). In the case of a viscoelastic outer fluid, we also need the constitutive equations that govern the polymeric stress $\boldsymbol{\tau}$ (Eq. (4.2d)). Thus, for the inner fluid and for a Newtonian outer fluid we have

$$\nabla^4 \psi_{i,o} = 0, \tag{4.37a}$$

$$\nabla^2 p_{i,o} = 0; \tag{4.37b}$$

and for a viscoelastic outer fluid we have

$$\beta \nabla^4 \psi_o - (1-\beta)\Big[\Box^2 \tau_{xy} - \partial_{xy}(\tau_{xx} - \tau_{yy})\Big] = 0, \tag{4.38a}$$

$$\nabla^2 p_o - (1-\beta)\Big[\partial_{xx}\tau_{xx} + 2\partial_{xy}\tau_{xy} + \partial_{yy}\tau_{yy}\Big] = 0, \tag{4.38b}$$

$$\tau_{xx} - 2\partial_{xy}\psi_o + \mathrm{De}\Big[(\partial_y\psi_o\partial_x - \partial_x\psi_o\partial_y)\tau_{xx} - 2\tau_{xx}\partial_{xy}\psi_o - 2\tau_{xy}\partial_{yy}\psi_o\Big] = 0, \tag{4.38c}$$

$$\tau_{xy} + \Box^2\psi_o + \mathrm{De}\Big[(\partial_y\psi_o\partial_x - \partial_x\psi_o\partial_y)\tau_{xy} + \tau_{xx}\partial_{xx}\psi_o - \tau_{yy}\partial_{yy}\psi_o\Big] = 0, \tag{4.38d}$$

$$\tau_{yy} + 2\partial_{xy}\psi_o + \mathrm{De}\Big[(\partial_y\psi_o\partial_x - \partial_x\psi_o\partial_y)\tau_{yy} + 2\tau_{xy}\partial_{xx}\psi_o + 2\tau_{yy}\partial_{xy}\psi_o\Big] = 0, \tag{4.38e}$$

where $\Box^2 = \partial_{xx} - \partial_{yy}$, $\beta = \eta_s/(\eta_s + \eta_p)$ is the viscosity ratio, and $\mathrm{De} = \lambda c k$ is the Deborah number of the fluid.

In each of the domains, we represent the hydrodynamic fields by truncated Fourier-Chebyshev series. For example, the pressure field in the inner fluid p_i is given by

$$p_i(\eta, \xi) = \sum_{n=0}^{N-1}\sum_{m=0}^{M-1} p_i^{(nm)} F_n(\eta) T_m(\xi), \tag{4.39}$$

where $T_m(\xi) = \cos(m \arccos(\xi))$ is the mth Chebyshev polynomial, and

$$F_n(\eta) = \begin{cases} \sin(\frac{n+1}{2}\eta) & n \text{ odd} \\ \cos(\frac{n}{2}\eta) & n \text{ even}, \end{cases}$$

is the nth Fourier mode. We increase the resolution (N, M) of the fields until the relative error in the swimming speed between the two highest resolutions is no more than 0.5%. We find that if the outer fluid is Newtonian, $N = 21$ and $M = 60$ is sufficient. For a viscoelastic outer fluid, we find that resolutions of $N = 31$ and $M = 80$ are required for the data presented.

In each domain, the spatial derivative matrices ∂_x and ∂_y associated with the these truncated Fourier-Chebyshev series are given by

$$\left(\frac{\partial}{\partial x}\right)_i = \frac{\partial}{\partial \eta_i} + (\xi_i - 1)\frac{kf'(\eta_i)}{h_i - kf(\eta_i)}\frac{\partial}{\partial \xi_i}, \tag{4.40a}$$

$$\left(\frac{\partial}{\partial y}\right)_i = \frac{2}{h_i - kf(\eta_i)}\frac{\partial}{\partial \xi_i}, \tag{4.40b}$$

$$\left(\frac{\partial}{\partial x}\right)_o = \frac{\partial}{\partial \eta_o}, \tag{4.40c}$$

$$\left(\frac{\partial}{\partial y}\right)_o = \frac{2}{h_o - h_i}\frac{\partial}{\partial \xi_o}. \tag{4.40d}$$

Here $\partial_{\eta_{i,o}}$ and $\partial_{\xi_{i,o}}$ are the $NM \times NM$ spectral derivative matrices, which when multiplying vectors of spectral coefficients produce the associated derivatives [77, 78].

To calculate products of the fields represented in the spectral space, we use the Fast Fourier transform [78] with the following collocation points

$$\eta_{n_c} = \frac{2\pi n_c}{N_c}, \tag{4.41a}$$

$$\xi_{m_c} = \cos\left(\frac{\pi m_c}{M_c - 1}\right). \tag{4.41b}$$

We use these to evaluate the fields in the real space, calculate their product and transform the result back to the spectral space. Here, $n_c \in [0, N_c)$, $m_c \in [0, M_c)$ and the collocation resolution (N_c, M_c) is selected to satisfy both $N_c > 1.5N$ and $M_c > 1.5M$ in order to avoid aliasing issues [77, 78].

If the outer fluid is Newtonian, then the representation of the governing equations in each fluid domain yields a set of $4NM$ linear algebraic equations in the truncated Fourier-Chebyshev basis. If the outer fluid is viscoelastic, then the representation is a set of $7NM$ algebraic equations, $3NM$ of which are non-linear. These sets of equations must be complemented by boundary conditions.

We have already imposed periodicity in the η-direction via the use of Fourier modes in our basis. Additionally, if the outer fluid is viscoelastic, then we do not need any boundary conditions for the polymeric stress as we have a steady state solution and the only derivatives of $\boldsymbol{\tau}$ are time derivatives. Thus, we need an additional 12 boundary conditions (four for each of $\psi_{i,o}$ and two for each of $p_{i,o}$) along the lines $\xi_{i,o} = \pm 1$. These boundary conditions are functions of η and thus yield a set of $12N$ discretised boundary conditions to substitute into the original set of $4NM$ (or $7NM$) discretised governing equations. As we have seen in previous chapters, we have a different set of boundary conditions for the $n = 0$ and the $n \neq 0$ Fourier modes. First, let us consider the $n \neq 0$ boundary conditions.

The first boundary conditions to consider are the no-slip boundary conditions at both the sheet and the wall as well as the continuity of velocity at the interface, as found in Eqs. (4.3), (4.4a) and (4.34), where the velocities of the material points of the sheet are given by Eq. (4.35) and $\boldsymbol{u}_w = (U - 1)\boldsymbol{e}_x$. These six boundary conditions are given by

$$\partial_y \psi_i|_{\xi_i=-1} = u_s, \tag{4.42a}$$
$$-\partial_x \psi_i|_{\xi_i=-1} = v_s, \tag{4.42b}$$
$$\partial_y \psi_i|_{\xi_i=1} = \partial_y \psi_o|_{\xi_o=-1}, \tag{4.42c}$$
$$-\partial_x \psi_i|_{\xi_i=1} = -\partial_x \psi_o|_{\xi_o=-1}, \tag{4.42d}$$
$$\partial_y \psi_o|_{\xi_o=1} = U - 1, \tag{4.42e}$$
$$-\partial_x \psi_o|_{\xi_o=1} = 0. \tag{4.42f}$$

The second set of boundary conditions we need is the continuity of force between the two fluid domains at the interface (Eq. (4.4b)). As these boundary conditions depend on the stresses in the fluid, they are different depending on the governing equations of the outer fluid. If the outer fluid is Newtonian, then we have the following

$$\beta\Big[(\partial_{yy} - \partial_{xx})\psi_i\Big]_{\xi_i=1} = \Big[(\partial_{yy} - \partial_{xx})\psi_o\Big]_{\xi_o=-1}, \tag{4.43a}$$
$$\beta\Big[p_i + \partial_{xy}\psi_i\Big]_{\xi_i=1} = \Big[p_o + \partial_{xy}\psi_o\Big]_{\xi_o=-1}. \tag{4.43b}$$

Whereas, if the outer fluid is viscoelastic we have

$$\beta\Big[(\partial_{yy} - \partial_{xx})\psi_i\Big]_{\xi_i=1} = \Big[\beta(\partial_{yy} - \partial_{xx})\psi_o + (1-\beta)\tau_{xy}\Big]_{\xi_o=-1}, \tag{4.44a}$$
$$\beta\Big[p_i + \partial_{xy}\psi_i\Big]_{\xi_i=1} = \Big[p_o + \beta\partial_{xy}\psi_o - (1-\beta)\tau_{yy}\Big]_{\xi_o=-1}. \tag{4.44b}$$

The final set of boundary conditions for the $n \neq 0$ Fourier modes is to require that the fields satisfy the local force balance equation $\nabla \cdot \boldsymbol{\Sigma}_{i,o} = \boldsymbol{0}$. So far, we have only required that the curl and the divergence of this force balance equation is satisfied, we fix the curl and divergence free terms of the hydrodynamic fields by requiring $\boldsymbol{n} \cdot \nabla \cdot \boldsymbol{\Sigma}_{i,o} = 0$ at the sheet and interface for the inner fluid and at the interface and wall for the outer fluid. Here, $\boldsymbol{n}$ is the normal of the sheet, interface or wall as appropriate. These boundary conditions depend on the stresses, and also the geometry of the two domains. Thus, we have a different set of boundary conditions for the inner fluid, a Newtonian outer fluid and a viscoelastic outer fluid. For the inner fluid we have the following

$$\Big[f'(\eta_{i,o})\partial_x p_{i,o} - \partial_y p_{i,o} - (f'(\eta_{i,o})\partial_y + \partial_x)\nabla^2\psi_{i,o}\Big]_{\xi_{i,o}=-1} = 0, \tag{4.45a}$$

$$\Big[\partial_y p_{i,o} + \partial_x \nabla^2 \psi_{i,o}\Big]_{\xi_{i,o}=1} = 0, \tag{4.45b}$$

where $(0,-1)^T$ is the normal to the interface and $(-f'(\eta),1)^T$ the normal of the sheet. And for a Newtonian outer fluid we have

$$\Big[\partial_y p_o + \partial_x \nabla^2 \psi_o\Big]_{\xi_o=-1} = 0, \tag{4.46a}$$

$$\Big[\partial_y p_o + \partial_x \nabla^2 \psi_o\Big]_{\xi_o=1} = 0, \tag{4.46b}$$

where $(0,-1)^T$ is the normal to the wall and $(0,1)^T$ is the normal to the interface. And finally for a viscoelastic outer fluid, we have the following

$$\Big[\partial_y p_o + \beta\partial_x \nabla^2 \psi_o - (1-\beta)(\partial_x \tau_{xy} - \partial_y \tau_{yy})\Big]_{\xi_o=-1} = 0, \tag{4.47a}$$

$$\Big[\partial_y p_o + \beta\partial_x \nabla^2 \psi_o - (1-\beta)(\partial_x \tau_{xy} - \partial_y \tau_{yy})\Big]_{\xi_o=1} = 0. \tag{4.47b}$$

For the $n = 0$ Fourier modes, the x-derivatives vanish. This leads to some boundary conditions being automatically satisfied, i.e. Eqs. (4.42b), (4.42d) and (4.42f) and these must be replaced. Also, with vanishing x-derivatives for either Eq. (4.43b) (for a Newtonian outer fluid) or Eq. (4.44b) (for a viscoelastic outer fluid), we have conditions which link the constant terms of the pressure in the two fluids. These constant terms have no physical significance and can be set to arbitrary values. For reasons of aesthetics, we choose to set them independently, making these conditions redundant and in need of replacement.

For the $n = 0$ mode, there are special conditions on the x-forces (discussed below) that require that both the left- and right-hand-sides of Eqs. (4.43a) and (4.44a) independently vanish for Newtonian and viscoelastic fluids respectively. Thus, again mainly for aesthetic reasons, we choose to replace this boundary condition as well.

We also find that for the $n = 0$ Fourier modes, each of the pairs of equations in Eqs. (4.45) to (4.47) become degenerate and one of the equations in each of the pairs must be replaced. Finally, we do not know the swimming speed U, thus we must replace the $n = 0$ mode of Eq. (4.42e). In total then, we have eight of the 12 boundary conditions to replace for the $n = 0$ Fourier mode .

As we have already pointed out, the constant terms in the pressure fields, $p_{i,o}$ have no physical significance and can be set to arbitrary values. The same is true for the constant terms in $\psi_{i,o}$. Thus, the first four replacements of the seven we require for the $n = 0$ Fourier modes are simply setting these values via

$$p_{i,o}\big|_{\xi=1} = 0, \tag{4.48a}$$

$$\psi_{i,o}\big|_{\xi=1} = 0. \tag{4.48b}$$

We also require that there is no average x-force acting on either of the fluid domains, the sheet, the interface or the wall. As the system as a whole must be in mechanical equilibrium, these five average x-forces can be set to zero by requiring that the average x-forces applied by (i) the inner fluid to the sheet, (ii) the inner fluid to the interface, (iii) the outer fluid to the interface and (iv) the outer fluid to the wall all vanish independently. Thus for the inner fluid, we have the following two replacement boundary conditions for the $n = 0$ Fourier mode

$$(\partial_{xx} - \partial_{yy})\psi_i\big|_{\xi_i=1} = 0, \tag{4.49a}$$

$$\Big[f'(\eta_i)p_+ - 2f'(\eta_i)\partial_{xy}\psi_i - (\partial_{xx} - \partial_{yy})\psi_i\Big]_{\xi_i=-1} = 0. \tag{4.49b}$$

For the outer fluid, we have two more replacement boundary conditions, which if the outer fluid is Newtonian are given by

$$(\partial_{xx} - \partial_{yy})\psi_o\big|_{\xi_o=-1} = 0, \tag{4.50a}$$

$$(\partial_{xx} - \partial_{yy})\psi_o\big|_{\xi_o=1} = 0. \tag{4.50b}$$

Or if the outer fluid is viscoelastic, then they are given by

$$\Big[\beta(\partial_{xx} - \partial_{yy})\psi_o + (1-\beta)\tau_{xy}\Big]_{\xi_o=-1} = 0, \tag{4.51a}$$

$$\Big[\beta(\partial_{xx} - \partial_{yy})\psi_o + (1-\beta)\tau_{xy}\Big]_{\xi_o=1} = 0, \tag{4.51b}$$

In the spirit of the Chebyshev-tau method [78], for each Fourier mode we replace

	$n = 0$	$0 < n < N$
$0 \leq m < M - 4$	Equation (4.37a)(i) Equation (4.37b)(i) Equation (4.37a)(o) Equation (4.37b)(o)	Equation (4.37a)(i) Equation (4.37b)(i) Equation (4.37a)(o) Equation (4.37b)(o)
$m = M - 4$	Equation (4.49b) Equation (4.37b)(i) Equation (4.50a) Equation (4.37b)(o)	Equation (4.43b) Equation (4.37b)(i) Equation (4.42f) Equation (4.37b)(o)
$m = M - 3$	Equation (4.49a) Equation (4.37b)(i) Equation (4.50b) Equation (4.37b)(o)	Equation (4.43a) Equation (4.37b)(i) Equation (4.42e) Equation (4.37b)(o)
$m = M - 2$	Equation (4.48b)(i) Equation (4.48a)(i) Equation (4.48b)(o) Equation (4.48a)(o)	Equation (4.42b) Equation (4.45b) Equation (4.42d) Equation (4.46b)
$m = M - 1$	Equation (4.42a) Equation (4.45a) Equation (4.42c) Equation (4.46a)	Equation (4.42a) Equation (4.45a) Equation (4.42c) Equation (4.46a)

Table 4.1 An outline how of the $4NM$ discretised equations are constructed from the differential equations in Eq. (4.37) and the various boundary conditions in Eqs. (4.42) to (4.51) for a Newtonian outer fluid. If an equation referenced in this table is subscripted by i, o then which subscript to select in the given position is in parenthesis after the equation number.

the four highest Chebyshev modes of the discretised Eq. (4.37a) (or Eq. (4.38a) for a viscoelastic outer fluid) and the two highest modes of Eq. (4.37b) (or Eq. (4.38b)) with the boundary conditions outlined. Combining this all together leads to a set of $4NM$ (or $7NM$) discretised equations, with the structure outlined in Table 4.1 (or Table 4.2).

We can now solve these sets of equations for either the Newtonian or viscoelastic case and, provided that (N, M) is large enough, we will have the complete solution to the problem. From this complete solution we can extract the swimming speed via

$$U = \partial_y \psi_o\big|_{\xi_o=1} + 1.$$

If the outer fluid is Newtonian, then the problem is linear and solving is as trivial as inverting the resulting $4NM \times 4NM$ matrix described in Table 4.1. In the

	$n = 0$	$0 < n < N$
$0 \leq m < M - 4$	Equation (4.37a)(i)	Equation (4.37a)(i)
	Equation (4.37b)(i)	Equation (4.37b)(i)
	Equation (4.38a)	Equation (4.38a)
	Equation (4.38b)	Equation (4.38b)
	Equations (4.38c) to (4.38e)	Equations (4.38c) to (4.38e)
$m = M - 4$	Equation (4.49b)	Equation (4.44b)
	Equation (4.37b)(i)	Equation (4.37b)(i)
	Equation (4.50a)	Equation (4.42f)
	Equation (4.38b)	Equation (4.38b)
	Equations (4.38c) to (4.38e)	Equations (4.38c) to (4.38e)
$m = M - 3$	Equation (4.49a)	Equation (4.44a)
	Equation (4.37b)(i)	Equation (4.37b)(i)
	Equation (4.51b)	Equation (4.42e)
	Equation (4.38b)	Equation (4.38b)
	Equations (4.38c) to (4.38e)	Equations (4.38c) to (4.38e)
$m = M - 2$	Equation (4.48b)(i)	Equation (4.42b)
	Equation (4.48a)(i)	Equation (4.45b)
	Equation (4.48b)(o)	Equation (4.42d)
	Equation (4.48a)(o)	Equation (4.47b)
	Equations (4.38c) to (4.38e)	Equations (4.38c) to (4.38e)
$m = M - 1$	Equation (4.42a)	Equation (4.42a)
	Equation (4.45a)	Equation (4.45a)
	Equation (4.42c)	Equation (4.42c)
	Equation (4.47a)	Equation (4.47a)
	Equations (4.38c) to (4.38e)	Equations (4.38c) to (4.38e)

Table 4.2 Outline how of the $7NM$ discretised equations are constructed from the differential equations in Eq. (4.38) and the various boundary conditions in Eqs. (4.42) to (4.51) for a viscoelastic outer fluid. If an equation referenced in this table is subscripted by i, o then which subscript to select in the given position is in parenthesis after the equation number.

viscoelastic case, things are more difficult because the problem is non-linear. We use a Newtonian-Raphson method with an analytically calculated $7NM \times 7NM$ Jacobian to find a solution for a given set of parameters. Unfortunately, this will not converge for a given Deborah number from an arbitrary initial guess. To get around this, we use an analytic continuation method where we start from $\mathrm{De} = 0$, which is linear and can always be solved, and then increment De by some small step $\Delta\mathrm{De}$, and use the Newton-Raphson solver with the previous solution as an initial guess. We repeat this process until we reach the desired Deborah number. In practice, for some sets of parameters this still might fail to converge, at which point we try a smaller $\Delta\mathrm{De}$ and continue the process. In some cases, $\Delta\mathrm{De}$ becomes too small to make reasonable progress. Where this occurs, we just report the largest De we can achieve.

Note that our numerical solver assumes that the sheet is entirely in the inner fluid, thus, we cannot solve the problem with $h < b$ using this method. However, given the mechanism we outlined in Section 4.1.1, this scenario is not physically relevant.

4.4 Results

Figure 4.2 shows the swimming speed for a sine-waving sheet in the depletion region of a Newtonian fluid as a function of depletion-region thickness h for various wave amplitudes b and viscosity ratios β. The numerical results (symbols) from the solver outlined in Section 4.3 are compared to the small-amplitude analysis (solid line) showing good agreement for $bk = 0.01$ and $bk = 0.1$.

In the small-amplitude case, the swimming speed is given by Eq. (4.19). We see that U is always greater than $U_{BN} = cb^2k^2/2$, the small-amplitude swimming speed in a single Newtonian fluid. The bulk Newtonian swimming speed U_{BN} is recovered in the limits of $h \to 0$ and $h \to \infty$ as expected, because in both of these limits we are swimming in a single Newtonian fluid. In between these two extremes, there is an optimal depletion region thickness where the swimming speed is maximised. At $\beta = 1$ ($\eta = \eta_s$), this maximum disappears as $U = U_{BN}$ for all h. As β decreases, the optimal depletion region thickness h^* decreases and the maximum swimming speed increases. At $\beta = 0$, we find $h^*k = 0$ and the maximum swimming speed diverges. This recovers the swimming speed next to a wall in a Newtonian fluid [74], which is expected as $\beta = 0$ corresponds to $\eta_s \ll \eta$,

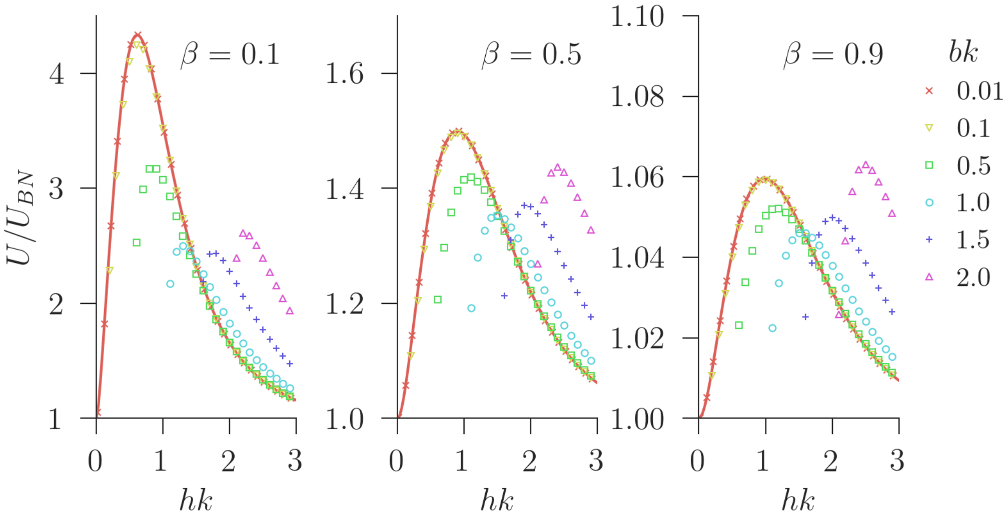

Figure 4.2 The swimming speed U against depletion-region thickness h, for a sine-waving sheet ($f(\zeta) = b\sin(\zeta)$), with a Newtonian outer fluid for various wave amplitudes b and viscosity ratios β. The small-amplitude expression (solid line) found in Eq. (4.19) agrees with the numerical solution (symbols) at $bk = 0.01$ and $bk = 0.1$. In all cases, the swimming speed is scaled by the swimming speed of the sheet in the bulk of a single Newtonian fluid, U_{BN}. See the text for more details.

i.e. the outer fluid becomes a solid.

At larger wave amplitudes, we find qualitatively similar behaviour as in the small-amplitude case with $h - b$ taking the role of h. As $h - b$ approaches 0, we find that U approaches U_{BN}. Unfortunately, we cannot reach sufficiently small $h - b$ to probe this region further. The scaled swimming speed increases with $h - b$ before reaching a peak scaled swimming speed, which is usually smaller than the small-amplitude peak scaled swimming speed, at some optimal $h - b$. As $h - b$ increases further, the swimming speed decreases tending to $U = U_{BN}$, as $h - b \to \infty$. At larger wave amplitudes, the maximum swimming speed has a similar β dependence as in the small-amplitude case. At large β, the presence of the depletion region has very little effect and the maximum swimming speed is $\approx U_{BN}$. As β decreases, the maximum swimming increases and the optimal depletion-region thickness tends to $h^* = b$. This recovers the behaviour we found for a finite-amplitude waving sheet swimming next to a wall in a Newtonian fluid. Interestingly, the peaks in scaled swimming speed do not monotonically decrease with the wave amplitude b. The maximum scaled swimming speed U/U_{BN} is larger for $bk = 2.0$ than it is for smaller bk. For $\beta = 0.9$, the maximum scaled swimming speed is in fact faster than in the small-amplitude case.

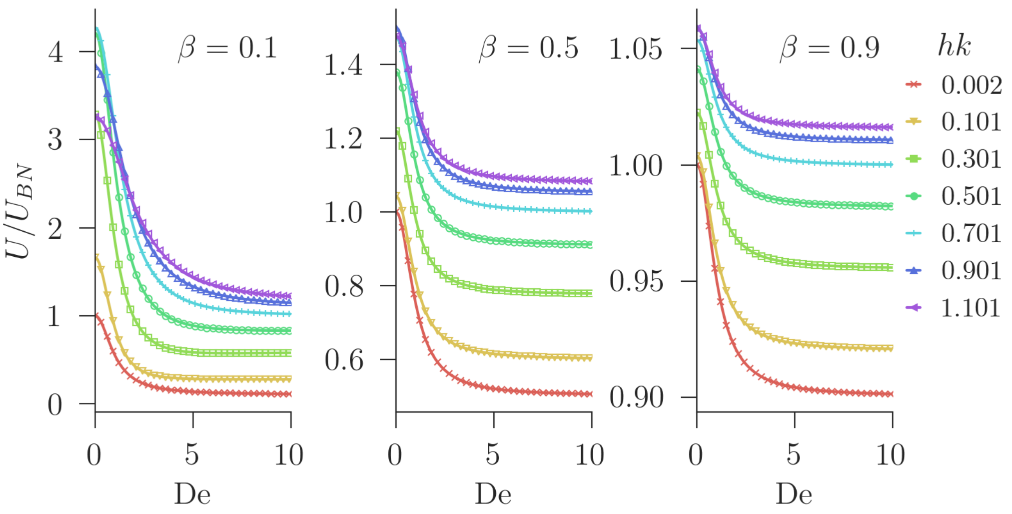

Figure 4.3 Swimming speed U against Deborah number De of a small-amplitude sine-waving sheet ($f(\zeta) = b\sin(\zeta)$) in the depletion region of a viscoelastic fluid, at various thicknesses h and viscosity ratios β. The swimming speeds are scaled by the swimming speed of the same sheet in a single Newtonian fluid, U_{BN}. The numerical results (symbols) ($bk = 0.001$) are compared to the small amplitude analysis, Eq. (4.33) (solid lines) showing good agreement.

Figure 4.3 shows the swimming speed U as a function of Deborah number De for a small-amplitude sine-waving sheet swimming in the depletion region of a viscoelastic fluid, at various thicknesses h and viscosity ratios β. The numerical results (symbols) from our solver outlined in Section 4.3 with $bk = 0.001$ are compared to the small-amplitude result Eq. (4.33) showing good agreement.

From the small-amplitude expression in Eq. (4.33), we find that in the limits of $hk \to 0$ and $hk \to \infty$, we recover the bulk swimming speeds in a viscoelastic fluid and a Newtonian fluid, respectively, as expected. As a function of Deborah number, the swimming speed behaves in a similar manner to swimming in the bulk of a single viscoelastic fluid as in Chapter 2. The swimming speed decreases from its zero Deborah number value $U_0 > U_{BN}$ with increasing Deborah number, down to some plateau swimming speed. By taking De $\to \infty$ we find the plateau swimming speed U_∞ is given by

$$U_\infty = \frac{cb^2k^2}{2}\left(1 + (1-\beta)(2h^2-1)e^{-2h}\right). \tag{4.52}$$

When swimming in a single viscoelastic fluid ($hk = 0.0$), we have $U_\infty = \beta U_{BN}$. As $hk \to \infty$, U_∞ becomes the swimming speed U_{BN} of a sheet in the bulk of a Newtonian fluid, as expected. For all β, if $hk > 1/\sqrt{2}$ then $U_\infty > U_{BN}$ and the

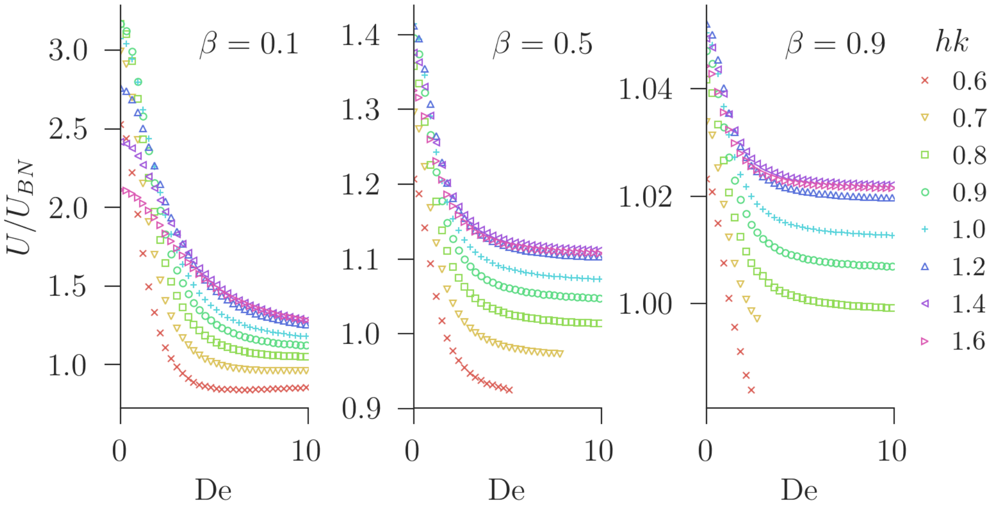

Figure 4.4 Swimming speed U against Deborah number De for a sine-waving sheet ($f(\zeta) = b\sin(\zeta)$), with amplitude $bk = 0.5$, in the depletion region of a viscoelastic fluid at various thicknesses h and viscosity ratios β.

maximum plateau swimming speed occurs at $hk = (1 + \sqrt(3))/2$.

Figure 4.4 shows the swimming speed U against Deborah number De for a sine-waving sheet with amplitude $bk = 0.5$ in the depletion region of a viscoelastic fluid at various thicknesses h and viscosity ratios β. This was calculated by the numerical solver outlined in Section 4.3. Unfortunately, we were unable to resolve the problem for larger bk. However, the data presented shows the behaviour of the swimmer at moderate wave amplitudes.

At moderate amplitudes, we find qualitative agreement with the small-amplitude analysis. The swimming speed decreases from its zero Deborah number value, $U_0 > U_{BN}$, with increasing Deborah number down to some plateau swimming speed. Just as for small amplitudes, this decrease is not monotonic for small β and small $(h - b)k$. The plateau value $U_\infty > \beta U_{BN}$ for all the hk reported. From Chapter 2, we know that when $hk = 0$, this is still the case. The plateau value increases with increasing hk; and for $hk \gtrsim 1/\sqrt{2}$, we have $U_\infty > U_{BN}$. This suggests that the ratio U_∞/U_{BN} has a weak dependence on the wave amplitude bk.

We now provide a physical mechanistic explanation of the observed behaviour.

4.5 Discussion

We can understand the physical mechanism responsible for the behaviour of Taylor's sheet in the depletion region of a viscoelastic fluid in terms of the mechanisms we identified in Chapters 2 and 3. To begin, let us ignore the viscoelasticity of the outer fluid and just focus on the Newtonian results in Eq. (4.19) and Fig. 4.2.

Recall from Section 1.1.3 that the vertical motion of the material points of the sheet create an array of vortices with alternating direction of rotation near the sheet in the incompressible fluid. In addition, recall from Chapter 3 that when swimming next to a wall, Taylor's sheet is faster than when unconfined. We showed that this behaviour is due to the sheet vortices increasing in speed. The same mechanistic principle can explain the behaviour of the swimming in a depletion region with a Newtonian outer fluid. In other words, the outer fluid behaves as a soft wall, which increases the speed of the sheet vortices; and consequently, increases the speed of the sheet.

Equation (4.19) shows that the small-amplitude swimming speed of the sheet in this scenario depends on the dimensionless viscosity difference $\alpha_0 = (1-\beta)/(1+\beta) = (\eta - \eta_s)/(\eta + \eta_s)$. If $\alpha_0 = 0$, then we have $\eta = \eta_s$. The two Newtonian fluids are identical and the interface has no physical significance. As we expect, Eq. (4.19) reduces to the small-amplitude swimming speed $U_{BN} = cb^2k^2/2$ of a sheet in the bulk of a Newtonian fluid. Similarly, for $\alpha_0 = 1$ we have $\eta \gg \eta_s$. Velocities in the outer fluid are so slow that we can consider it to be a solid. As a result, the velocity continuity equations at the interface become no-slip conditions at the solid surface. In this scenario, we recover the swimming speed U of Taylor's sheet at the centre of a channel of width $2h$, originally found by Katz [74]:

$$U = \frac{cb^2k^2}{2}\frac{\sinh^2(hk) + h^2k^2}{\sinh^2(hk) - h^2k^2}. \tag{4.53}$$

At intermediate α_0, we find an interpolation between these two extremes. This is the so-called soft-wall effect. This argument applies regardless of the amplitude of the wave. Setting $\alpha_0 = 0$ or $\alpha_0 = 1$ changes the boundary conditions to swimming in the bulk of a fluid and swimming next to a wall respectively. Thus, at finite amplitudes the soft-wall effect also occurs.

If the soft wall is viscoelastic, then we find from Eq. (4.33) that, at small-amplitudes, viscoelasticity turns off the soft-wall effect. In addition, viscoelastic agents in the outer fluid push the entire inner fluid via mechanisms similar to those we discussed in Chapter 2. In the outer fluid, the flow field consists of a vortex array located near the sheet. There is a linear viscoelastic response to the local oscillatory shear created by the vortices in the outer fluid. This viscoelastic response interacts with the vortices in the outer fluid as in Eq. (4.30c). As a result, it pushes on the inner fluid. Viscoelastic agents pushing on the sheet always slow the sheet down. In contrast, viscoelastic agents pushing on the inner fluid can either slow the sheet down or speed it up, depending on the depletion-region thickness. For $h > 1/\sqrt{2}$, the viscoelastic response speeds up the sheet. Conversely, for $h < 1/\sqrt{2}$, the viscoelastic response slows the sheet down. As such, the enhanced propulsion of the waving sheet at large Deborah numbers for $hk > 1/\sqrt{2}$ is not due to the soft-wall effect; but instead due to the viscoelastic effects in the outer fluid.

To demonstrate this, consider Fig. 4.5, which shows the two contributions to the small-amplitude swimming speed U_s and U_p separately, as functions of Deborah number De. U_s is the first term in Eq. (4.10) and is the only term that contributes for a Newtonian outer fluid. U_s contains the contribution to the swimming speed due to the soft-wall effect. In contrast, U_p is the contribution to the swimming speed due to the viscoelasticity of the outer fluid. Figure 4.5 shows that U_s approaches U_{BN} at large Deborah numbers; and that U_p approaches some plateau value, which is positive, i.e. in the direction of swimming, for $hk > 1/\sqrt{2}$ and is negative, i.e. opposing the direction of swimming, for $hk < 1/\sqrt{2}$. Thus, viscoelasticity turns off the Newtonian soft-wall effect in favour of a polymeric effect, resulting from the interaction of the linear viscoelastic response to local oscillatory shear flows and the vortices.

Viscoelasticity turns off the soft-wall effect because the soft-wall effect is caused by the viscous component of the linear viscoelastic response. As the Deborah number increases, the viscoelastic agents do not have time to react to the local oscillatory shear, and stop responding viscously, turning off the soft-wall effect.

To understand the origin of the crossover depletion-region thickness, recall from Chapter 3 that the contribution from the advective term $\boldsymbol{u} \cdot \nabla \boldsymbol{\tau}$ in Eq. (4.2d) is only non-zero if the object being pushed by the viscoelastic agents coincides with the centreline of the vortices. We showed that, because the centreline of the vortices is raised slightly by the introduction of the wall, the advection term contributed a push on the sheet (now below the centreline) against the direction

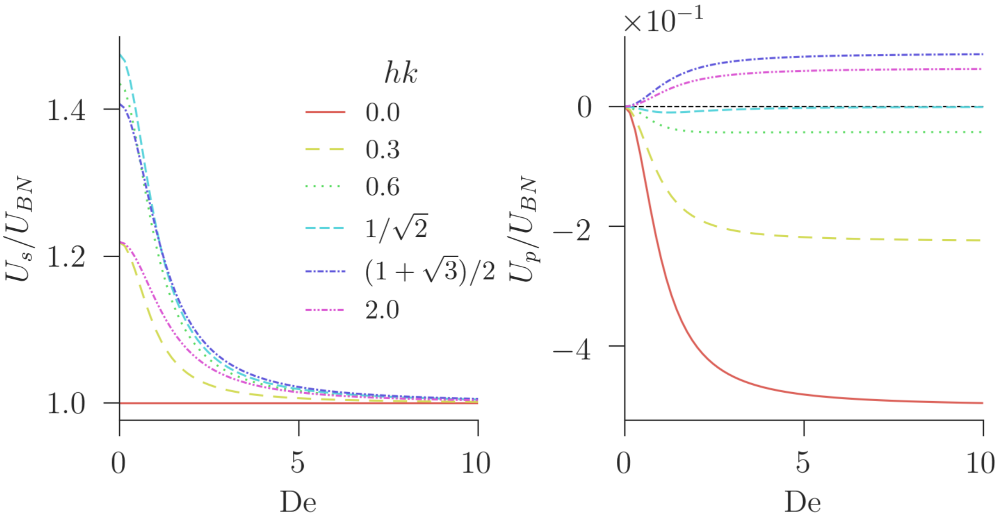

Figure 4.5 The two contributions U_s and U_p of the small-amplitude swimming speed U of a sheet in the depletion region of a viscoelastic fluid, of various thicknesses h as a function of Deborah number De. The viscosity ratio $\beta = 0.5$. The swimming speed contributions are scaled by the swimming speed of a sheet in the bulk of a Newtonian fluid. The plateau value of U_p changes sign at $hk = 1/\sqrt{2}$ and is maximum at $hk = (1+\sqrt{3})/2$.

of swimming. Thus when next to a wall, the advection term slows the sheet, just like the rotational term of Eq. (4.2d). When swimming in a depletion region, the polymers do not push the sheet; but instead push the entire depletion region. However, the vortices are still centred near the sheet. Thus, we are now pushing an object above the centreline of the vortices. As such, this advection term now pushes in the direction of swimming and speeds up the sheet. As a result, there is a competition between the rotational and advective terms. At small depletion region thicknesses, the advection term is negligible and swimming is hindered by the polymers; whereas for larger thicknesses, the advection term dominates and the sheet swims faster.

Figure 4.4 suggests that similar mechanisms are at play at finite amplitudes. For $\beta = 0.1$ and $hk = 0.6$, the swimming speed does not monotonically decrease with Deborah number. In fact, there is some minimum swimming speed $U_{\min} < U_\infty$ at around De $= 6.8$. This suggests that the soft-wall effect has been turned off before the polymeric contributions have been completely turned on. Moreover, there is a crossover from $U_\infty < U_{BN}$ to $U_\infty > U_{BN}$ at around $hk \approx 1/\sqrt{2} \approx 0.7$. Thus, we suggest that for real microswimmers, such as spermatozoa, and if there is some mechanism that creates a depletion region, then we would expect the swimming speed to be dominated by a soft-wall effect at low Deborah numbers;

and for polymeric contributions to swimming speed to dominate at large Deborah numbers.

If the mechanism responsible for the creation of the depletion region is the same as that which we outlined in Section 4.1.1, then we expect $h = b + R_g$, where R_g is the radius of gyration of the polymers in solution. Typically, $R_g \ll b$, thus we can take $h \approx b$ for a real swimmer. We expect that for such a swimmer, at low Deborah numbers, the swimming speed will be larger than the Newtonian swimming speed of the organism due to the soft-wall effect. This is the regime of the *E. coli* studied by Martinez et al. [19], where the Deborah number is $\mathrm{De} \approx 0.7$. As the Deborah number increases we expect the swimming speed to decrease, reaching a plateau. This plateau speed is either faster or slower than the Newtonian speed depending on the dimensionless wave-amplitude, bk of the swimmer. For *E. coli* $bk \approx 0.3$ [38], so we expect the high Deborah number swimming speed to be slower than the Newtonian swimming speed.

4.6 Conclusion

In this chapter, we have used Taylor's swimming sheet to model a flagellated microorganism swimming through a polymer solution, where there is some mechanism that creates a region surrounding the swimmer, which is depleted of polymer coils. We have shown, using small-amplitude analysis, that there are two physical mechanisms that affect the swimming of the sheet: (i) the interface between the depletion region and the rest of the fluid acts as a 'soft wall', speeding up the sheet; and (ii) there is a polymeric contribution to the swimming speed due to the interaction of the linear viscoelastic response to the local oscillatory shear with the vortices constituting the flow in the outer fluid. We have shown that at small Deborah numbers, mechanism (i) dominates; while at large Deborah numbers, mechanism (ii) dominates.

Numerical solutions to the problem suggest that these physical mechanisms are still important at finite amplitudes. We have also shown that, because the typical radius of gyration of a polymer coil is small when compared to the wave amplitude of a typical microswimmer, we expect small-amplitude flagellated microswimmers ($bk \lesssim 1/\sqrt{2}$) to swim more slowly in viscoelastic fluids at large Deborah numbers than in Newtonian fluids. Conversely, we expect large-amplitude flagellated microswimmers to swim faster at large Deborah numbers than in a Newtonian fluid. This shows very directly how important the exact kinematics of the swimmer are in determining their behaviour in viscoelastic fluids.

More experimental evidence is needed to know if flagellated microswimmers do indeed create depletion regions as they swim through polymer solutions. However, this model suggests that there should be separate regimes for the behaviour of microswimmers in polymer solutions based on their kinematics. This provides an experimental test for the existence of these depletion regions, which just involves the measurement of the swimming speed of flagellated microorganisms.

Chapter 5

Optimisation of microswimmers in Newtonian fluids

5.1 Introduction

In the previous chapters, we have developed a mechanistic understanding of the behaviour of Taylor's sheet swimming through a viscoelastic fluid in various situations. To develop this understanding we followed a procedure that is ubiquitous in the mathematical study of microswimmers. We prescribed some kinematics to the sheet and solved the appropriate fluid mechanical equations to find the properties of the swimmer we were interested in. However, the question remains: what is it that prescribes these kinematics in the first place?

The kinematics of biological microswimmers have been optimised by evolutionary processes and many studies [94–101] have mathematically optimised the swimming kinematics of various model microswimmers. It is tempting to compare the results of these mathematical optimisations with those of evolutionary optimisation processes. However, to make a fair comparison, we must ensure that the quantity being mathematically optimised for reflects the selection pressures the biological microswimmers experience.

When discussing evolution, the quantity that mathematically reflects these biological selection pressures is known as the fitness function. An organism exhibits many different traits, which are collectively known as the organism's phenotype. In general, the fitness function is a function of phenotype i.e. the entirety of the organism's traits. As its name would suggest, the value of the fitness function in some way measures the 'fitness' of that phenotype, that is, how likely an organism with that phenotype is to pass on their genes. If a set of traits are independent, then their contributions to the fitness function will factorise. In this case we can consider a fitness function for each of the traits independently. In this thesis, we are concerned with the swimming of microorganisms and so, naturally, we are going to assume that we can consider an independent fitness function for the trait of swimming.

In general, the 'swimming fitness function' depends on any number of observables used to characterise the organism's swimming. From a mathematical perspective, two of the most readily available such observables are the swimming speed U of the organism and the rate of work W done by the organism against the viscous forces in the fluid. There has been some debate about whether W is of any biological relevance. Purcell [3] has argued that the fitness function should not depend on W. He showed that for a typical microswimmer, the energetic cost of swimming is much smaller than the metabolic rate of the organism. That is, W is a small fraction of the organism's total rate of energy consumption. Thus, argues Purcell, the energetic cost of swimming is irrelevant.

In an endogenous metabolic state, where the cell conserves energy, Proteobacteria, such as *E. coli*, have an average metabolic rate of $R \approx 11\,\mathrm{W\,kg^{-1}}$ [102]. The power expended by the motor of an *E. coli* cell is $W \approx 10^{-16}\,\mathrm{W}$ [39]. This gives a ratio of the energetic cost of swimming to the minimum metabolic rate of $W/(RM) \approx 10^{-2}$, where $M \approx 10^{-15}\,\mathrm{kg}$ [103] is the mass of an *E. coli* cell. Similarly, *C. elegans* has a metabolic rate $R \approx 10\,\mathrm{W\,kg^{-1}}$ in the absence of food [104] and does work at a rate of $W \approx 10^{-12}\,\mathrm{W}$ [105]. Thus, we have $W/(RM) \approx 10^{-5}$, where $M \approx 10^{-8}\,\mathrm{kg}$ is an estimate of the worms mass assuming it has the same density as water. Purcell is therefore correct that these energy costs are small. However, it is not clear to us that this allows us to neglect W from the fitness function. Evolutionary processes occur over millions of years, and we cannot exclude the possibility that even small optimisations of the total energy consumption are made over these incredibly long timescales [106]. Even if we dismiss Purcell's argument, we still have to determine what the fitness function is, in order to make comparisons of mathematical optimisations to evolutionary processes.

If W is important, then a natural choice for the fitness function is the efficiency of the organism. The usual definition of efficiency is the ratio of the useful work done and the total energy spent. However, for a low Reynolds-number force-free swimmer, there is no clear way to define useful work. Microswimmers exploit drag anisotropy, i.e. their propulsive forces are 'drag' forces in the direction of swimming. It is difficult to separate these from the actual drag forces.

Lighthill [2] attempted to address this problem by defining a quantity known as the hydrodynamic efficiency $\mathcal{E}_H$. Lighthill compared W to the power P required by an external agent as it drags a 'frozen' copy of the organism at its swimming velocity $\boldsymbol{U}$. Due to the linearity of Stokes' equations, in a Newtonian fluid, the force $\boldsymbol{F}$ required to pull an object at a speed $\boldsymbol{U}$ depends linearly on $\boldsymbol{U}$. Thus, $P = \boldsymbol{F} \cdot \boldsymbol{U} = \eta\alpha U^2$ and we have

$$\mathcal{E}_H = \frac{\eta\alpha U^2}{W}, \tag{5.1}$$

where η is the viscosity of the fluid and α is some geometric factor specific to the swimmer. This quantity is not really an efficiency as it is possible to design swimmers with $\mathcal{E}_H > 1$ [107] and there have been some attempts [108] to define better measures of efficiency. However, $\mathcal{E}_H$ does provide a method of comparing swimming strategies via some reference problem. As such, there are many mathematical optimisations of model microswimmers using $\mathcal{E}_H$ as a fitness function throughout the literature [95, 96, 99–101, 109–111].

Although $\mathcal{E}_H$ may be of interest for an engineer designing an artificial microswimmer, it is not obvious that this 'efficiency' is of any biological relevance. Why should an organism be more likely to pass on its genes if it has a high $\mathcal{E}_H$? The fact of the matter is, the fitness function is largely unknown and depends on the selection pressures experienced by the organism in question. Without a detailed understanding of the organism's environment, we cannot *a priori* determine the fitness function we should be optimising.

In this chapter, we attempt to narrow down the possible fitness functions that can govern the evolution of microswimming. To do this, we perform a 'backward optimisation process'. That is, we find the optimal kinematics of a model swimmer for different trial fitness functions. We then compare the resulting optimal kinematics to the kinematics of biological microswimmers, which optimise the true fitness function. Based on how close the calculated optimal kinematics are to those of biological microswimmers, we can estimate how closely the trial fitness function matches the true fitness function. These backwards optimisations allow us to investigate the true fitness function without a detailed knowledge of the microorganism's environment.

Although there is an infinite number of trial fitness functions we could choose, we are going to look at the simplest class of functions and only consider power laws. Presumably, spending energy to swim lowers the fitness of an organism; whereas swimming more quickly increase an organism's fitness. Thus, we expect our fitness function $\Phi = \Phi(U, W)$ to be an increasing function of U and a decreasing function of W. As, for some real number b, the optima of Φ^b coincide with the optima of Φ, the most general power-law fitness function Φ_a is given by

$$\Phi_a = \frac{U^a}{W}. \tag{5.2}$$

Here, $a > 0$ controls how important it is to swim quickly compared to the cost associated with spending energy. In addition to being simple, this choice of Φ_a has the advantage that the optima of Φ_2 are the same as the optima of $\mathcal{E}_H$.

Assuming the true fitness function is of the form Eq. (5.2), the true value of a depends on the selection pressures relevant to the organism in question. As a increases, swimming quickly becomes more and more important. For example, the advantage associated with swimming for bacteria such as *E. coli* may be due to an increased consumption of food. In this case, we might expect a to be relatively small because if the organism spends too much energy swimming, it may not gain any benefit from consuming more food. Contrast this to spermatozoa, where the advantage of swimming is closely tied to the speed of swimming: whichever spermatozoon fertilises the egg passes on its genes. Thus we might expect a to be quite large, in that case.

Dimensional analysis shows that the generalised fitness function scales with the frequency, ω, of the swimmer's deformation as $\Phi_a \sim \omega^{2-a}$ and this is the only way in which time enters the problem. Thus, for $a > 2$, the fitness function increases with increasing frequency and conversely, for $a < 2$, the fitness function increases with decreasing frequency. This suggests that, for $a > 2$, any real swimmer will swim at the maximum frequency possible for its motor. Whereas, for $a < 2$, the organism would be best to not use its motor at all. For the rest of this chapter, we will be concerned with the optimal shape for an organism to make with its flagellum, given it has a fixed motor frequency. We will still consider the $a < 2$ case even though this simple dimensional analysis suggests it is unimportant, because it is useful in understanding the landscape of the problem.

In this chapter, we perform a backwards optimisation process using two model swimmers in low Reynolds-number Newtonian fluids: (i) Taylor's sheet and (ii)

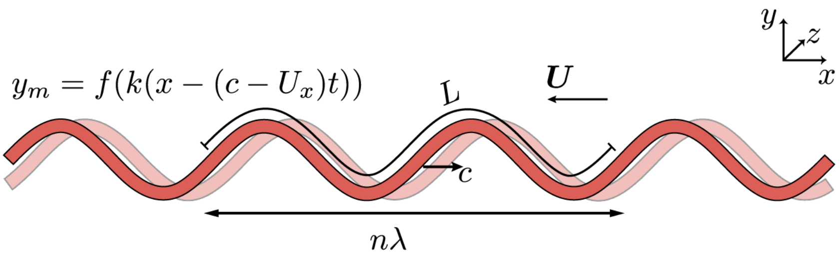

Figure 5.1 A schematic of a infinite flagellum propagating a wave with a wavelength $\lambda = 2\pi/k$, a wave speed c and a waveform f. The wave is travelling to the right and the faded image shows the flagellum at a later time. The schematic shows the relationship of this infinite flagellum to a finite n-period swimmer of length L.

an infinite flagellum model Lighthill optimised when he introduced Eq. (5.1). We now introduce these models.

5.1.1 The models

Both Taylor's waving sheet and Lighthill's infinite flagellum are inspired by planar-wave microswimmers such as spermatozoa and *C. elegans*. As such, the models share a common set of swimming kinematics, allowing for comparisons between the two.

As discussed in Section 1.1.3, Taylor's waving sheet is an infinite two dimensional sheet. In contrast, the flagellum is an infinite cylinder. Both swimmers propagate planar waves in the xy-plane in the positive x-direction at a speed c, resulting in a swimming velocity $\boldsymbol{U} = (U_x, U_y, 0)^T$. Both the sheet and the flagellum make a shape y_m in the xy-plane, which, at a time t, is given by

$$y_m(x,t) = f(k(x-(c+U_x)t)), \tag{5.3}$$

where f is the waveform and k the associated wavenumber. For the sheet, U_y vanishes and for both swimmers $U_x < 0$. Figure 5.1 shows this for the flagellum.

The key difference between these two models is the method used to calculate the associated swimming properties. For Taylor's sheet, we can solve the Stokes' equations surrounding the swimmer and use the solution to find the swimming properties. In this chapter, we use our spectral method solver, which allows us to find the swimming properties for any waveform f.

The flagellum has less symmetries than Taylor's sheet. Thus, finding the solution to the Stokes' equations in the surrounding fluid is more difficult than with the sheet. Instead, we follow Hancock [6] and Lighthill [2] and use resistive force theory. Resistive force theory exploits the linearity of Stokes' equations to approximate the hydrodynamics of the problem, by adapting the solution to a straight flagellum. Using this approach allows us to find analytical expressions for the swimming properties of the infinite flagellum.

These two models complement each other. The infinite flagellum model more closely resembles the biological microswimmers we wish to compare our models to. However, when finding the swimming properties, we neglect aspects of the flagellum's interactions with itself. Taylor's waving sheet can be solved without neglecting these aspects. This allows us to estimate how the neglected aspects of the hydrodynamic interaction might affect the flagellum. That being said, the sheet is only two-dimensional. This is a considerable difference from the biological swimmers we wish to model. The flagellum model tries to cover this deficiency.

Both the sheet and the flagellum are infinite. This makes them much simpler problems to solve than finite swimmers. However, their infinite size makes them poor candidates for doing optimisations of their kinematics, as neither model has a length scale independent of the kinematics. Also, due to their infinite sizes, the rate of work done by each swimmer diverges. As such, we can only find a rate of work per unit length or per unit area for the flagellum or sheet, respectively.

To avoid these problems, we propose the following. We consider a finite piece of each swimmer consisting of n periods of the wave, where n is an integer. The swimming speed U of this finite piece is the same as that of the infinite swimmer. Its rate of work W is found by integrating the appropriate quantity over the n periods of the wave. To perform optimisations, we fix the contour length L of the finite piece of the sheet and the angular frequency of the wave $\omega = ck$. Thus, the swimming kinematics that we optimise are entirely determined by the following: (i) the number of periods n, (ii) the wavelength $\lambda = 2\pi/k$ and (iii) the waveform f.

By fixing the contour length L, we are introducing a length to the problem allowing for optimisations. This is not necessary when optimising Φ_2, or equivalently $\mathcal{E}_H$, because, as we show below, these quantities are independent of any length scale. However, it is necessary for all other Φ_a, which do depend on the length scale. The fixed contour length imposes a constraint on the swimming kinematics given by

$$
\begin{aligned}
L &= \int_0^{n\lambda} \sqrt{1+f'(x)^2}\; dx, \\
&= n\int_0^{\lambda} \sqrt{1+f'(x)^2}\; dx = n\Lambda. \qquad (5.4)
\end{aligned}
$$

where Λ is the contour length of a single period of the waveform. Using this relationship, we introduce the length scale into the problem.

In Section 5.2, we repeat Lighthill's [2] calculations to find expressions for the swimming speed and rate of work per unit length of an infinite flagellum with arbitrary waveform, using resistive force theory. We combine these expressions with Eq. (5.4) to find expressions for the swimming speed and the rate of work of a finite length swimmer. We then find the swimming kinematics of this finite length swimmer that optimise Φ_a for different a. In Section 5.3, we outline how to use our numerical solver for Taylor's waving sheet in a Newtonian fluid. We demonstrate how to use this solver to find the swimming speed of a finite length swimmer. We then perform numerical optimisations of the finite piece of Taylor's sheet for various Φ_a. In Section 5.4, we compare the optimal kinematics we found to the swimming kinematics of biological microswimmers and discuss the implications this has on the true fitness function.

5.2 Optimising the kinematics of an infinite flagellum

Lighthill [112] used resistive force theory to show that the optimal waveform for $\Phi_2 \sim \mathcal{E}_H$ is a sawtooth wave. In this section, we provide an overview of Lighthill's calculations and show that this is still the case for all other Φ_a. We find the optimal wavelength λ^* of this sawtooth wave, as a function of the fitness function parameter a.

To calculate the swimming speed and rate of work of the flagellum in a Newtonian fluid, we must solve the Stokes' equations, which are given by

$$-\nabla p + \eta \nabla^2 \boldsymbol{u} = 0, \qquad (5.5a)$$

$$\nabla \cdot \boldsymbol{u} = 0, \qquad (5.5b)$$

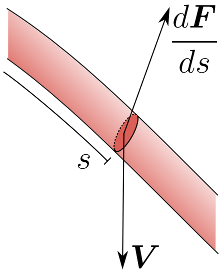

Figure 5.2 The drag force density $d\boldsymbol{F}/ds$ of a cross-section at a distance s along the flagellum is linearly related to its velocity $\boldsymbol{V}$.

where η is the fluid viscosity, p is the pressure field and $\boldsymbol{u}$ is the velocity field in the surrounding fluid. In addition to the Stokes' equations, we need the no-slip boundary conditions at the surface of the flagellum. These boundary conditions depend on the swimming kinematics in Eq. (5.3). Solving Eq. (5.5) with these boundary conditions for an arbitrary waveform f is difficult. We will instead approximate the problem using resistive force theory. This allows us to simplify the hydrodynamic interactions of the flagellum with itself.

5.2.1 Resistive force theory

Resistive force theory was originally developed by Gray & Hancock [113] to simplify the calculation of the swimming velocity of a flagellum moving through a Newtonain fluid. They ignore any contribution from the waveform to the hydrodynamic interaction of the flagellum with itself to make the problem more tractable. Using their analysis, Lighthill [2] found expressions for the swimming speed and rate of work for any waveform. Here, we give a brief overview of these calculations.

Consider a cross section of the flagellum at a distance s along its length. As the wave passes down the flagellum, the cross section will have some velocity $\boldsymbol{V}(s)$ and will experience some drag-force density $d\boldsymbol{F}/ds$ due to its motion through the fluid. A Newtonian fluid's stress tensor is linear in $\boldsymbol{u}$ and p. Therefore, at low Reynolds-numbers, $\boldsymbol{V}(s)$ and $d\boldsymbol{F}/ds$ are related linearly. We can express this linear relationship with a matrix equation

$$\frac{d\boldsymbol{F}}{ds}(s) = -\Xi \cdot \boldsymbol{V}(s), \tag{5.6}$$

where Ξ is the symmetric, positive-definite resistance matrix of the flagellum.

Although, Ξ is independent of $\boldsymbol{V}(s)$, it does depend on the velocities and positions of all the other cross-sections that make up the flagellum. Thus, Ξ depends on the waveform $f(x)$, which governs the position and velocity of the other cross-sections and the position s of the cross-section in question. Rather than exactly calculating Ξ for a general waveform, we approximate Ξ by ignoring its dependence on $f(x)$ and using the result for a straight flagellum (i.e. $f(x) = 0$), regardless of the actual waveform.

For the special case of $f(x) = 0$, it is relatively easy to calculate Ξ using a Green's function approach, see [2]. This Green's function calculation shows that the dependence of Ξ on s is very weak and the matrix has two unique eigenvalues $\xi_{||}$ and $\xi_{\perp}$ corresponding to motions parallel and perpendicular to the flagellum respectively. The $\xi_{\perp}$ eigenvalue is repeated twice as there are two equivalent directions perpendicular to the flagellum in the eigenbasis of Ξ. Ignoring their weak s-dependence, these eigenvalues are approximately given by

$$\begin{aligned} \xi_{||} &\approx \frac{4\pi\eta}{2\log(\frac{L}{R}) - 1}, \\ \xi_{\perp} &\approx \frac{8\pi\eta}{2\log(\frac{L}{R}) + 1}. \end{aligned} \tag{5.7}$$

As the motion of the flagellum is confined to the xy-plane, the z-components of $\boldsymbol{V}$ and $d\boldsymbol{F}/ds$ must vanish and we just consider their x- and y-components. It is easy to show, by considering a rotation from the $||\perp$-basis to the xy-basis, that Ξ is given by

$$\begin{aligned} \Xi =&(\xi_{||}\cos^2\theta + \xi_{\perp}\sin^2\theta)\boldsymbol{e}_x\boldsymbol{e}_x \\ &+(\xi_{||} - \xi_{\perp})\cos\theta\sin\theta(\boldsymbol{e}_x\boldsymbol{e}_y + \boldsymbol{e}_y\boldsymbol{e}_x) \\ &+(\xi_{\perp}\cos^2\theta + \xi_{||}\sin^2\theta)\boldsymbol{e}_y\boldsymbol{e}_y, \end{aligned} \tag{5.8}$$

where $\theta = \theta(s)$ is the angle the flagellum is making to the x-axis at a distance s along its length.

Now that we have our approximation for Ξ, consider again a flagellum with an arbitrary waveform $f(x) \neq 0$. From Eq. (5.8), the flagellum experiences a drag force density given by

$$\frac{dF_x}{ds} = V_y(\xi_\perp - \xi_\parallel)\sin\theta\cos\theta - V_x(\xi_\parallel\cos^2\theta\xi_\perp\sin^2\theta), \tag{5.9a}$$

$$\frac{dF_y}{ds} = V_x(\xi_\perp - \xi_\parallel)\sin\theta\cos\theta - V_y(\xi_\perp\cos^2\theta\xi_\parallel\sin^2\theta), \tag{5.9b}$$

where $V_{x,y}$ and $dF_{x,y}/ds$ are the x- and y-components of $\boldsymbol{V}$ and $d\boldsymbol{F}/ds$ respectively. In the frame of reference moving with the wave, the flagellum is moving tangentially backward along itself with a speed $Q = \frac{\Lambda}{\lambda}c$. Thus, the velocity $\boldsymbol{V}$ of the cross-section is the sum of this tangential motion and the motion of the organism as a whole due to the swimming velocity $\boldsymbol{U}$. These are given by

$$\boldsymbol{V} = (U_x + c - Q\cos\theta)\boldsymbol{e}_x + (U_y - Q\sin\theta)\boldsymbol{e}_y. \tag{5.10}$$

In order for the cross-section to move at a velocity $\boldsymbol{V}$, the internal mechanism of the flagellum must produce a force density equal and opposite to the local drag force density that the cross-section experiences. The organism cannot apply a net force to itself, thus for each period of the wave, we have the integral conditions

$$F_x = \int_0^\Lambda \frac{dF_x}{ds}ds = 0, \tag{5.11a}$$

$$F_y = \int_0^\Lambda \frac{dF_y}{ds}ds = 0. \tag{5.11b}$$

Here, $\boldsymbol{F} = (F_x, F_y, 0)^T$ is the total drag force the period of the wave experiences as it moves through the fluid. Using Eqs. (5.9) and (5.10), the integral conditions of Eq. (5.11) reduce to a pair of simultaneous equations in terms of $(U_x + c)$ and U_y which are both independent of s:

$$I_1(U_x + c) - I_3U_y = \lambda Q, \tag{5.12a}$$

$$-I_3(U_x + c) + I_2U_y = \quad 0. \tag{5.12b}$$

Here, $I_{1,2,3}$ are a set of integrals that depend on the waveform of the flagellum.

They are given by

$$I_1 = \int_0^\lambda \frac{1+\gamma f'(x)^2}{\sqrt{1+f'(x)^2}}\mathrm{d}x, \tag{5.13a}$$

$$I_2 = \int_0^\lambda \frac{\gamma + f'(x)^2}{\sqrt{1+f'(x)^2}}\mathrm{d}x, \tag{5.13b}$$

$$I_3 = \int_0^\lambda \frac{(\gamma-1)f'(x)}{\sqrt{1+f'(x)^2}}\mathrm{d}x, \tag{5.13c}$$

where $\gamma = \xi_\perp/\xi_\parallel$ is the flagellum's drag anisotropy. Here, we have used $\cos\theta ds = dx$ and $\tan\theta = f'(x-ct)$ and removed the formal time dependence as the integrands are periodic in $x - ct$.

Solving Eq. (5.11) for the swimming velocity, we find

$$\boldsymbol{U} = \frac{U_0}{n}\left\{\left(\frac{\lambda I_2}{I_1 I_2 + I_3^2} - \frac{\lambda}{\Lambda}\right)\boldsymbol{e}_x + \frac{\lambda I_3}{I_1 I_2 + I_3^2}\boldsymbol{e}_y\right\}, \tag{5.14}$$

where $U_0 = \omega L/2\pi$ is the characteristic speed of the piece of the flagellum. If $f'(x)$ is odd about some value of x, then I_3 vanishes and the organism swims purely in the x-direction with a speed, $U = |\boldsymbol{U}|$ given by

$$U = \frac{U_0}{n}\left(\frac{\lambda}{I_1} - \frac{\lambda}{\Lambda}\right). \tag{5.15}$$

To calculate the rate of work W, we exploit the fact that the flagellum is a force-free swimmer. We perform a Galilean transform to the frame of reference where the wave is stationary. In this frame, the cross-sections of the flagellum move tangentially along the length of the flagellum with a speed Q. They experience a drag force density in the tangential direction given by $dF_\parallel/ds = \xi_\parallel V_\parallel = \xi_\parallel(-Q + (c+U_x)\cos\theta + U_y\sin\theta)$. Thus, $dW/ds = -Q dF_\parallel/ds$; and the rate of work W is given by

$$W = \frac{\xi_\parallel U_0^2 L}{n^2}\left(1 - \frac{\lambda^2 I_2}{\Lambda(I_1 I_2 + I_3^2)}\right). \tag{5.16}$$

Figure 5.3 shows the swimming speed and rate of work of n periods of a sine-waving infinite flagellum.

With Eqs. (5.14) and (5.16), we have expressions for the swimming speed $U = |\boldsymbol{U}|$ and rate of work W in terms of the kinematic parameters n, λ and f. Here, we find the values of these kinematic parameters that optimise the trial fitness function

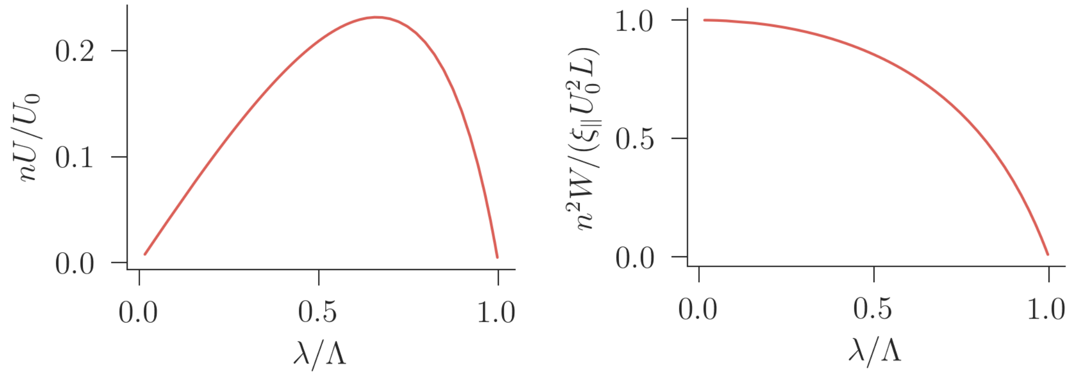

(a) Swimming speed **(b)** Rate of work

Figure 5.3 The swimming speed U and the rate of work W of n periods of an infinite sine-waving flagellum against wavelength λ. The finite piece of the flagellum has a length $L = n\Lambda$.

$\Phi_a = U^a/W$.

5.2.2 Flagellum optimisations

To find the functional form of f, we use calculus of variations. The dependence of U, W and thus, Φ_a on f is entirely contained in the integrals $I_{1,2,3}$. Each of these integrals is of the form

$$I_i = \int_0^\lambda \mathcal{L}_i(x, f(x), f'(x))\, dx. \tag{5.17}$$

For f to extremise I_i, it must satisfy, subject to appropriate boundary conditions, the Euler-Lagrange equation, given by

$$\frac{\partial \mathcal{L}_i}{\partial f} - \frac{d}{dx}\frac{\partial \mathcal{L}_i}{\partial f'} = 0. \tag{5.18}$$

For all i, $\mathcal{L}_i$ only depends on the gradient of the waveform f'. Thus, we can integrate Eq. (5.18), with respect to x, to find that $\partial\mathcal{L}_i/\partial f'$ must be a constant. As the only x-dependence of $\partial\mathcal{L}_i/\partial f'$ occurs via f', this can only be satisfied if f' is also a constant. Thus, the optimal waveform must be of the form $f(x) = Ax+B$ for all of the integrals. As the functional form of the optimal waveform for each of the integrals is the same, the optimal waveform for the swimming parameters U, W and Φ_a is also a straight line.

The waveform must satisfy periodic boundary conditions, i.e. $f(0) = f(2\pi) = 0$.

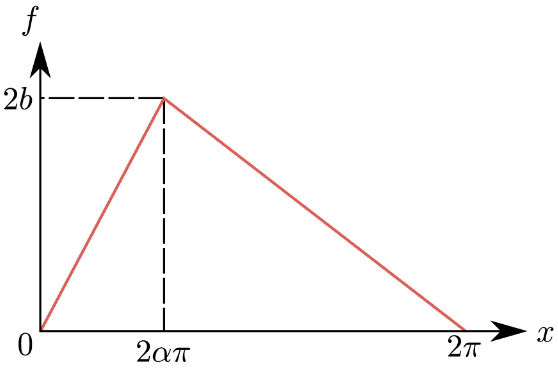

Figure 5.4 A schematic of a triangular waveform, f_{tri} with amplitude b and skew α.

For a straight line, this leads us to the only solution $f(x) = 0$ — a waveform that does not even swim! To obtain a non-trivial periodic solution, we construct a periodic waveform from straight pieces that each satisfy Eq. (5.18). There is not a unique way to do this, but we will consider the simplest such construction: a skewed triangular waveform $f_{\text{tri}}(x)$, with a skew α and an amplitude b, such that $f_{\text{tri}}(2\alpha\pi) = 2b$ as shown in Fig. 5.4. For $\alpha = 1/2$, this triangular waveform is the sawtooth wave found by Lighthill [112].

For the triangular waveform f_{tri}, the integrals in Eq. (5.14) can be computed piece-wise and are given by

$$I_1 = \Lambda \tilde{I}_1 = \Lambda \left(\frac{\alpha^2 \tilde{\lambda}^2 + 4\gamma \tilde{b}^2}{\sqrt{\alpha^2 \tilde{\lambda}^2 + 4\tilde{b}^2}} + \frac{(1-\alpha)^2 \tilde{\lambda}^2 + 4\gamma \tilde{b}^2}{\sqrt{(1-\alpha)^2 \tilde{\lambda}^2 + 4\tilde{b}^2}} \right), \tag{5.19a}$$

$$I_2 = \Lambda \tilde{I}_2 = \Lambda \left(\frac{\gamma \alpha^2 \tilde{\lambda}^2 + 4\tilde{b}^2}{\sqrt{\alpha^2 \tilde{\lambda}^2 + 4\tilde{b}^2}} + \frac{\gamma (1-\alpha)^2 \tilde{\lambda}^2 + 4\tilde{b}^2}{\sqrt{(1-\alpha)^2 \tilde{\lambda}^2 + 4\tilde{b}^2}} \right), \tag{5.19b}$$

$$I_3 = \Lambda \tilde{I}_3 = \Lambda \left(\frac{(\gamma - 1)\alpha \tilde{\lambda} \tilde{b}}{\sqrt{\alpha^2 \tilde{\lambda}^2 + 4\tilde{b}^2}} - \frac{(\gamma - 1)(1-\alpha) \tilde{\lambda} \tilde{b}}{\sqrt{(1-\alpha)^2 \tilde{\lambda}^2 + 4\tilde{b}^2}} \right), \tag{5.19c}$$

where $\tilde{\lambda} = \lambda/\Lambda$ is the dimensionless wavelength and $\tilde{b} = b/\Lambda$ $= 1/4\sqrt{(1-\tilde{\lambda}^2)(1-(1-2\alpha)^2\tilde{\lambda}^2)}$ is the dimensionless wave amplitude.

The swimming velocity $\boldsymbol{U}_{\text{tri}}$ and rate of work W_{tri} of the triangular waveform are given by

$$\boldsymbol{U}_{\text{tri}} = \frac{U_0}{n}\left\{\left(\frac{\tilde{\lambda}\tilde{I}_2}{\tilde{I}_1\tilde{I}_2+\tilde{I}_3^{\,2}} - \tilde{\lambda}\right)\boldsymbol{e}_x + \left(\frac{\tilde{\lambda}\tilde{J}}{\tilde{I}_1\tilde{I}_2+\tilde{I}_3^{\,2}}\right)\boldsymbol{e}_y\right\}, \tag{5.20a}$$

$$W_{\text{tri}} = \frac{\xi_{\parallel}U_0^2 L}{n^2}\left(1 - \frac{\tilde{\lambda}^2\tilde{I}_2}{\tilde{I}_1\tilde{I}_2+\tilde{I}_3^{\,2}}\right). \tag{5.20b}$$

The problem has a symmetry such that $\alpha \to 1-\alpha$ does not change the swimming speed, but only changes the sign of $U_{\text{tri},y}$ from positive for $\alpha > 1/2$ to negative for $\alpha < 1/2$. For the $\alpha = 1/2$ case, $U_{\text{tri},y}$ vanishes and the organism travels anti-parallel to the wave.

Before optimising the general Φ_a, let us consider the limiting case of $a \to \infty$, which corresponds to optimising U_{tri}. The bracketed terms in Eq. (5.20) depend only on the waveform's skew α and the dimensionless wavelength $\tilde{\lambda}$. The only n-dependence occurs in the prefactors. As n must be a natural number, the maximum swimming speed (or Φ_∞) occurs for $n^* = 1$. The swimming speed, U_{tri}, can be maximised algebraically with respect to α and λ giving

$$\alpha^* = \frac{1}{2}, \tag{5.21a}$$

$$\lambda^* = \sqrt{\frac{1+2\gamma-\sqrt{1+8\gamma}}{\Lambda}2(\gamma-1)}, \tag{5.21b}$$

$$\boldsymbol{U}_{\text{tri}}^* = -\frac{U_0\lambda^*}{\Lambda}\left(\frac{\sqrt{1+8\gamma}-3}{\sqrt{1+8\gamma}-1}\right)\boldsymbol{e}_x. \tag{5.21c}$$

In the limit of a very thin flagellum, $\gamma = 2$ and we have $\lambda^* \approx 0.662\Lambda$ and $U_{\text{tri}}^* \approx -0.238U_0$.

We can follow a similar procedure for optimising Φ_a for finite fitness function parameter a. Let us suppose there is some maximum number of periods $n_{\max}$ that a finite flagellum can support due to its mechanical properties, such as the maximum allowed curvature and the 'resolution' of the motor. As $\Phi_a \sim n^{2-a}$, we expect $n^* = n_{\max}$ for $a < 2$; and $n^* = 1$ for $a > 2$. In the exact case of $a = 2$, n^* is undetermined.

Analytically optimising Φ_a with respect to α and λ for an arbitrary a is not a tractable problem. Instead, we have performed the optimisations numerically for the $\gamma = 2$ case. We used the truncated Newton method of the `optimize.minimize` function from the `scipy` [114] Python package. For $a \leq 1$, we find that the optimal wavelength is given by $\lambda^* = \Lambda$ and $U^* = 0$. For

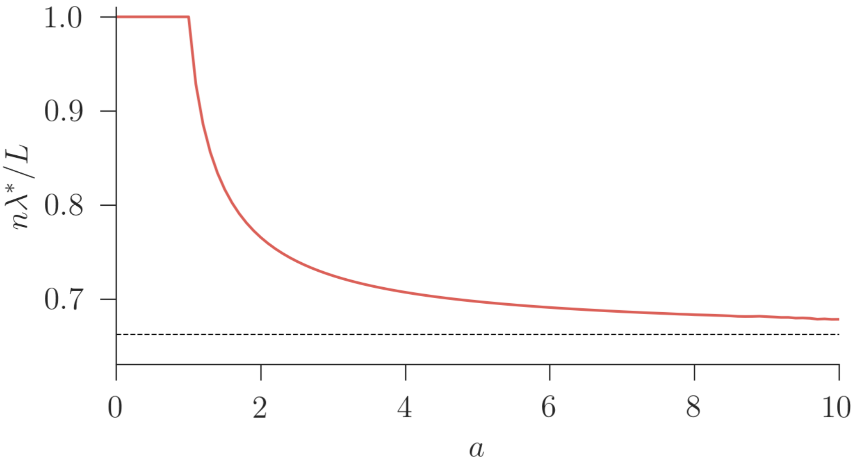

Figure 5.5 The optimal dimensionless wavelength λ^*, scaled by the contour length of a period Λ, against the fitness function parameter a for $\gamma = 2$. The dashed line is the dimensional wavelength of the fastest triangular waveform.

$a > 1$, we find that the optimal skew is $\alpha^* = 1/2$; and the optimal dimensionless wavelength decreases from $\lambda^* = \Lambda$ at $a = 1$, tending to Eq. (5.21b) as a increases — see Fig. 5.5.

To summarise, we find the following three regimes: (i) for $a \leq 1$, the optimal swimmer does not swim; (ii) for $1 < a < 2$, the optimal finite swimmer has $n_{\max}$ periods of a front-back symmetric triangular wave; and (iii) for $a > 2$, the optimal swimmer has one period of a front-back symmetric triangle wave. In all cases, when the finite piece of the flagellum swims optimally, it has a wavelength $\lambda > 0.662\Lambda$, which is the wavelength of the fastest swimmer.

In using resistive force theory to solve the flagellum model we have simplified the hydrodynamic interaction of the flagellum with itself. Although it is possible to modify the resistive force theory to more accurately model the hydrodynamic interactions of the waving flagellum, this quickly becomes unwieldy and we will instead use an alternative model swimmer which we can solve without approximating the hydrodynamic interactions.

5.3 Optimising the kinematics of Taylor's waving sheet

As mentioned in Section 5.1, Taylor's sheet is two dimensional, thus we must specify two dimensions when defining the finite piece of the sheet we will use to do the optimisations. We have already established in Section 5.1.1 that the finite piece of the sheet consists of n periods of the wave and has a fixed contour length L. In addition to this, the piece of the sheet has a depth d in the z-direction, so that it is a true finite swimmer.

To elucidate the distinction between the infinite sheet as a whole and the finite piece of the sheet, we will show how we can use Taylor's small-amplitude analysis of the infinite sheet to find small-amplitude expressions for the swimming speed and rate of work of the finite piece of the sheet.

When Taylor first proposed this model swimmer in 1951 [5], he considered a sine-waving sheet with waveform $f(x) = b\sin(x)$. He showed that for small bk, the infinite sheet swims with a velocity U given by

$$U_x = -c\left\{\frac{1}{2}b^2k^2 - \frac{19}{32}b^4k^4 + O(b^6k^6)\right\}. \tag{5.22}$$

The dimensionality of this expression comes from c, a quantity that depends on the swimming kinematics, which we want to optimise. To find the swimming speed where the dimensionality is independent of the kinematics, we first calculate the length of the piece using Eq. (5.4)

$$\begin{aligned} L &= \frac{n\lambda}{2\pi}\int_0^{2\pi}\sqrt{1 + b^2k^2\cos(kx)^2}\;dx, \\ &= n\lambda\left\{1 + \frac{1}{4}b^2k^2 - \frac{3}{64}b^4k^4O(b^6k^6)\right\}. \end{aligned} \tag{5.23}$$

We use this expression to replace c with a speed $U_0 = cL/\lambda$, which is a characteristic of the piece of the sheet and independent of the wave. This yields

$$U_x = -\frac{U_0}{n}\left\{\frac{1}{2}b^2k^2 - \frac{23}{32}b^4k^4 + O(b^6k^6)\right\}. \tag{5.24}$$

Calculating the rate of work of the swimmer is slightly more complicated than the swimming speed. As Taylor's sheet is infinite, we cannot calculate the *total* rate of work W — as this diverges. Instead, all we can calculate is the sheet's 'rate of work density' δW, which is the rate of work of a small piece of the sheet δA, given by

$$\delta W = \boldsymbol{u} \cdot \boldsymbol{\Sigma} \cdot \boldsymbol{n}_s|_{y=y_s} \, \delta A, \tag{5.25}$$

where $\boldsymbol{n}_s$ is the normal of the sheet and $\boldsymbol{\Sigma}$ is the total stress in the fluid.

However, for the piece of the sheet, the total rate of work W is finite and can be calculated by integrating δW over the surface area of the piece of the sheet, giving

$$\begin{aligned} W &= \int_0^d \mathrm{d}z \int_0^L \boldsymbol{u} \cdot \boldsymbol{\Sigma} \cdot \boldsymbol{n}_s|_{y=y_s} \, \mathrm{d}s, \\ &= nd \int_0^\lambda \boldsymbol{u} \cdot \boldsymbol{\Sigma} \cdot \boldsymbol{n}_s|_{y=y_s} \, \mathrm{d}x. \end{aligned} \tag{5.26}$$

Taylor [5] only calculated the integral in Eq. (5.26) to second order in bk. However, it is easy to extend his calculation to find W to the fourth order:

$$\begin{aligned} W &= n\eta c^2 d \left\{ 4\pi b^2 k^2 - \frac{3\pi}{2} b^4 k^4 + O(b^6 k^6) \right\}, \\ &= \frac{\xi_\parallel^{(s)} U_0^2 L}{n} \left\{ 4\pi b^2 k^2 - \frac{7\pi}{2} b^4 k^4 + O(b^6 k^6) \right\}, \end{aligned} \tag{5.27}$$

where $\xi_\parallel^{(s)} = \eta d/L$ is the 'resistance coefficient' of the sheet, performing a role analogous to $\xi_\parallel$ for the flagellum in the previous section.

Note the similarity between these expressions and that of the flagellum in Eqs. (5.14) and (5.16). The only difference in the dimensional prefactors is the dependence on the number of periods n for the flagellum (n^{-2}) and the sheet (n^{-1}). This is a consequence of the flagellum being a three dimensional swimmer, whereas the sheet is only two dimensional.

This analysis has just been for small-amplitude sine-waving sheets. In order to optimise the waveform, we need some scheme for calculating the swimming speed and rate of work for any waveform of arbitrary amplitude. For this, we use our spectral method solver to find the quantities numerically. We will outline this below in Section 5.3.1.

Although the numerical solver is applicable to a much more general situation than the small-amplitude analysis above, as we will see, the numerical solver gives the same scaling of the swimming speed and the rate of work as the small-amplitude analysis. That is, the way in which the numerical solution will differ from the small-amplitude solution is in the numerical value of the braced terms in Eqs. (5.24) and (5.27).

5.3.1 Finite-amplitude numerics

To find the swimming speed U_x and rate of work W of the sheet, we must first find the fluid velocity $\boldsymbol{u}(x, y)$ and the fluid pressure $p(x, y)$ in the fluid surrounding the model swimmer. We do this by solving the two dimensional version of the Stokes' equations Eq. (5.5), subject to no-slip boundary conditions at the sheet, which are given by

$$\boldsymbol{u}|_{y=y_s} = \boldsymbol{u}_s, \tag{5.28}$$

where $\boldsymbol{u}_s = (u_s, v_s)^T$ is the velocity of the material points of the sheet. We can then extract the swimming properties of the sheet from the solution in the fluid.

Here, we develop a numerical method to solve Eq. (5.5), subject to the boundary conditions Eq. (5.28) for an arbitrary waveform. Instead of solving the problem of the sheet in the bulk of the fluid, we solve the slightly more general problem of the sheet in a channel with walls above and below a distance h_+ and h_- from the centreline of the sheet, respectively. We take both h_+ and h_- to the same sufficiently large value, such that they do not influence the swimming speed and rate of work of the swimmer. We require additional no-slip boundary conditions at these walls. Thus, we have

$$\boldsymbol{u}|_{y=h_\pm} = \boldsymbol{u}_w, \tag{5.29}$$

where $\boldsymbol{u}_w = (u_w, v_w)^T$ is the velocity of the material points of the wall, which vanishes in this frame.

We start by simultaneously introducing dimensionless variables and removing any explicit time dependence with the help of the following transformations to daggered quantities

$$\begin{gathered} x^\dagger = k(x - (c + U_x)t),\ y^\dagger = ky,\ y_s^\dagger = ky_s,\ f^\dagger = kf,\ h_\pm^\dagger = kh_\pm, \\ U^\dagger = -\frac{U_x}{c},\ u^\dagger = 1 + \frac{U_x}{c} + \frac{u}{c},\ v^\dagger = \frac{v}{c}, \\ p^\dagger = \frac{p}{\eta c k},\ \boldsymbol{\Sigma}^\dagger = \frac{\boldsymbol{\Sigma}}{\eta c k}. \end{gathered}$$

In these coordinates the velocity of material points of the walls is given by $\boldsymbol{u}_w^\dagger = -(1-U^\dagger)\boldsymbol{e}_x$ and the shape of the sheet is fixed in time such that $y_s^\dagger(x^\dagger) = f^\dagger(x^\dagger)$. From now on we will drop the †s for clarity.

In this new coordinate system, Taylor [5] showed that the velocity of the sheet is given by

$$u_s(x) = -\frac{Q}{\sqrt{1+f'(x)^2}}, \tag{5.30a}$$

$$v_s(x) = -\frac{Qf'(x)}{\sqrt{1+f'(x)^2}}, \tag{5.30b}$$

$$\tag{5.30c}$$

where

$$Q = \int_0^{2\pi} \sqrt{1+f'(x)^2}\mathrm{d}x.$$

We find the swimming speed U and rate of work W from the solution $\boldsymbol{u}(x,y)$ and $p(x,y)$ via

$$U = \lim_{y\to\infty} u(x,y) - 1, \tag{5.31a}$$

$$W = \int_0^{n\lambda} \boldsymbol{u}\cdot\boldsymbol{\Sigma}\cdot\boldsymbol{n}\big|_{y=y_s}\mathrm{d}x, \tag{5.31b}$$

where $\boldsymbol{\Sigma}$ is the stress in the fluid.

To exploit the two-dimensional nature of the problem, we introduce a stream-function $\psi(x,y)$, which is defined via its relationship to the flow field $\boldsymbol{u}$: $u = \partial_y\psi$ and $v = -\partial_x\psi$. This substitution satisfies Eq. (5.5b) for any choice of ψ. To reformulate Eq. (5.5) in terms of the stream-function, we take the curl and divergence of Eq. (5.5a) to obtain the governing equations:

$$\nabla^4\psi = 0, \tag{5.32a}$$

$$\nabla^2 p = 0. \tag{5.32b}$$

The convergence properties of the Fourier-Chebyshev basis are optimal in rectangular domains [77], so we perform two independent coordinate transformations (one for the fluid above the sheet and one for the fluid below) which project the corresponding domains onto periodic rectangular strips. These transformations from the original coordinates (x, y) to the new ones $(\eta_\pm, \xi_\pm)$ are given by

$$\eta\pm = kx, \tag{5.33a}$$

$$\xi_\pm = 1 - 2\frac{y \mp h_\pm}{f(x) \mp h_\pm}, \tag{5.33b}$$

where "+" and "−" denote the regions above and below the sheet respectively. In each domain, $\xi_\pm = 1$ corresponds to the domain's wall, while $\xi_\pm = -1$ corresponds to the sheet, i.e. the lower domain has been flipped. The two domains can be treated equivalently and from now on we will drop the ± unless it is necessary.

In each deformed domain $(\eta, \xi) \in [0, 2\pi) \times [-1, 1]$, the fields are represented by truncated Fourier-Chebyshev series. For example, the steam-function ψ is given by

$$\psi(\eta, \xi) = \sum_{n=0}^{N-1} \sum_{m=0}^{M-1} \psi^{(nm)} F_n(\eta) T_m(\xi), \tag{5.34}$$

where $T_m(\xi) = \cos(m \arccos(\xi))$ is the mth Chebyshev polynomial, and

$$F_n(\eta) = \begin{cases} \sin(\frac{n+1}{2}\eta) & n \text{ odd} \\ \cos(\frac{n}{2}\eta) & n \text{ even,} \end{cases}$$

is the nth Fourier mode. We choose the resolution (N, M) such that the error on the swimming speed is less than 0.5%. When performing the optimisations in this chapter, this required resolutions of $N = 137$ and $M = 60$.

We construct matrices, which, when multiplied with vectors of the coefficients in Eq. (5.34), produce the coefficients of the spatial derivatives, ∂_x and ∂_y, of the field. In each domain, these matrices are given by

$$\left(\frac{\partial}{\partial x}\right)_\pm = \frac{\partial}{\partial \eta_\pm} + (\xi_\pm - 1)\frac{f'(\eta_\pm)}{\pm h_\pm - f(\eta_\pm)}\frac{\partial}{\partial \xi_\pm}, \tag{5.35a}$$

$$\left(\frac{\partial}{\partial y}\right)_\pm = \frac{2}{\pm h_\pm - f(\eta_\pm)}\frac{\partial}{\partial \xi_\pm}. \tag{5.35b}$$

where ∂_η and ∂_ξ are represented by the Fourier-Chebyshev spectral derivative matrices [77–79]. To calculate products of the fields represented in the spectral space, we use a Fast Fourier transform [78] technique, using collocation points given by,

$$\eta_{n_c} = \frac{2\pi n_c}{N_c}, \tag{5.36a}$$

$$\xi_{m_c} = \cos\left(\frac{\pi m_c}{M_c - 1}\right), \tag{5.36b}$$

Here, $n_c \in [0, N_c)$, $m_c \in [0, M_c)$ and the collocation resolution (N_c, M_c) is selected to satisfy $N_c > 1.5N$ and $M_c > 1.5M$ in order to avoid aliasing issues [77, 78].

Representing the two governing equations in Eq. (5.32) in the truncated Fourier-Chebyshev basis for each fluid domain yields a set of $4NM$ linear algebraic equations which need to be complemented by boundary conditions. By using Fourier modes, we have implicitly imposed periodic boundary conditions in the η-direction, which correctly reflects the symmetry of the underlying problem. We still need, however, six boundary conditions (four for ψ and two for p) along the lines $\xi = \pm 1$. These boundary conditions are expanded in the Fourier basis (as they are functions of η), generating $12N$ discretised boundary conditions to substitute into the original set of $4NM$ discretised governing equations.

We have a different set of boundary conditions for the $n \neq 0$ case than from the $n = 0$ case, because the $n = 0$ Fourier modes are in the null space of the x-derivative operator and the unknown swimming speed U appears in the $n = 0$ mode of u_w. For the $n \neq 0$ modes, we have the no-slip boundary conditions at the sheet and wall, which are given by given by

$$\partial_y \psi|_{\xi=-1} = u_s, \tag{5.37a}$$

$$-\partial_x \psi|_{\xi=-1} = v_s, \tag{5.37b}$$

$$\partial_y \psi|_{\xi=1} = U - 1, \tag{5.37c}$$

$$-\partial_x \psi|_{\xi=1} = 0. \tag{5.37d}$$

In addition, we fix the divergence- and curl-free terms in the solutions to Eq. (5.32), by requiring that $\boldsymbol{n} \cdot \nabla \cdot \boldsymbol{\Sigma} = 0$ at both the sheet and the wall, where $\boldsymbol{n}$ is the inward normal to the given surface. This yields

$$\Big[f'(\eta)\partial_x p - \partial_y p - (f'(\eta)\partial_y + \partial_x)\nabla^2\psi\Big]_{\xi=-1} = 0, \tag{5.38a}$$

$$\Big[\partial_y p + \partial_x \nabla^2 \psi\Big]_{\xi=1} = 0, \tag{5.38b}$$

where $(0, -1)^T$ is the normal to the wall, and $(-f'(\eta), 1)^T$ the normal to the surface of the sheet.

For the $n = 0$ mode, we set the constant terms of ψ and p to arbitrary values and we require there is no average x-force applied to the walls. We couple the two domains by requiring that: (i) the swimming calculated in each domain is the same; and (ii) there is no net force applied to the sheet. Thus, we have

$$p|_{\xi=1} = 0, \tag{5.39a}$$

$$\psi|_{\xi=1} = 0, \tag{5.39b}$$

$$(\partial_{xx} - \partial_{yy})\psi|_{\xi=1} = 0, \tag{5.39c}$$

$$\begin{aligned} &\left[f'(\eta_+)p_+ - 2f'(\eta_+)\partial_{xy}\psi_+ - (\partial_{xx} - \partial_{yy})\psi_+\right]_{\xi_+=-1} - \\ &\left[f'(\eta_-)p_- - 2f'(\eta_-)\partial_{xy}\psi_- - (\partial_{xx} - \partial_{yy})\psi_-\right]_{\xi_-=-1} = 0, \end{aligned} \tag{5.39d}$$

$$\partial_y\psi_+|_{\xi_+=1} = \partial_y\psi_-|_{\xi_-=1}, \tag{5.39e}$$

where the absence of a ± implies that the boundary condition applies to both domains.

The waveform $f(x)$ influences the construction of the matrices representing ∂_x and ∂_y via the transformation in (5.33) and via the boundary conditions outlined. With this we can then completely solve the swimming problem for any waveform provided we have a large enough resolution (N, M). From this solution we can then find the swimming properties, i.e. the swimming speed and rate of work. We use this solver to optimise the swimming sheet's waveform using numerical optimisation routines.

For each Fourier mode we replace the four highest Chebyshev modes of the discretised Eq. (5.32a) and the two modes of Eq. (5.32b) with the boundary conditions presented above. Combining everything together leads to the set of $4NM$ discretised equations, with the structure outlined in Table 5.1.

We solve the linear set of equations outlined in Table 5.1 to find the spectral representation of the flow field $\boldsymbol{u}$ and pressure field p. With the flow and pressure fields, we can find the swimming speed and rate of work using Eq. (5.31) to find

	$n = 0$	$0 < n < N$
$0 \leq m < M - 4$	Equations (5.32a) and (5.32b)	Equations (5.32a) and (5.32b)
$m = M - 4$	Equation (5.39d)(+) (5.39e)(−) Equation (5.32b)	Equation (5.37d) Equation (5.32b)
$m = M - 3$	Equation (5.39c) Equation (5.32b)	Equation (5.37c) Equation (5.32b)
$m = M - 2$	Equation (5.39b) Equation (5.39a)	Equation (5.37b) Equation (5.38b)
$m = M - 1$	Equation (5.37a) Equation (5.38a)	Equation (5.37a) Equation (5.38a)

Table 5.1 An outline of how the $4NM$ discretised equations are constructed from the differential equations in Eq. (5.32) and the various boundary conditions Eqs. (5.37) to (5.39).

the braced terms in Eqs. (5.24) and (5.27), giving

$$U = \frac{U_0}{n} \left\{ \frac{1 + \langle \partial_y \psi|_{\xi=1} \rangle}{2\pi \langle \sqrt{1 + f'(\eta)^2} \rangle} \right\} \tag{5.40a}$$

$$W = \frac{\xi_{\parallel}^{(s)} U_0^2 L}{n} \left\{ \frac{\sum_{\pm} \langle \boldsymbol{u}_\pm \cdot \boldsymbol{\Sigma}_\pm \cdot \boldsymbol{n}_\pm|_{\xi_\pm=-1} \rangle}{\langle \sqrt{1 + f'(\eta)^2} \rangle}, \right\} \tag{5.40b}$$

where $\langle ... \rangle$ is an average over x, $\boldsymbol{n}_\pm$ is the normal to the sheet and $\sum_\pm$ represents a sum over both domains. Due to the boundary conditions we imposed, Eq. (5.40a) gives the same result regardless of which domain is used.

Figure 5.6 shows the swimming speed and rate of work as calculated by the spectral solver for the waveform $f(x) = b \sin(x)$. The numerical results are compared to the 500 non-zero terms of the Taylor expansion for the swimming speed of the sheet found by Sauzade et al. [53] as discussed in Section 1.1.3. The numerical results agree with the analytical expression, demonstrating that our numerical solver is correct.

We can use Eq. (5.40) to calculate $\Phi_a = U^a/W$ for the finite piece of the swimming sheet with any wave propagating along its length. With this, we can now perform optimisations.

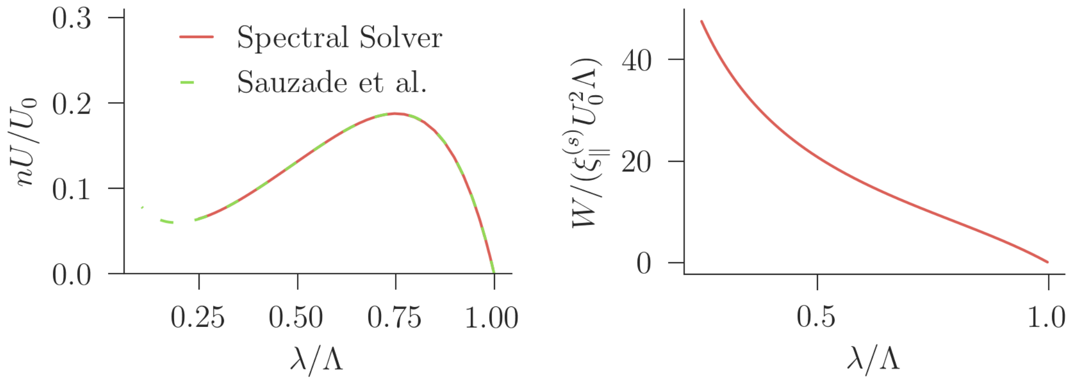

(a) Swimming speed **(b)** Rate of work

Figure 5.6 The swimming speed U and the rate of work W of a n periods of a sine-waving sheet with waveform $f(x) = b\sin(x)$ against wavelength λ. The swimming speed is compared to the swimming speed found by Sauzade et. al [53] by calculating the first 500 terms of the small-amplitude expansion. The resolution required to get an accuracy of 0.5% for the smallest wavelengths is $N = 61$, $M = 120$.

5.3.2 Taylor's sheet optimisations

There are two sets of parameters controlling the swimming kinematics that we can optimise for: (i) the number of periods of the wave n, which only appears in the prefactors of Eq. (5.40) and; (ii) the waveform $f(x)$ and wavelength λ, which only appear in the braced terms of Eq. (5.40). As these two sets of parameters are separable, we can optimise them independently.

Firstly, let us consider optimising with respect to n. Let us assume, as we did with the flagellum, that there is some n_{max} that the piece of the sheet can support. Then, as $\Phi_a \sim n^{a-1}$, for $a < 1$ we have $n^* = n_{\text{max}}$; and for $a > 1$ we have $n^* = 1$. Also, if we optimise just the swimming speed, we have $n^* = 1$.

For optimising the waveform $f(x)$, we need to use the spectral method solver to calculate the velocity and pressure fields of the fluid surrounding the sheet. We can then calculate the braced terms in Eq. (5.40), using these fields. We represent the waveform $f(x)$ as a truncated Fourier series with m modes, i.e.

$$f(x) = A_1\sin(x) + \sum_{p=2}^{m}(A_p\sin(px) + B_p\cos(px)), \tag{5.41}$$

where we have set $B_1 = 0$ without loss of generality due to the translational invariance of the problem along the x-axis. We also require $A_1, A_2 > 0$, again without loss of generality, due to the reflectional symmetry about the x-axis and

y-axis respectively. As m increases, we are exploring a larger function-space with our optimisations and thus, the waveforms we find will be closer to the true optimal waveform.

For the numerical optimisation of Φ_a, we successively increase m starting from 1 and using the $(m-1)^{\text{th}}$ optimal as a starting point for the m^{th} optimisation. We used the `L-BFGS-B`[115] algorithm of the `optimize.minimize` function in the `scipy` [114] `python` library to do the numerical optimisations. We perform the optimisations at increasing resolution (N, M), until the coefficients of the optimal waveform and the value of the optimum do not change by more than 0.5% between the highest resolutions.

We find that when optimising Φ_a, all the B_p modes and the A_{2q} modes vanish, for any choice of a. Unfortunately, we also found that for $m > 9$, the resolutions required for the spectral method solver to be able to resolve the optimal waveform were too large for optimisation to be feasible. This is due to the slow decay of the A_{2q+1} components of the optimal waveforms, which make the flow field difficult to resolve.

Figure 5.7 shows the wavelength of the optimal waveforms of the piece of the sheet for $m = 1, 5, 9$ as a function of the optimisation parameter a. Similarly to the flagellum, for $a < 1$, the optimum wave has a wavelength $\lambda^* = \Lambda$ and $U^* = 0$. And again similarly to the flagellum, for $a > 1$, the optimal wavelength decreases with a. However, unlike the flagellum where the optimal waveforms are the same shape for all a, there is a transition in the shape of the optimal waveform at $a = 2$ when optimising the sheet.

Figure 5.8 shows this ‘shape-transition’ from an approximate sine wave to a cusped waveform. This cusped waveform is similar to that found by Montenegro-Johnson et al.[111] when they performed an optimisation of a quantity equivalent to Φ_2 for a waving sheet using a boundary-element method. Their solver does not suffer from the resolution issues we face in resolving the optimal waveform and they were able to find the first 30 non-zero modes of the optimal waveform, which corresponds to $m = 61$. The shape they found is also a cusped waveform, similar to that which we find for $a \geq 2$.

Now that we have determined the optimal swimming kinematics for both the flagellum and the sheet, we compare them to the kinematics of biological swimmers.

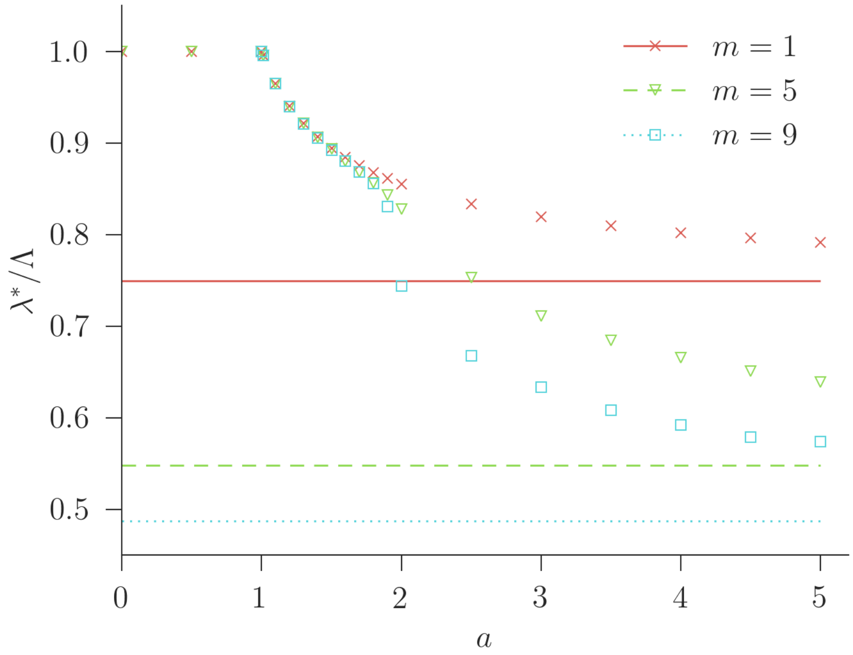

Figure 5.7 The optimal wavelength λ^* for a piece of a swimming sheet of length $L = n\Lambda$ when optimising for the fitness function Φ_a. The waveform is constrained to a truncated Fourier basis with m modes, as described in Eq. (5.41). The horizontal lines are the optimal wavelengths when optimising for the swimming speed. As $a \to \infty$, we expect the optimal wavelength when optimising Φ_a to tend to these swimming speed values. Unfortunately, we were unable to obtain results for larger m, and so the results are not converged for larger a. However, the results clearly show a transition at $a \approx 2$.

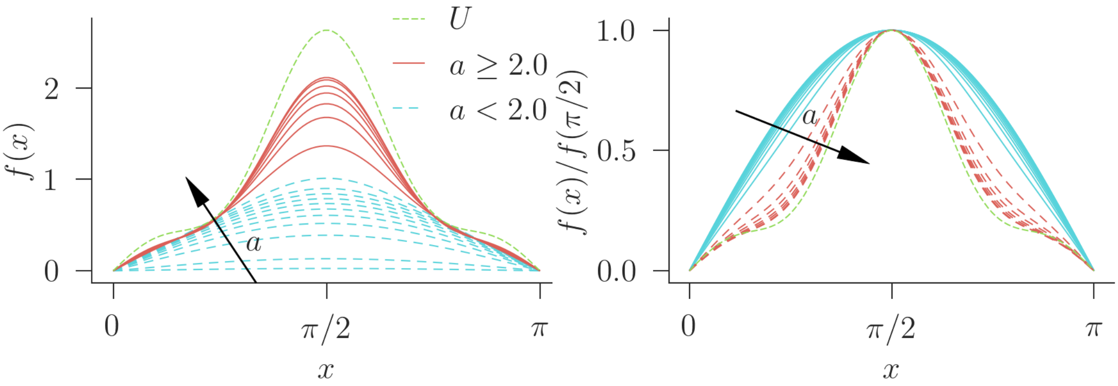

(a) Waveforms **(b)** Normalised waveforms

Figure 5.8 The sheet waveforms and normalised waveforms with $m = 9$ that optimise Φ_a for $0 \leq a \leq 5.0$ and U. For $a \geq 2.0$, the optimal waveform transitions from an approximate sine wave to a so-called cusped wave. Each wave corresponds to a point on the $m = 9$ line in Fig. 5.7 with a increasing as indicated by the arrows.

5.4 Discussion

The purpose of doing the optimisations above was to gain information about the true swimming fitness function for a microswimmer. In considering the results, and how they might be compared to the kinematics of biological swimmers, we need to mindful of the limitations of the models we have used. As discussed in Section 5.1.1, Taylor's waving sheet is a two dimensional object, which, as we have seen, has consequences for the prefactors to the swimming speed and rate of work. Also, recall that to solve the flagellum problem we had to make approximations to the hydrodynamic interactions of the flagellum with itself. In this section, we will try to show how using these two models allows us to compensate for their respective deficiencies.

The flagellum model predicts that the optimum waveform for a planar wave swimmer, which is optimising any fitness function of the form Φ_a, is a sawtooth wave. This is the same as the optimum waveform Lighthill found when optimising $\mathcal{E}_H$. At the vertex of the sawtooth, there is an infinite curvature, which a real flagellum could, in all likelihood, not support. To the author's knowledge, there are no biological planar wave swimmers with triangular waveforms. Observations of both sea-urchin spermatozoa [4] and nematodes, such as *C. elegans* [48], show waveforms with much more gentle curvatures, suggesting that they are not even attempting to approximate a triangular waveform. This might suggest that the true fitness function does not have the form of Φ_a.

However, before we jump to this conclusion, we should consider whether this apparent deficiency can be explained by the approximations used to solve the model, namely the approximations to the hydrodynamic interactions of the flagellum with itself. Recall that to solve the flagellum model, we used resistance coefficients when working out the force density along the length of the flagellum. Crucially, these coefficients were calculated for a straight flagellum. However, proximity of the flagellum to itself will affect these coefficients. This is the aspect of the hydrodynamics that our model neglects. Near the apex of the triangular waveform, cross-sections of the flagellum are closer to each other than they would be if the waveform was smooth. Thus, including these neglected aspects of the hydrodynamics might remove the high curvature parts of the optimum waveform. Our optimisations of Taylor's waving sheet show just that.

The optimum waveform for Taylor's waving sheet is either: (i) for $a < 2$, approximately a sine wave; or (ii) for $a \geq 2$, a cusped waveform similar to that found by Montenegro-Johnson et al. [111] when optimising the sheet for Lighthill's efficiency $\mathcal{E}_H$. Thus, including these aspects of the hydrodynamics regularised the high curvature point of the triangular wave. The cusped waveform in (ii) is just as unlike the observed waveforms of biological microswimmers. In contrast, the observed waveforms of these swimmers is far more similar to the approximate sine waves found in (i). We could therefore conclude that, for the true fitness function, $a < 2$. Importantly $a \neq 2$, which suggests that the swimming kinematics of these biological microswimmers do not extremise $\mathcal{E}_H$.

This argument is furthered if we consider the optimum wavelengths predicted by both models. Firstly, recall that for $a \leq 1$, both models predicted that $\lambda^* = \Lambda$ and that $U^* = 0$. Thus, if the true fitness function has $a \leq 1$, then the organisms would not have evolved to swim. Therefore, we conclude that $a > 1$. So far, we have determined that, for most planar wave swimmers, $1 < a < 2$. Let us use the wavelengths of some real microswimmers to determine which Φ_a most closely resemble the true fitness function for said organisms.

Brokaw [41] has observed that the flagellum of the spermatozoa of the tunicate *Ciona intestinalis* propagates $n \approx 1.3$ periods of a wave with a wavelength of $\lambda \approx 0.73L \approx 0.95\Lambda$. To obtain these wavelengths for the flagellum model, we require $a \approx 1.05$; and for Taylor's sheet, we require $a \approx 1.15$. Sznitman et al. [48] have observed that *C. elegans* propagates $n \approx 0.5$ periods of a wave with a wavelength λ, that is very close to Λ, suggesting that if the true swimming fitness function of *C. elegans* has the form Φ_a then a is close to unity. This suggests (if we just consider the shapes of the organisms) that for both of these swimmers, which live in very different environments, the energy used by these organisms as they swim is an important factor in the selection of the swimming kinematics.

This is in contradiction with the dimensional analysis we performed at the start of the chapter, involving the frequency of the organisms motion. There we found that only $a > 2$ leads to swimming being favourable over not swimming. This contradiction suggests that the true fitness function may not be of the form $\Phi_a = U^a/W$. As we are unable to reconcile the spatial optimisation with the temporal.

Also notice how, for both the organisms study by Brokaw, n is small. Recall that our optimisations of n found that n is small when $a > 1$ for Taylor's sheet and $a > 2$ for the flagellum. The difference between Taylor's sheet and the flagellum model is purely due to the difference in dimensionality between the two models. While Taylor's sheet is two-dimensional, the flagellum model is three-dimensional, just like real swimmers. As a result, we can dismiss the Taylor's sheet optimisation of n; and conclude that the small n observed for biological microswimmers corroborates our findings that $a > 2$.

This is a contradiction to the other two aspects of the kinematics, which predict that $1 < a < 2$. This contradiction can be caused by any of following three reasons: (i) the true fitness function is not of the form Φ_a; (ii) $n_{\max}$ is small for the spermatozoa flagellum and *C. elegans*; or (iii) the sheet and the flagellum are poor models for the biological microswimmers we are considering. Without further investigation, we cannot distinguish between these two situations. However, the parameter n only enters the problem via the introduction of our fixed length scale L; and as we have seen, the dependence of Φ_a on n is purely from the dimensionality of the problem. In using infinite swimmers, we are missing key aspects as to how n influences the swimming behaviour.

In fact, there is a deficiency common to both of these models because they are both infinite. That is, neither of these model swimmers is torque-free because torque is not a well defined quantity for the infinite models. However, we would expect a finite swimmer to rotate in order to minimise the torque it experiences. This effect will be more pronounced for shorter swimmers, meaning swimmers with a smaller n [97]. Due to this rotation, the organism will expend energy not accounted for in our calculations. Pironneau and Katz [98] have performed optimisations of the kinematics of a finite torque-free flagellum. When optimising $\mathcal{E}_H$, they find a sawtooth wave with $n = 1$ is optimal. In contrast the scaling analysis for an infinite flagellum shows that $\mathcal{E}_H$ is independent of n. Therefore, the n-dependence of Φ_a for these infinite model swimmers is a poor approximation to that of a proper finite torque-free swimmer. Further study is required to ascertain whether the use of finite model swimmers can reconcile the fitness function parameter a suggested by optimum n with the those suggested by optimum f and λ.

These infinite models also fail to capture the energetic cost in building and maintaining a flagellum. Flagella are complex organelles which are very energetically costly to produce, and as such their production is very heavily regulated by the cell[116]. In using these infinite models, we have neglected the length of the flagellum completely. For a finite cell, there will be a trade off between the costly process of producing the flagellum and the benefits afford the organism from swimming. This trade off cannot be investigated can only be investigated using more sophisticated finite model swimmers.

Despite these shortcomings, hopefully, our work can serve as a starting point for others to investigate the aspects we were unable to account for in more detail.

5.5 Conclusion

In this chapter, we have investigated how the kinematics of a microswimmer are chosen in a Newtonian fluid. Specifically, we looked at the role of the energetics of a microswimmer in this process.

We did this by performing a backwards optimisation process using Φ_a as a trial fitness function. The parameter a controls the importance of the swimming speed compared to the energetics. We compared the optimal kinematics predicted by the optimisation of Φ_a to the kinematics of biological microswimmers. Provided that the true fitness function of these microswimmers is of the form Φ_a, we were able to conclude that for most planar swimmers, generally $1 < a < 2$; but more specifically, for *C. elegans* and the spermatozoa of *C. intestinalis*, a is only slightly greater than unity. This suggests that, contrary to what Purcell [3] claimed, while small, the energetics required to swim are likely to play a role in the evolutionary selection of swimming kinematics. Additionally, this leads us to believe that Lighthill's efficiency, which shares optima with Φ_2, does not represent how the energetics of the organism are valued by evolutionary processes.

Although this chapter is inconclusive on the issue and more work is required with more sophisticated models, it does demonstrate the importance of carefully selecting an appropriate fitness function to optimise if one intends to use these optimisations as metaphors for evolution.

Chapter 6

Conclusions

In this thesis, we have investigated the swimming of microorganisms in complex fluids. Specifically, we have examined a simple model swimmer, Taylor's waving sheet, swimming through a fluid governed by the Oldroyd-B equations. We have developed a mechanistic understanding of the behaviour of this swimmer in a number of situations.

We have shown that when swimming in the bulk of the fluid, Taylor's waving sheet can be understood as an oscillatory sheer probe. At small wave amplitudes, the linear viscoelastic response to the local oscillatory sheer interacts with the vortices created by the sheet. Due to the topology of the vortices, this slows the sheet down. At large Deborah numbers, the viscoelastic agents in the fluid do not have time to react to the local oscillatory sheer and just behave elastically with a constant storage modulus. This results in a plateau swimming speed. We have demonstrated that this mechanism is still present at moderate wave amplitudes, albeit with more complicated non-linear viscoelastic responses. Thanks to this understanding, we have also been able to conclude that this mechanism should occur for any planar-wave swimmer. Thus, we suggest that this mechanism also explains the observations made by Shen and Arratia [20] of the nematode *C. elegans*.

We then extended this mechanism to swimming next to a wall. We showed that, broadly speaking, the same processes occur — except that in this situation, the vortices created by the sheet are faster. We further demonstrated that when close to the wall and at moderate amplitudes, the non-linear viscoelastic responses in the fluid could lead to non-monotonic swimming speeds, as a function of Deborah number. Further research is required to understand the exact origin of this non-monotonicity.

We also investigated the effects of viscoelasticity on the semi-continuum depletion-region model proposed by Martinez et al. [19]. We showed that at small Deborah numbers, the swimming behaviour is dominated by a soft-wall effect, which speeds the sheet up. But at large Deborah numbers, it is the interaction of the viscoelastic response with the vortices that dominates swimming behaviour. The presence of the depletion region means that this interaction can either speed the sheet up or slow it down. We demonstrated that due to the relative size of polymer coils in comparison to typical wave amplitudes, small-amplitude swimmers will be hindered at large Deborah numbers; whereas larger-amplitude swimmers will be helped. This shows how the kinematics of the swimmer can affect its qualitative behaviour in viscoelastic fluids.

Finally, we investigated the evolutionary process, which selects the kinematics of swimmers in Newtonian fluids. We showed that care must be taken when selecting the fitness function to optimise for. We also suggested that hydrodynamic efficiency is not a quantity relevant to biological swimmers. However, more work is required to truly understand how swimming kinematics are selected. The next step should include optimisations of microswimmers in complex fluids, as these are largely the environments in which they have evolved.

Previous research into microswimming in complex fluids has been limited to a collection of largely unrelated observations about various swimmers in various fluids. This thesis has begun to provide a better mechanistic understanding that is required to connect these observation. In doing so, we hope to have demonstrated the importance of providing intuitive pictures about how the swimmers interact with their fluid environments. Without these, we cannot hope to apply the research done on microswimmers in simple situations, such as swimming through synthetic-polymer solutions, to swimming in real biological complex fluids. In particular, this would be necessary for any design of artificial swimmers. In fact, our mechanistic understanding of Taylor's sheet allowed us to design a peristaltic swimmer that swims faster in viscoelastic fluids than in Newtonian ones.

Bibliography

[1] Thomas R Ives and Alexander Morozov. The mechanism of propulsion of a model microswimmer in a viscoelastic fluid next to a solid boundary. *Physics of Fluids 29*, 121612, 2017.

[2] James Lighthill. *Mathematical Biofluiddynamics*. Society for Industrial and Applied Mathematics, jan 1975.

[3] E. M. Purcell. Life at Low Reynolds Number. *American Journal of Physics*, 45(1):3–11, dec 1977.

[4] J Gray. The movement of sea-urchin spermatozoa. *Journal of Experimental Biology*, 32(May):755–801, 1955.

[5] Geoffrey Taylor. Analysis of the Swimming of Microscopic Organisms. *Proceedings of the Royal Society A: Mathematical, Physical and Engineering Sciences*, 209(1099):447–461, nov 1951.

[6] G. J. Hancock. The Self-Propulsion of Microscopic Organisms through Liquids. *Proceedings of the Royal Society A: Mathematical, Physical and Engineering Sciences*, 217(1128):96–121, mar 1953.

[7] A. T. Chwang and T. Y. Wu. A note on the helical movement of microorganisms. *Proceedings of the Royal Society of London. Series B, Biological Sciences*, 178(1052):327–346, 1971.

[8] Howard C. Berg and Robert A. Anderson. Bacteria swim by rotating their flagellar filaments. *Nature*, 245:380–382, 1973.

[9] Edward M. Purcell. The efficiency of propulsion by a rotating flagellum. *Proceedings of the National Academy of Sciences*, 94(21):11307–11311, oct 1997.

[10] Pawel Romanczuk, Markus Bär, Werner Ebeling, Benjamin Lindner, and Lutz Schimansky-Geier. Active Brownian Particles. From Individual to Collective Stochastic Dynamics. *European Physical Journal ST*, 162:1–162, 2012.

[11] Christopher Dombrowski, Luis Cisneros, Sunita Chatkaew, Raymond E. Goldstein, and John O. Kessler. Self-concentration and large-scale coherence in bacterial dynamics. *Physical Review Letters*, 93(9):2–5, 2004.

[12] Jörn Dunkel, Sebastian Heidenreich, Knut Drescher, et al. Fluid dynamics of bacterial turbulence. *Physical review letters*, 110(22):228102, 2013.

[13] N A Croll. *The behaviour of nematodes: their activity, senses and responses.* London: Edward Arnold (Publishers) Ltd., 1970.

[14] E.A. Gaffney, H. Gadêlha, D.J. Smith, J.R. Blake, and J.C. Kirkman-Brown. Mammalian Sperm Motility: Observation and Theory. *Annual Review of Fluid Mechanics*, 43(1):501–528, jan 2011.

[15] Sören Schreiber, Manuela Konradt, Claudia Groll, et al. The spatial orientation of Helicobacter pylori in the gastric mucus. *Proceedings of the National Academy of Sciences of the United States of America*, 101(14):5024–5029, 2004.

[16] Susan Sanchez, Charles L Hofacre, Margie D Lee, John J Maurer, and Michael P Doyle. Animal sources of salmonellosis in humans. *Journal of the American Veterinary Medical Association*, 221(4):492–497, 2002.

[17] Ali Houry, Michel Gohar, Julien Deschamps, et al. Bacterial swimmers that infiltrate and take over the biofilm matrix. *Proceedings of the National Academy of Sciences of the United States of America*, 109(32):13088–93, 2012.

[18] Bin Liu, Thomas R. Powers, and K. S. Breuer. Force-free swimming of a model helical flagellum in viscoelastic fluids. *Proceedings of the National Academy of Sciences*, 108(49):19516–19520, dec 2011.

[19] Vincent A. Martinez, Jana Schwarz-Linek, Mathias Reufer, et al. Flagellated bacterial motility in polymer solutions. *Proceedings of the National Academy of Sciences*, 111(50):17771–17776, 2014.

[20] X. N. Shen and P. E. Arratia. Undulatory Swimming in Viscoelastic Fluids. *Physical Review Letters*, 106(20):208101, may 2011.

[21] Moumita Dasgupta, Bin Liu, Henry C. Fu, et al. Speed of a swimming sheet in Newtonian and viscoelastic fluids. *Physical Review E*, 87(1):013015, jan 2013.

[22] Eric Lauga. Propulsion in a viscoelastic fluid. *Physics of Fluids*, 19(8):083104, 2007.

[23] Gaojin Li and Arezoo M. Ardekani. Undulatory swimming in non-Newtonian fluids. *Journal of Fluid Mechanics*, 784:R4, 2015.

[24] Joseph Teran, Lisa Fauci, and Michael Shelley. Viscoelastic Fluid Response Can Increase the Speed and Efficiency of a Free Swimmer. *Physical Review Letters*, 104(3):038101, jan 2010.

[25] Emily E. Riley and Eric Lauga. Enhanced active swimming in viscoelastic fluids. *EPL (Europhysics Letters)*, 108(3):34003, nov 2014.

[26] M. De Corato, F. Greco, and P. L. Maffettone. Locomotion of a microorganism in weakly viscoelastic liquids. *Physical Review E*, 92(5):053008, nov 2015.

[27] Saverio E. Spagnolie, Bin Liu, and Thomas R. Powers. Locomotion of Helical Bodies in Viscoelastic Fluids: Enhanced Swimming at Large Helical Amplitudes. *Physical Review Letters*, 111(6):068101, aug 2013.

[28] Shahrzad Yazdi, Arezoo M. Ardekani, and Ali Borhan. Locomotion of microorganisms near a no-slip boundary in a viscoelastic fluid. *Physical Review E*, 90(4):043002, oct 2014.

[29] S. Yazdi, A. M. Ardekani, and A. Borhan. Swimming Dynamics Near a Wall in a Weakly Elastic Fluid. *Journal of Nonlinear Science*, 25(5):1153–1167, oct 2015.

[30] G. J. Li, A. Karimi, and A. M. Ardekani. Effect of solid boundaries on swimming dynamics of microorganisms in a viscoelastic fluid. *Rheologica Acta*, 53(12):911–926, dec 2014.

[31] Henry C. Fu, Thomas R. Powers, and Charles W. Wolgemuth. Theory of Swimming Filaments in Viscoelastic Media. *Physical Review Letters*, 99(25):258101, dec 2007.

[32] Henry C. Fu, Charles W Wolgemuth, and Thomas R. Powers. Swimming speeds of filaments in nonlinearly viscoelastic fluids. *Physics of Fluids*, 21(3):033102, mar 2009.

[33] Henry C. Fu, Vivek B. Shenoy, and Thomas R. Powers. Low-Reynolds-number swimming in gels. *Epl*, 91(2), 2010.

[34] James Lighthill. Flagellar Hydrodynamics. *SIAM Review*, 18(2):161–230, apr 1976.

[35] John R. Blake. Microbiological fluid mechanics: a tribute to Sir James Lighthill. *Mathematical Methods in the Applied Sciences*, 24(17-18):1469–1483, nov 2001.

[36] Eric Lauga and Thomas R. Powers. The hydrodynamics of swimming microorganisms. *Reports on Progress in Physics*, 72(9):096601, sep 2009.

[37] Howard C. Berg. Motile Behavior of Bacteria. *Physics Today*, 53(1):24–29, jan 2000.

[38] Fredrick C. Neidhardt, John L. Ingraham, and Moselio Schaechter. *Physiology of the Bacterial Cell: A Molecular Approach*. Sinauer Associates, Inc., 1990.

[39] S. Chattopadhyay, R. Moldovan, C. Yeung, and X. L. Wu. Swimming efficiency of bacterium Escherichia coli. *Proceedings of the National Academy of Sciences*, 103(37):13712–13717, sep 2006.

[40] I. R. Gibbons. Cilia and flagella of eukaryotes. *The Journal of Cell Biology*, 91(3):107–124, dec 1981.

[41] C. J. Brokaw. Non-sinusoidal bending waves of sperm flagella. *Journal of Experimental Biology*, 43(1):155–169, 1965.

[42] S. S. Merchant, S. E. Prochnik, O. Vallon, et al. The Chlamydomonas Genome Reveals the Evolution of Key Animal and Plant Functions. *Science*, 318(5848):245–250, 2007.

[43] David R Mitchell. Chlamydomonas flagella. *Journal of Phycology*, 36(2):261–273, dec 2001.

[44] D.F Katz and G.K Ojakian. A simple technique for the measurement of swimming speed of Chlamydomonas. *Experimental Cell Research*, 81(2):487–491, 1973.

[45] B. Martinac, Y. Saimi, and C. Kung. Ion Channels in Microbes. *Physiological Reviews*, 88(4):1449–1490, oct 2008.

[46] Nancy M Bonini. Differential regulation of Paramecium ciliary motility by cAMP and cGMP. *The Journal of Cell Biology*, 106(5):1615–1623, may 1988.

[47] Bruce Alberts, John Wilson, and Tim Hunt. *Molecular biology of the cell*. Garland Science, New York, fifth edit edition, 2008.

[48] J. Sznitman, X. Shen, P. K. Purohit, and P. E. Arratia. The Effects of Fluid Viscosity on the Kinematics and Material Properties of C. elegans Swimming at Low Reynolds Number. *Experimental Mechanics*, 50(9):1303–1311, nov 2010.

[49] Jing Yang, Charles W. Wolgemuth, and Greg Huber. Kinematics of the swimming of spiroplasma. *Physical Review Letters*, 102(21):2–5, 2009.

[50] L Margulis, J B Ashen, M Sole, and R Guerrero. Composite, large spirochetes from microbial mats: spirochete structure review. *Proc Natl Acad Sci U S A*, 90(15):6966–6970, 1993.

[51] Howard C. Berg. How spirochetes may swim. *Journal of Theoretical Biology*, 56(2):269–273, 1976.

[52] S. F. Goldstein, N. W. Charon, and J. A. Kreiling. Borrelia burgdorferi swims with a planar waveform similar to that of eukaryotic flagella. *Proceedings of the National Academy of Sciences*, 91(8):3433–3437, 1994.

[53] Martin Sauzade, Gwynn J. Elfring, and Eric Lauga. Taylor's swimming sheet: Analysis and improvement of the perturbation series. *Physica D: Nonlinear Phenomena*, 240(20):1567–1573, oct 2011.

[54] A. J. Reynolds. The swimming of minute organisms. *Journal of Fluid Mechanics*, 23(2):241–260, 1965.

[55] E. O. Tuck. A note on a swimming problem. *Journal of Fluid Mechanics*, 31(02):305, jan 1968.

[56] O. S. Pak and E. Lauga. The transient swimming of a waving sheet. *Proceedings of the Royal Society A: Mathematical, Physical and Engineering Sciences*, 466(2113):107–126, 2010.

[57] Gwynn J. Elfring, On Shun Pak, and Eric Lauga. Two-dimensional flagellar synchronization in viscoelastic fluids. *Journal of Fluid Mechanics*, 646:505, mar 2010.

[58] Gwynn J. Elfring and Eric Lauga. Synchronization of flexible sheets. *Journal of Fluid Mechanics*, 674:163–173, may 2011.

[59] Jian Du, James P. Keener, Robert D. Guy, and Aaron L. Fogelson. Low-Reynolds-number swimming in viscous two-phase fluids. *Physical Review E*, 85(3):036304, mar 2012.

[60] Emily E. Riley and Eric Lauga. Small-amplitude swimmers can self-propel faster in viscoelastic fluids. *Journal of Theoretical Biology*, 382:345–355, oct 2015.

[61] Gwynn J. Elfring and Gaurav Goyal. The effect of gait on swimming in viscoelastic fluids. *Journal of Non-Newtonian Fluid Mechanics*, 234:8–14, aug 2016.

[62] J. Rodrigo Vélez-Cordero and Eric Lauga. Waving transport and propulsion in a generalized newtonian fluid. *Journal of Non-Newtonian Fluid Mechanics*, 199:37–50, 2013.

[63] R. Bansil. Mucin Biophysics. *Annual Review of Physiology*, 57(1):635–657, jan 1995.

[64] S. H. Hwang, M. Litt, and W. C. Forsman. Rheological properties of mucus. *Rheologica Acta*, 8(4):438–448, oct 1969.

[65] Samuel K. Lai, Ying Ying Wang, Denis Wirtz, and Justin Hanes. Micro- and macrorheology of mucus. *Advanced Drug Delivery Reviews*, 61(2):86–100, 2009.

[66] R G Larson. *The Structure and Rheology of Complex Fluids*. Topics in Chemical Engineering. OUP USA, 1999.

[67] M Rubinstein and R H Colby. *Polymer Physics*. OUP Oxford, 2003.

[68] R. B. Bird, R. C. Armstrong, and O. Hassager. *Dynamics of Polymeric Liquids, Volume 1: Fluid mechanics*. Dynamics of Polymeric Liquids. Wiley, 1987.

[69] R. B. Bird, O. Hassager, R. C. Armstrong, and C. F. Curtiss. *Dynamics of Polymeric Liquids, Volume 2: Kinetic Theory*. Wiley, 1987.

[70] David F James. Boger Fluids. *Annual Review of Fluid Mechanics*, 41:129–142, 2009.

[71] David J. Smith, E. A. Gaffney, H. Gadêlha, N. Kapur, and J. C. Kirkman-Brown. Bend propagation in the flagella of migrating human sperm, and its modulation by viscosity. *Cell Motility and the Cytoskeleton*, 66(4):220–236, apr 2009.

[72] Howard C. Berg and Linda Turner. Movement of microorganisms in viscous environments. *Nature*, 278(5702):349–351, 1979.

[73] W R Schneider and R N Doetsch. Effect of Viscosity on Bacterial Motility. *Journal of Bacteriology*, 117(2):696–701, 1974.

[74] D. F. Katz, J. R. Blake, and S. L. Paveri-Fontana. On the movement of slender bodies near plane boundaries at low Reynolds number. *Journal of Fluid Mechanics*, 72(03):529, 1975.

[75] Gwynn J. Elfring and Eric Lauga. Theory of Locomotion Through Complex fluids. In Saverio E. Spagnolie, editor, *Complex Fluids in Biological Systems*, Biological and Medical Physics, Biomedical Engineering, pages 283–317. Springer New York, New York, NY, 2015.

[76] David F. Katz. On the propulsion of micro-organisms near solid boundaries. *Journal of Fluid Mechanics*, 64(01):33, 1974.

[77] J. P. Boyd. *Chebyshev and Fourier Spectral Methods: Second Revised Edition*. Dover Books on Mathematics. Dover Publications, 2013.

[78] C. Canuto, M. Y. Hussaini, A. Quarteroni, and T. A. Zang. *Spectral Methods in Fluid Dynamics*. Springer-Verlag, 1987.

[79] Steven A Orszag. Accurate solution of the Orr–Sommerfeld stability equation. *Journal of Fluid Mechanics*, 50(04):689, dec 1971.

[80] Randy H. Ewoldt, A. E. Hosoi, and Gareth H. McKinley. New measures for characterizing nonlinear viscoelasticity in large amplitude oscillatory shear. *Journal of Rheology*, 52(6):1427–1458, 2008.

[81] Joo Sung Lee, Rebecca Dylla-Spears, Nerayo P. Teclemariam, and Susan J. Muller. Microfluidic four-roll mill for all flow types. *Applied Physics Letters*, 90(7):074103, feb 2007.

[82] Allison P. Berke, Linda Turner, Howard C. Berg, and Eric Lauga. Hydrodynamic Attraction of Swimming Microorganisms by Surfaces. *Physical Review Letters*, 101(3):038102, jul 2008.

[83] Félix Lebois, Pascal Sauvage, Charlotte Py, et al. Locomotion Control of Caenorhabditis elegans through Confinement. *Biophysical Journal*, 102(12):2791–2798, jun 2012.

[84] Diego Lopez and Eric Lauga. Dynamics of swimming bacteria at complex interfaces. *Physics of Fluids*, 26(7):071902, jul 2014.

[85] T. D. Montenegro-Johnson, H. Gadelha, and D. J. Smith. Spermatozoa scattering by a microchannel feature: an elastohydrodynamic model. *Royal Society Open Science*, 2(3):140475–140475, mar 2015.

[86] R. D. Schulman, M. Backholm, W. S. Ryu, and K. Dalnoki-Veress. Undulatory microswimming near solid boundaries. *Physics of Fluids*, 26(10):101902, oct 2014.

[87] Renaud Trouilloud, Tony Yu, A. Hosoi, and Eric Lauga. Soft Swimming: Exploiting Deformable Interfaces for Low Reynolds Number Locomotion. *Physical Review Letters*, 101(4):048102, jul 2008.

[88] Darren Crowdy, Sungyon Lee, Ophir Samson, Eric Lauga, and A. E. Hosoi. A two-dimensional model of low-Reynolds number swimming beneath a free surface. *Journal of Fluid Mechanics*, 681(2):24–47, aug 2011.

[89] Jackson C. Kirkman-Brown and David J. Smith. Sperm motility: is viscosity fundamental to progress? *Molecular Human Reproduction*, 17(8):539–544, aug 2011.

[90] James E. Mark. *Polymer Data Handbook*. Oxford University Press, 1999.

[91] Frederick A. Bettelheim and Santosh K. Dey. Molecular parameters of submaxillary mucins. *Archives of Biochemistry and Biophysics*, 109(2):259–265, 1965.

[92] P G de Gennes. *Scaling Concepts in Polymer Physics*. Cornell University Press, 1979.

[93] Yi Man and Eric Lauga. Phase-separation models for swimming enhancement in complex fluids. *Physical Review E*, 92(2):023004, aug 2015.

[94] Lei Li and Saverio E. Spagnolie. Swimming and pumping of rigid helical bodies in viscous fluids. *Physics of Fluids*, 26(4), 2014.

[95] R. S. Berman, O. Kenneth, J. Sznitman, and A. M. Leshansky. Undulatory locomotion of finite filaments: lessons from Caenorhabditis elegans. *New Journal of Physics*, 15(7):075022, jul 2013.

[96] François Alouges, Antonio DeSimone, and Aline Lefebvre. Optimal Strokes for Low Reynolds Number Swimmers: An Example. *Journal of Nonlinear Science*, 18(3):277–302, jun 2008.

[97] Stephan Koehler, Tristan Spoor, and B S Tilley. Pitching , bobbing , and performance metrics for undulating finite-length swimming filaments. *Physics of Fluids*, 24:091901, 2012.

[98] O. Pironneau and D. F. Katz. Optimal swimming of flagellated microorganisms. *Journal of Fluid Mechanics*, 66(02):391, mar 1974.

[99] O. Wiezel and Y. Or. Optimization and small-amplitude analysis of Purcell's three-link microswimmer model. *Proceedings of the Royal Society A: Mathematical, Physical and Engineering Science*, 472(2192):20160425, aug 2016.

[100] Daniel Tam and a. Hosoi. Optimal Stroke Patterns for Purcell's Three-Link Swimmer. *Physical Review Letters*, 98(6):068105, feb 2007.

[101] Hanliang Guo, Janna Nawroth, Yang Ding, and Eva Kanso. Cilia beating patterns are not hydrodynamically optimal. *Physics of Fluids*, 26(9):091901, sep 2014.

[102] A. M Makarieva, V. G Gorshkov, and B.-L. Li. Energetics of the smallest: do bacteria breathe at the same rate as whales? *Proceedings of the Royal Society B: Biological Sciences*, 272(1577):2219–2224, 2005.

[103] Christina L Lewis, Caelli C Craig, and Andre G Senecal. Mass and Density Measurements of Live and Dead Gram-Negative and Gram-Positive Bacterial Populations. *Applied and Environmental Microbiology*, 80(12):3622–3631, 2014.

[104] Rajindar S Sohal. Metabolism and aging in the nematode Caenorhabditis elegans. *Free Radical Biology & Medicine*, 33(5):587–596, 2002.

[105] J. Sznitman, X. Shen, R. Sznitman, and P. E. Arratia. Propulsive force measurements and flow behavior of undulatory swimmers at low Reynolds number. *Physics of Fluids*, 22(12), 2010.

[106] M A Nowak. *Evolutionary Dynamics*. Harvard University Press, 2006.

[107] A. M. Leshansky, O. Kenneth, O. Gat, and J. E. Avron. A frictionless microswimmer. *New Journal of Physics*, 9(145), 2007.

[108] Stephen Childress. A thermodynamic efficiency for Stokesian swimming. *Journal of Fluid Mechanics*, 705:77–97, 2012.

[109] By J J L Higdon. A hydrodynamic analysis of flagellar propulsion. *Journal of Fluid Mechanics*, 90:685–711, 1979.

[110] J. J. L. Higdon. The hydrodynamics of flagellar propulsion : helical waves. *Journal of Fluid Mechanics*, 94:331–351, 1979.

[111] Thomas D. Montenegro-Johnson and Eric Lauga. Optimal swimming of a sheet. *Physical Review E - Statistical, Nonlinear, and Soft Matter Physics*, 89(6):1–6, 2014.

[112] M. J. Lighthill. On the squirming motion of nearly spherical deformable bodies through liquids at very small reynolds numbers. *Communications on Pure and Applied Mathematics*, 5(2):109–118, may 1952.

[113] J. Gray and G. J. Hancock. The propulsion of sea-urchin spermatozoa. *Journal of Experimental Biology*, 32:802–814, dec 1955.

[114] Eric Jones, Travis Oliphant, Pearu Peterson, and Others. Scipy, 2001.

[115] Richard H Byrd, Peihuang Lu, Jorge Nocedal, and Ciyou Zhu. A Limited Memory Algorithm for Bound Constrained Optimization. *SIAM Journal on Scientific Computing*, 16(5):1190–1208, 1995.

[116] Devon M. Fitzgerald, Richard P. Bonocora, and Joseph T. Wade. Comprehensive Mapping of the Escherichia coli Flagellar Regulatory Network. *PLoS Genetics*, 10(10), 2014.